

# Are seasonal deposits in spring at the Martian North Pole much shallower than previously thought?

Haifeng Xiao<sup>1</sup>, Yuchi Xiao<sup>2</sup>, Shu Su<sup>3</sup>, Frédéric Schmidt<sup>4</sup>, Luisa M. Lara<sup>5</sup>, and Pedro J. Gutiérrez<sup>6</sup>

<sup>1</sup>Technische Universität Berlin

<sup>2</sup>China University of Geosciences (CUG)

<sup>3</sup>Technical University of Berlin

<sup>4</sup>GEOPS, Université Paris-Saclay, CNRS, France

<sup>5</sup>Instituto de Astrofísica de Andalucía (IAA-CSIC)

<sup>6</sup>Instituto de Astrofísica de Andalucía (CSIC)

September 11, 2023

## Abstract

The seasonal deposition and sublimation of CO<sub>2</sub> constitute a major element in the Martian volatile cycle. Here, we propose to use the shadow variations of the ice blocks at the foot of the steep scarps of the North Polar Layered Deposits (NPLDs) to infer the vertical evolution of the seasonal deposits at high polar latitudes. We conduct an experiment at a steep scarp centered at (85.0°N, 151.5°E). We show that the average thickness of the seasonal deposits due to snowfalls in Mars Year 31 is  $0.97 \pm 0.13$  m at Ls = 350.7° in late winter, which then gradually decreases in springtime. The large snow depth measured makes us wonder if snowfalls are more frequent and violent than previously thought. Meanwhile, we show that the average frost thickness due to direct condensation in Mars Year 31 reaches  $0.64 \pm 0.18$  m at Ls = 350.7° in late winter and quasi-linearly decreases towards the summer solstice. Combined, the total thickness of the seasonal cover in Mars Year 31 reaches  $1.63 \pm 0.22$  m at Ls = 350.7° in late winter, continuously decreases to  $0.45 \pm 0.06$  m at Ls = 42.8° in middle spring and  $0.06 \pm 0.05$  m at Ls = 69.6° in late spring. These estimates are up to 0.8 m lower than the existing MOLA results during the spring, which can be mainly attributed to MOLA-related biases. In terms of interannual variations, we observe that snow in the very early spring of Mars Year 36 can be  $0.36 \pm 0.13$  m deeper than that in Mars Year 31.



**18 Abstract**

**19** The seasonal deposition and sublimation of CO<sub>2</sub> constitute a major element in the Mar-  
**20** tian volatile cycle. Here, we propose to use the shadow variations of the ice blocks at the foot  
**21** of the steep scarps of the North Polar Layered Deposits (NPLDs) to infer the vertical evolu-  
**22** tion of the seasonal deposits at high polar latitudes. We conduct an experiment at a steep scarp  
**23** centered at (85.0°N, 151.5°E). We show that the average thickness of the seasonal deposits due  
**24** to snowfalls in Mars Year 31 is  $0.97\pm 0.13$  m at  $L_s = 350.7^\circ$  in late winter, which then grad-  
**25** ually decreases in springtime. The large snow depth measured makes us wonder if snowfalls are  
**26** more frequent and violent than previously thought. Meanwhile, we show that the average frost  
**27** thickness due to direct condensation in Mars Year 31 reaches  $0.64\pm 0.18$  m at  $L_s = 350.7^\circ$  in  
**28** late winter and quasi-linearly decreases towards the summer solstice. Combined, the total thick-  
**29** ness of the seasonal cover in Mars Year 31 reaches  $1.63\pm 0.22$  m at  $L_s = 350.7^\circ$  in late win-  
**30** ter, continuously decreases to  $0.45\pm 0.06$  m at  $L_s = 42.8^\circ$  in middle spring and  $0.06\pm 0.05$  m  
**31** at  $L_s = 69.6^\circ$  in late spring. These estimates are up to 0.8 m lower than the existing MOLA  
**32** results during the spring, which can be mainly attributed to MOLA-related biases. In terms  
**33** of interannual variations, we observe that snow in the very early spring of Mars Year 36 can  
**34** be  $0.36\pm 0.13$  m deeper than that in Mars Year 31.

**35 Plain Language Summary**

**36** Like Earth, Mars also has seasons. Up to one third of the atmosphere's CO<sub>2</sub> is exchange-  
**37** ing with the polar regions through seasonal deposition/sublimation processes. At the steep scarps  
**38** of the North Polar Layered Deposits (NPLDs), ice fractures can detach and fall to form ice blocks.  
**39** We propose to use variations in the shadows of these ice blocks, observed in the High Resolu-  
**40** tion Imaging Science Experiment (HiRISE) images, to infer the thickness evolution of the sea-  
**41** sonal deposits. We show that the average thickness of snowfalls at a study scarp is around 1 m  
**42** in late winter in Mars Year 31. Meanwhile, we show that the average thickness of frosts directly  
**43** condensed onto the surface reaches  $\sim 0.6$  m in late winter and quasi-linearly decreases towards  
**44** late spring. Combining these two aspects, the gross thickness reaches  $\sim 1.6$  m in late winter,  
**45** decreases to  $\sim 0.4$  m in middle spring, and further declines to  $\sim 0.1$  m in late spring. Surpris-  
**46** ingly, these estimates are up to 0.8 m lower than the existing results during the springtime. It  
**47** is expected that these proposed approaches can enable us to put important constraints on the  
**48** Martian volatile cycles.

**49 1 Introduction**

**50** Three billion years ago, when life emerged on Earth, the climate of Mars could have been  
**51** with a thick atmosphere and a circumpolar ocean of liquid water in the northern hemisphere  
**52** (Head III et al., 1999; Schmidt et al., 2022). Unfortunately, present Mars is barren and arid with

53 almost all water exists as ice, though it also exists in small quantities as vapor in the atmosphere.  
54 The Martian Polar Layered Deposits (PLDs) are predominantly pure water ice accumulated  
55 due to periodic orbital forcing (Laskar et al., 2002; Becerra et al., 2017), with a diameter of 1,000 km  
56 across and a thickness of a few kilometers (Plaut et al., 2007; Nerozzi & Holt, 2019). The spi-  
57 ral troughs that dissect the deposits contain thousands of visible ice layers with varying ratio  
58 of dust that record the Martian climate history in the Late Amazonian (Grima et al., 2009; Be-  
59 cerra et al., 2017). Carving of the troughs are probably related to prevailing katabatic winds  
60 that spiral due to the Coriolis effects. The PLDs, together with outlying crater ice deposits (Sori  
61 et al., 2022; McGlasson et al., 2023), are the most accessible and complete planetary climate  
62 records, making them among the most compelling science targets in the Solar System (I. B. Smith  
63 et al., 2020; Becerra et al., 2021). On the steep scarps at the margins of the North Polar Lay-  
64 ered Deposits (NPLDs), mass-wasting processes like dust-ice avalanches and ice block falls have  
65 been frequently observed (Russell et al., 2008; Fanara et al., 2020b; Su, Fanara, Zhang, et al.,  
66 2023; Su, Fanara, Xiao, et al., 2023). The latter is in the form of scattered ice blocks and ac-  
67 cumulating apron-like debris at the foot of the scarps. These phenomena represent multiple al-  
68 ternative modes of erosion in addition to sublimation, which are held accountable for mass losses  
69 of the polar ice caps. Mass loss rate due to these phenomena can compete with the outward  
70 motion due to viscous deformation to shape the NPLDs' rheology and evolution (Sori et al.,  
71 2015; Fanara et al., 2020b). In terms of the ice blocks, ice fragments that fall from the steep  
72 scarps are mainly protrusions that break due to structural failure once being subject to inter-  
73 nal/external triggers, for example, thermal expansion/contraction and then stress-induced poly-  
74 gonal fracturing, the loading/removal of the topping seasonal deposits (Xiao, Stark, Schmidt,  
75 Hao, Steinbrügge, et al., 2022), or even the downward katabatic winds (Byrne et al., 2017).

76 Due to its obliquity ( $\sim 25^\circ$  compared to  $23.5^\circ$  of Earth), there exist seasons on Mars as the  
77 planet orbits the Sun. When temperature drops below the  $\text{CO}_2$  condensation point (approx-  
78 imately 148 K at average Martian surface pressure, but can range from 130 K to 154 K depend-  
79 ing on elevation and season) in the fall and winter, the  $\text{CO}_2$  solidifies and accumulates as snow  
80 or frosts in the polar regions. Then when the temperature increases during spring, these de-  
81 posits sublimate into the atmosphere. Each Martian year, up to one third of the atmospheric  
82  $\text{CO}_2$  is involved in the seasonal deposition/sublimation process (Leighton & Murray, 1966). There  
83 exist two depositional mechanisms, that is, atmospheric precipitation as snowfalls and direct  
84 surface condensation as frosts (Määttänen & Montmessin, 2021). The resultant Seasonal South/North  
85 Polar Caps (SSPC, SNPC) can laterally extend down to  $50^\circ\text{S/N}$  in the beginning of winter un-  
86 der current conditions (Piqueux et al., 2015). Understanding these seasonal processes can place  
87 vital constraints on the Martian volatile cycles, and help with determination of the current mass  
88 balance of the polar ice reservoirs (Becerra et al., 2021). The thickness of the surficial layer would  
89 have important implications for the feasibility or trafficability of future landers, rovers, or he-  
90 licopters that would drill into the PLDs and decipher the stored paleoclimate of Mars (I. B. Smith  
91 et al., 2020; Matthies et al., 2022). Through Mars Climate Sounder (MCS) observations, it is

92 now believed that water ice particles in the atmosphere can act as condensation nuclei onto which  
93 the CO<sub>2</sub> ice condenses and be deposited onto the polar caps along with the CO<sub>2</sub> snowfalls (Al-  
94 saeed & Hayne, 2022). Thus, by constraining the quantities of the CO<sub>2</sub> snowfalls, we can also  
95 gain insights into the amount of water that can be annually removed from the atmosphere through  
96 this scavenging process. These information can also help to determine the current mass bal-  
97 ance of the residual north polar cap, that is, whether it is accumulating or ablating. Dynamic  
98 geological phenomena associated with sublimation of the SSPC/SNPC, for example, dark fans,  
99 polygonal cracks, spiders (South Pole)/furrows (North Pole), and alcoves in the dune fields, can  
100 be better modeled and interpreted given meaningful thickness evolution measurements of the  
101 overlying seasonal layer (for example, Portyankina et al., 2010; Hansen et al., 2013; Schmidt  
102 & Portyankina, 2018; Dundas et al., 2021; Mc Keown et al., 2023). Meanwhile, the amount of  
103 mass being seasonally added and removed from the surface is enough to induce significant elas-  
104 tic displacements of the lithosphere (Métivier et al., 2008). Characterizing these displacements  
105 through use of current altimetry or future dedicated geodetic missions can place important con-  
106 straints on the current thermal and rheologic state of the Martian interior (Wagner et al., 2023).  
107 The changing mass loads can also cause small but measurable effects on Mars gravity and – through  
108 changing mass distribution and moments of inertia – rotation (that is, nutation, polar motion,  
109 and length of day variation; Defraigne et al., 2000; Van den Acker et al., 2002; Le Maistre et  
110 al., 2023).

111 The direct depth variation measurements of the seasonal deposits have been made by exploit-  
112 ing dynamic Mars Orbiter Laser Altimeter (MOLA) elevation profiles (D. E. Smith et al.,  
113 2001; Aharonson et al., 2004; Xiao, Stark, Schmidt, Hao, Su, et al., 2022; Xiao, Stark, Schmidt,  
114 Hao, Steinbrügge, et al., 2022). The MOLA estimates can be easily extended to cover the en-  
115 tire polar regions. D. E. Smith et al. (2001) calculated the height differences of the MOLA heights  
116 to median-filtered reference surface at various latitudinal annuli and measured the maximum  
117 thickness to be  $\sim 1$  m at both poles. Aharonson et al. (2004) fitted sinusoidal curves to the height  
118 differences obtained at locations where two MOLA profiles intersect, that is, cross-overs, and  
119 estimated the maximum depth variations to be  $\sim 1.5$  m at the North Pole and  $\sim 2.5$  m at the  
120 South Pole. Recently, by reprocessing the MOLA profiles and self-registering them (Xiao, Stark,  
121 Steinbrügge, et al., 2022; Xiao, Stark, Steinbrügge, et al., 2021), Xiao, Stark, Schmidt, Hao, Su,  
122 et al. (2022); Xiao, Stark, Schmidt, Hao, Steinbrügge, et al. (2022) derived both spatial and tem-  
123 poral thickness variations of the seasonal polar caps with a maximum of about 2.5 m at the south  
124 and 1.3 m at the north. In particular, they brought attention to abnormal behavior of the SNPC  
125 over the extensive linear dune fields at Olympia Undae, where maximum thickness variations  
126 up to 4 m and significant off-season increases and decreases up to 3 m in magnitude have been  
127 spotted. Olympia Undae, which roughly spreads from 78°N to 83°N in latitude and 120°E to  
128 240°E in longitude (refer to Figure 4 for its location), is the largest continuous dune field on  
129 Mars, with dune percentage coverage typically greater than 80% (Hayward et al., 2010). It is  
130 a part of the vast circumpolar dark dune fields that surround the permanent north polar cap,

131 which are also referred to as the polar erg. However, it should be noted that the MOLA dataset  
132 is temporally limited to MY24 and MY25, impeding it to resolve inter-annual changes in the  
133 seasonal snow/ice depth.

134 [Andrieu et al. \(2018\)](#) applied Bayesian inversion techniques involving a radiative trans-  
135 fer model to constrain the impurity content and depth of the SSPC at a dune field of Richard-  
136 son Crater (72°S, 180°W), and a maximum thickness of  $\sim 0.4$  m was found in early southern  
137 spring. Currently, they are trying to extend the measurements to the SSPC over the “cryptic  
138 region” where features translucent CO<sub>2</sub> slab ice and cold-jetting during the southern spring (re-  
139 fer to [Hansen et al. \(2010\)](#) for the location of this enigmatic region). [Raguso & Nunes \(2021\)](#)  
140 performed advanced radar processing techniques to the SHadow RADar (SHARAD) dataset  
141 to garner the best possible resolution and Signal-to-Noise Ratio (SNR) and co-registered the  
142 subsurface reflectors for estimation of the two-way time delay differences, hence the thickness  
143 of the Martian seasonal layer. Unlike MOLA, these measurements were not affected by ephemeris  
144 errors of the spacecraft but can be biased by possible presence of slope differential between the  
145 surface and the subsurface reference reflectors. Unfortunately, the experimental results are cur-  
146 rently unavailable and extension to other regions with rougher surfaces and less distinct sub-  
147 surface reflectors can be difficult.

148 Another viable way is to relate the rock shadow length changes in high-resolution opti-  
149 cal images to that of the snow/ice depth. The High Resolution Imaging Science Experiment  
150 (HiRISE) camera on-board the NASA’s Mars Reconnaissance Orbiter (MRO) operates in vis-  
151 ible wavelengths, and with a telescopic lens that produces images at resolutions (0.25 m – 1.3 m)  
152 never before seen in planetary exploration missions ([McEwen, 2005](#); [McEwen et al., 2007](#)). This  
153 high-resolution can enable accurate identification of rocks as small as 0.7 m in diameter. The  
154 spacecraft operates in a near sun-synchronous orbit, providing images of similar solar azimuth,  
155 beneficial for comparison of the shadow lengths that indicates snow/ice depth variations. A HiRISE  
156 Digital Elevation Model (DEM) can be derived from a geometric stereo pair acquired on dif-  
157 ferent orbits so that a moderate convergence angle between the two viewing directions is formed  
158 ( $\sim 10^\circ - \sim 25^\circ$ , [McEwen et al., 2007](#)). The camera started to continuously acquire high-resolution  
159 pictures of targeted regions on 29 September 2006, obtaining 5 – 20 observations per day, which  
160 has led to a high-cadence time series of imagery. [Cull et al. \(2010\)](#) utilized HiRISE images to  
161 show that the CO<sub>2</sub> snow/ice thickness reduced from  $\sim 30$  cm in early spring to less than 5 cm  
162 by middle spring at the Mars Phoenix landing site (68.22°N, 125.70°W). [Mount & Titus \(2015\)](#)  
163 also used rock shadow measurements in HiRISE images to infer the seasonal snow/ice depth  
164 at three sites of distinct morphologies (at latitudes between 68°N and 75°N). They showed that  
165 the effects of moats (circumferential shadows around rocks during springtime) and crowns (ac-  
166 cumulation of snow/ice on the tops of rocks) can significantly modify rock shadow measurements  
167 and hence snow/ice depth (refer to Figure 3 of [Mount & Titus \(2015\)](#) for a schematic). There-  
168 fore, they applied an empirical model for correction and performed error propagation analy-

169 sis to reflect the uncertainty in the measurements. These snow/ice depth measurements were  
170 then combined with visible and thermal observations to calculate the bulk density of the sea-  
171 sonal ice cover over time. Despite its high precision, this approach can be spatially limited to  
172 fields where rocks are present on the surface. Unfortunately, at high polar latitudes where max-  
173 imum snow/ice accumulation happens, rocks are unavailable for the purposes of looking into  
174 the seasonal snow/ice thickness evolution.

175 As aforementioned, the only existing measurement of the seasonal snow/ice depth vari-  
176 ations at high latitudes come from MOLA records, which date back to MY24/25. Here, we pro-  
177 pose to use shadows of the ice blocks at the foot of the steep scarps as observed in the HiRISE  
178 images, complementing that of the rocks, as an alternative way to infer the depth of the sea-  
179 sonal deposits. We show how to relate the length of the ice block shadows to its height using  
180 a rigorous geometric model, which is based on orthorectified images and takes both the solar  
181 and surface properties into consideration. Building on this model, we present two independent  
182 and complementary approaches to shed light on the thickness evolution of the ephemeral de-  
183 posits: (1) “SUBTRACTing” that subtracts the ice block heights measured in the summer when  
184 free of seasonal cover to that in the spring; (2) “BOUNDing” that locates ice blocks that have  
185 been completely covered to place lower limits on the thickness of the seasonal deposits, and ice  
186 blocks that have not been completely submerged to put upper limits. We carry out the exper-  
187 iments at a scarp centered at (85.0°N, 151.5°E) and show the feasibility of these applications.  
188 We note that while “SUBTRACTing” is temporally limited to mid-to-late spring, “BOUND-  
189 ing” is capable of yielding measurements in late winter and early spring. Beginning in late north-  
190 ern summer, thin haze rapidly develops into the thick water ice clouds known as the polar hood.  
191 The polar hood can last from late summer, fall, and all the way to winter, and even early spring  
192 (Benson et al., 2011; Navarro et al., 2014; Calvin et al., 2015; Brown et al., 2016). Fortunately,  
193 plenty of unobscured HiRISE images are available during late winter and early spring. During  
194 experiments with these proposed methods, we observe that moats do not exist around the ice  
195 blocks and the depth of the crowns over the ice blocks quasi-linearly decreases to zero when the  
196 seasonal deposits completely sublimate back into the atmosphere. Thus, the empirical correc-  
197 tion scheme described in Mount & Titus (2015), that by adding the snow/ice thickness increases  
198 between consecutive seasons to all prior-season thicknesses, can be inapplicable in our case. We  
199 hence make reasonable assumptions and propose to use the widening of the ice blocks as a proxy  
200 to approximate and correct for the depth of the crowns over the ice blocks. These assumptions  
201 also enable us to decompose the contributions of the snowfalls and direct condensation to the  
202 thickness of the seasonal ice deposits and estimate them separately. Our ultimate goal is to ap-  
203 ply these approaches to all active scarps at high polar latitudes, and rock fields at lower po-  
204 lar latitudes, to obtain good samplings of the vertical evolution of the SNPC. The expected re-  
205 sults can also serve as ground truth to calibrate existing MOLA results and validate contem-  
206 porary anticipated SHARAD results.

207           The paper is structured as follows: In Section 2, bundle adjustment and orthorectifica-  
208           tion of the HiRISE images are introduced. Based on the orthorectified images, the shadowing  
209           model of ice blocks resting at the foot of the steep scarps is presented, and the “SUBTRACT-  
210           ing” and “BOUNDing” approaches to obtain thickness evolution of the SNPC are described. The  
211           study scarp centered at (85.0°N, 151.5°E) is introduced in Section 3. These are followed by the  
212           application of the two independent approaches to ice blocks at the study scarp (Section 4). Af-  
213           ter that, precision of the “SUBTRACTing” results, automation of the “BOUNDing” approach,  
214           interannual variations of snowfalls, estimation and correction for direct condensation effects,  
215           possible biases in the MOLA-derived thicknesses, comparison of measured snowfall thickness  
216           to that predicted by a snowing model, and prospects of future work are successively presented  
217           in Section 5. Finally, conclusions are drawn in Section 6.

## 218    **2 Methods**

219           To correctly relate an ice block’s shadow length to its height, bundle adjustment and sub-  
220           sequent orthorectification of the images should be implemented to remove the image distortions  
221           due to oblique viewing angle and topographic relief. For orthorectification to be carried out,  
222           a precise DEM has to be made using image matching of the bundle-adjusted stereo pairs. Pre-  
223           vious studies using the objects’ shadows to infer their heights focused on relatively flat regions  
224           without significant undulations and thus assumed the surface to be a horizontal plane (for ex-  
225           ample, Blackburn et al., 2010; Cull et al., 2010; Mount & Titus, 2015; P. C. Thomas et al., 2016).  
226           However, in our case, the slopes in the regions where ice blocks reside in the Basal Unit out-  
227           crops, immediately underlying the NPLDs, are significant (up to  $\sim 30^\circ$ ) and have to be consid-  
228           ered in the shadowing geometry. The established shadowing model is then used in the proposed  
229           “SUBTRACTing” and “BOUNDing” approaches to determine the thickness evolution of the sea-  
230           sonal deposits.

### 231           **2.1 Bundle adjustment, DEM generation, and image orthorectification**

232           We use the raw and unprocessed HiRISE images, that is, the Experimental Data Record  
233           (EDR) products, to do bundle adjustment and produce a DEM of the study region using a stereo  
234           pair and the Ames Stereo Pipeline (ASP) software (Beyer et al., 2018; Hepburn et al., 2019).  
235           This DEM is then used to orthorectify all the available images. We note that Reduced Data  
236           Record (RDR) products also exist that are radiometrically-corrected images resampled to a stan-  
237           dard map projection. However, these RDR images lack the required geometric stability for stereo  
238           processing. The sequential procedures applied are: (1) Mosaicking the individual 10 Charged-  
239           Coupled Devices (CCDs) together to single images which includes de-jittering and radio-calibration;  
240           (2) Bundle adjusting all available images to correct for errors in camera position and orienta-  
241           tion (extrinsics only) and make them internally consistent. Feature points are matched across  
242           images. A feature point can be identified in multiple overlapping images, it is equivalent to the

243 concept that a bundle of light rays can intersect at a single triangulated point on the ground.  
 244 In reality, the intersection can be imperfect due to residual errors. In bundle adjustment, each  
 245 triangulated ground point is projected back into the cameras. Then, the sum of squares of resid-  
 246 uals between the pixel coordinates of the feature points and the locations of the projected points,  
 247 that is, reprojection errors, are minimized through a robust least squares solver:

$$248 \quad \{\hat{\mathbf{R}}, \hat{\mathbf{t}}, \hat{\mathbf{P}}\} = \min \sum_{i=1}^n \sum_{j=1}^m (\mathbf{u}_{ij} - \pi(\mathbf{C}_j, \mathbf{R}_j \mathbf{P}_i + \mathbf{t}_j))^2, \quad (1)$$

249 where  $\mathbf{u}_{ij}$  is the observed tie point image coordinate in pixel,  $\mathbf{P}_i$  is the 3D coordinate of the  
 250  $i^{\text{th}}$  ground point (a total of  $n$ ), and  $\mathbf{C}_j$  is the center coordinate of the  $j^{\text{th}}$  camera (a total of  
 251  $m$ ). Meanwhile,  $\mathbf{R}_j$  and  $\mathbf{t}_j$  denote the rotation and translation operations to the  $j^{\text{th}}$  camera,  
 252  $\pi(\mathbf{C}_j, \mathbf{R}_j \mathbf{P}_i + \mathbf{t}_j)$  is the reprojection operator that obtains the reprojected image coordinate  
 253 in pixel of the ground point. Parameters to be adjusted are listed on the left of the equation;  
 254 (3) Locating conjugate feature points through image matching techniques and derive correspond-  
 255 ing disparity values. Sub-pixel correlation in image matching is performed to refine the dispar-  
 256 ity map, which is then converted to heights of the object ground points; (4) Gridding the point  
 257 cloud of object heights to a DEM. This DEM is then applied to orthorectify all of the HiRISE  
 258 images in the depositional area of the ice blocks. We note that the bundle adjustment lacks ab-  
 259 solute ground control points and only tie points are used to improve the internal consistency  
 260 of the images. As a result, there can exist lateral shifts between the DEMs generated in [Su, Fa-](#)  
 261 [nara, Zhang, et al. \(2023\)](#) using stereo pairs from previous bundle-adjustment and the images  
 262 from the bundle adjustment in this study. For more details of these processes, refer to the pipeline  
 263 explained in [Su, Fanara, Zhang, et al. \(2023\)](#).

## 264 2.2 Relating the height of an ice block to its shadow length

265 Figure 1 shows the schematic on the shadowing geometry that we utilize to establish the  
 266 relationship between the height of the Ice Block ( $H$ ) and the measured length of the cast shadow  
 267 as seen in an orthorectified HiRISE image ( $OPs'$ ). The solar elevation angle is  $\alpha$ , while the slope  
 268 is  $\beta$ . We align the local coordinate system with the bearing of the sloped plane ( $O - ABC$ ).  
 269 The angle  $\omega$  measures the angular separation between the sunlight and the orientation of the  
 270 slope. Without considering the slope, the Ice Block in question casts a shadow  $OPh$  on the hor-  
 271 izontal plane, coordinates of which can be written as

$$272 \quad \begin{cases} x_{_Ph} = H \frac{\sin \omega}{\tan \alpha \cos \beta} \\ y_{_Ph} = H \frac{\cos \omega}{\tan \alpha \cos \beta} \end{cases}. \quad (2)$$

273 Now, we consider the existence of the sloped plane and assume the intersection point of the light  
 274 over the tip of the Ice Block with the sloped plane to be  $Ps$ . As  $Ps$  has to be somewhere be-

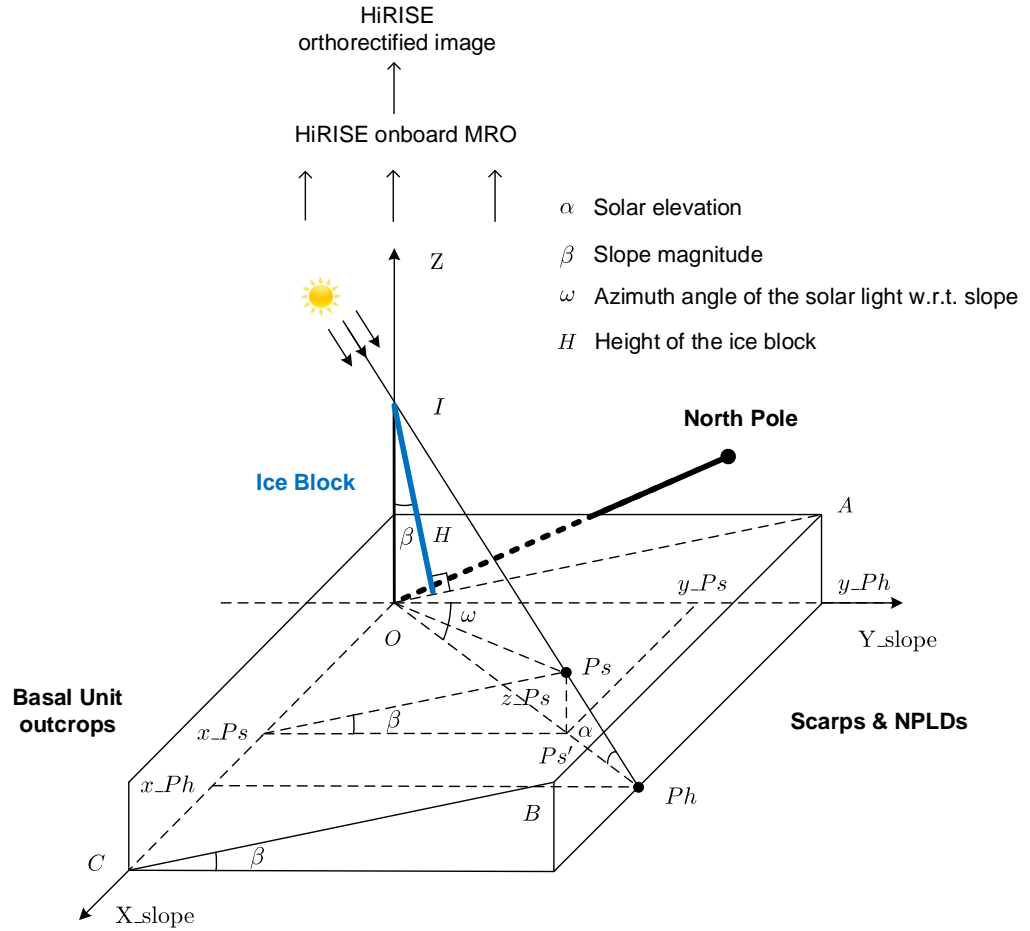


Figure 1: Geometry schematic that illustrates how the solar azimuth, elevation, magnitude and aspect of the slope affect the shadow of the Ice Block situated perpendicular to the slope plane ( $O-ABC$ ).  $Ph$  is the projected point of the Ice Block top onto the horizontal plane, while  $P_s$  is the top onto the inclined plane with a slope of  $\beta$ . The angle  $\alpha$  denotes the elevation angle of the Sun. The angle  $\omega$  represents the relative azimuth angle of the solar rays with respect to that of the slope.

275 tween  $I$  and  $Ph$ , its coordinates can be like

$$276 \quad \begin{cases} x_{Ps} = t \times H \frac{\sin \omega}{\tan \alpha \cos \beta} \\ y_{Ps} = t \times H \frac{\cos \omega}{\tan \alpha \cos \beta} \\ z_{Ps} = (1-t) \times H \frac{1}{\cos \beta} \end{cases}, \quad (3)$$

277 where  $t$  is a scalar between 0 and 1. As can be seen in Figure 1, the ratio of  $z_{Ps}$  and  $y_{Ps}$   
278 equals  $\tan \beta$ , which leads to

$$279 \quad t = \frac{\tan \alpha}{\cos \omega \tan \beta + \tan \alpha}, \quad (4)$$

280 and the coordinates of the intersection point on the sloped plane can be written as

$$281 \quad \begin{cases} x_{Ps} = H \frac{\sin \omega}{\cos \omega \sin \beta + \tan \alpha \cos \beta} \\ y_{Ps} = H \frac{\cos \omega}{\cos \omega \sin \beta + \tan \alpha \cos \beta} \\ z_{Ps} = H \frac{\cos \omega \tan \beta}{\cos \omega \sin \beta + \tan \alpha \cos \beta} \end{cases}. \quad (5)$$

282 The length of the shadow on the slope as measured from the HiRISE orthorectified image is  
283 then

$$284 \quad L_S = \sqrt{x_{Ps}^2 + y_{Ps}^2} = \frac{H}{\cos \omega \sin \beta + \tan \alpha \cos \beta}. \quad (6)$$

285 Solar azimuth together with the elevation at the acquisition time of the HiRISE image  
286 can be calculated by exploiting the information stored in the Spacecraft, Planet, Instrument,  
287 Camera-matrix, and Events (SPICE) kernels (Acton, 1996). Specifically, we access `pck00009.tpc`  
288 Planetary Constant Kernel for orientation and shape of Mars. Meanwhile, we use the `mar063.bsp`  
289 file of the generic planet ephemeris to estimate relative position of Mars with respect to the Sun  
290 at a given time stamp. Slope magnitude and aspect at the Ice Block's location can be approx-  
291 imated by evaluating the elevation values within a  $3 \times 3$  window in the HiRISE DEM gener-  
292 ated in this study. The azimuthal difference of the solar illumination with respect to bearing  
293 of the local slope,  $\omega$  that falls within  $[0^\circ, 180^\circ]$ , can be related to the measured solar azimuth  
294 ( $\varphi$ ) and slope aspect ( $\mu$ ) as shown in Figure S1. For the north polar stereographic projection  
295 centered at the North Pole, the projected body-fixed coordinates of the Ice Block with latitude  
296  $\phi$  and longitude  $L$  can be written as

$$297 \quad \begin{cases} x_{bf} = \frac{2R \cos \phi \sin L}{1 + \sin \phi} \\ y_{bf} = \frac{2R \cos \phi \cos L}{1 + \sin \phi} \end{cases}. \quad (7)$$

298 Once we know the map coordinates of the Ice Block, the analytical expression of  $\omega$  can be de-  
299 rived as follows:

$$300 \quad \begin{aligned} \omega &= |\pi/2 - (\varphi - \varepsilon - \pi/2) - \mu| = \left| \pi - (\varphi - \arctan \frac{x_{bf}}{y_{bf}}) - \mu \right| \\ &= |\pi - (\varphi - (\pi - L)) - \mu| \\ &= |2\pi - \varphi - L - \mu|, \end{aligned} \quad (8)$$

301 where the angle  $\varepsilon$  denotes the intersection angle between the map north and the direction for  
302 the Ice Block in question to the North Pole (Figure S1).

### 303 2.3 The “SUBTRACTing” approach

304 By measuring the shadow lengths of the ice blocks in the orthorectified images, combined  
 305 with auxiliary information on the solar and slope conditions, we can infer the ice block heights  
 306 above the snow/ice cover during spring or the bare ground surface during summer using Equa-  
 307 tion 6. As the HiRISE images can span eight Mars Years (MY), or more than 13 Earth years,  
 308 during which the heights of the ice blocks can slowly shrink due to tumbling and aeolian ero-  
 309 sion. Thus, we use the ice block heights obtained at the temporally adjacent northern summer  
 310 as the reference to infer the depth of the seasonal cap in the springtime. When there exist mul-  
 311 tiple ice block height measurements within a single summer, their average is taken as the ref-  
 312 erence value, as a way to reduce measurement errors. See a detailed discussion in Section 5.1.  
 313 Finally, acquired time-dependent depth values are plotted against the solar longitude for ex-  
 314 amination of their evolution patterns. Here, solar longitude ( $L_s$ ) is used to express the season-  
 315 ality on Mars and  $0^\circ < L_s < 90^\circ$  stands for northern spring,  $90^\circ < L_s < 180^\circ$  for northern  
 316 summer,  $180^\circ < L_s < 270^\circ$  for northern fall, and  $270^\circ < L_s < 360^\circ$  for northern winter. We  
 317 term this approach as “SUBTRACTing”, as it basically subtracts the ice block heights measured  
 318 in the summer to that measured in the spring to gauge the seasonal snow/ice depth in sprint-  
 319 ime.

320 Criteria for selection of the ice blocks as a reference to invert for the thickness variations  
 321 of the seasonal deposits are as follows: (1) Ice blocks are high enough as not to be submerged  
 322 by the seasonal snow/ice; (2) Ice blocks shaped like triangular prisms are the ideal candidates.  
 323 The shadows in these cases run parallel to the ridge lines of the ice blocks. Sticky ice blocks,  
 324 and so their shadows, are also considered solid options. The peaks on the ice blocks and in their  
 325 shadows are normally easy to identify. In both of these cases, the effects of accumulation of snow  
 326 particles over the ice block tops are minimized. However, it should be noted that the forma-  
 327 tion of a layer on the tops of the ice blocks, that is crowning, due to direct condensation of frosts  
 328 can still take place (Section 5.4); (3) The ice blocks can tumble under gravity of its own and  
 329 the seasonal layer, or even be triggered by the katabatic winds down from the polar caps. Fur-  
 330 thermore, erosion due to winds can slowly shrink the size of the ice blocks. Thus, it is required  
 331 that the morphology of the ice blocks and their heights should not significantly change during  
 332 the bracketing summers. For triangular-prism-like ice blocks, the lengths of the shadow are treated  
 333 as the distances between the parallel block crest lines and shadow edge lines along the solar az-  
 334 imuth at the acquisition times of the images. For peaked ice blocks, the lengths of the shadow  
 335 are measured as that of the lines connecting tips of the shadows and their corresponding points  
 336 along the terminators, that is, boundary lines separating the sunlit and shadowed portions of  
 337 the ice blocks. When the latter is blurry, then we fix the starting points of the measuring lines  
 338 at the shadow tips, tweak them to be parallel to the solar azimuth, and determine their end-  
 339 ing points as the intersections between the lines and the respective terminators.

340            2.4 The “BOUNDing” approach

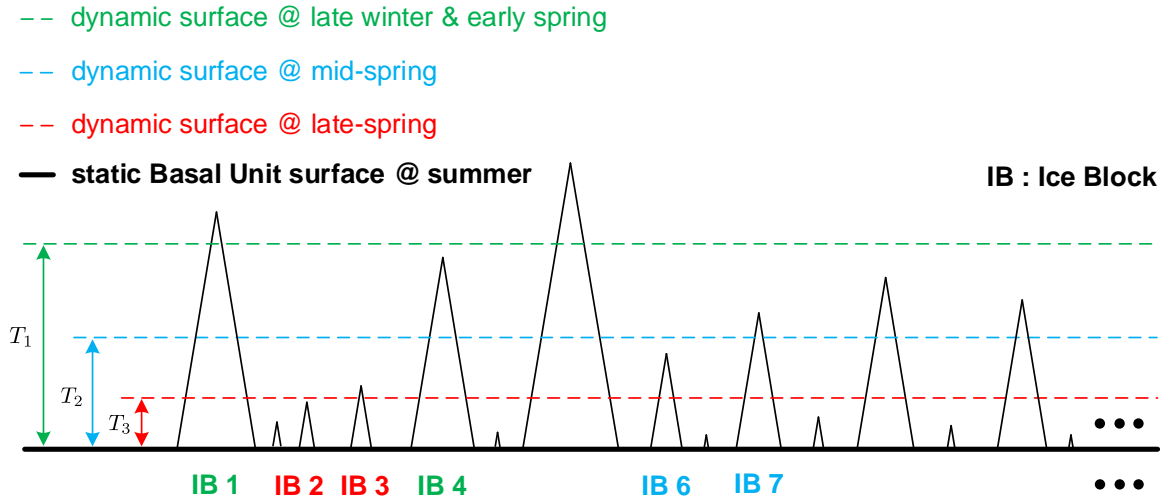


Figure 2: Illustration of an alternative and independent approach employed to constrain the depth of the seasonal deposits (“BOUNDing”). Instances of ice blocks of various sizes and heights are randomly placed over the Basal Unit. It should be noted that this plot is a simplified illustration as in reality smaller ice blocks are much more frequently observed than larger ones (Fanara et al., 2020b). Meanwhile, only peak-shaped ice blocks are presented so as we can assume no snow particles on top of the ice blocks.  $T_i$  denotes the varying thickness of the seasonal layer at different epochs.

341            Although HiRISE images without the impact of the polar hood can be acquired during  
 342 late winter and early spring, the outlines of the shadows cannot be unambiguously identified  
 343 due to unfavourable solar elevation angles, leading to failed application of the proposed “SUB-  
 344 TRACTing” approach. Meanwhile, the bundle adjustment can fail with images acquired in late  
 345 winter or early spring as small-scale features stay covered by the thick seasonal deposits.

346            Here we devise an independent approach for measuring the depth of the seasonal deposits,  
 347 which is capable of inferring the thickness during late winter and early spring (Figure 2). This  
 348 approach takes advantage of relatively large quantity of ice blocks that cluster in specific re-  
 349 gions (see the inset in Figure 5 for an example). The main idea behind it is that an ice block  
 350 that has been completely covered means that the thickness of the seasonal layer exceeds the  
 351 height of the ice block (a lower bound). Similarly, an ice block that has not been completely  
 352 covered means that the thickness of the seasonal layer is lower than the ice block height (an  
 353 upper bound). However, to place the strongest constraints, we have to locate the locally high-  
 354 est ice blocks that have been completely submerged and the locally lowest ice blocks that still

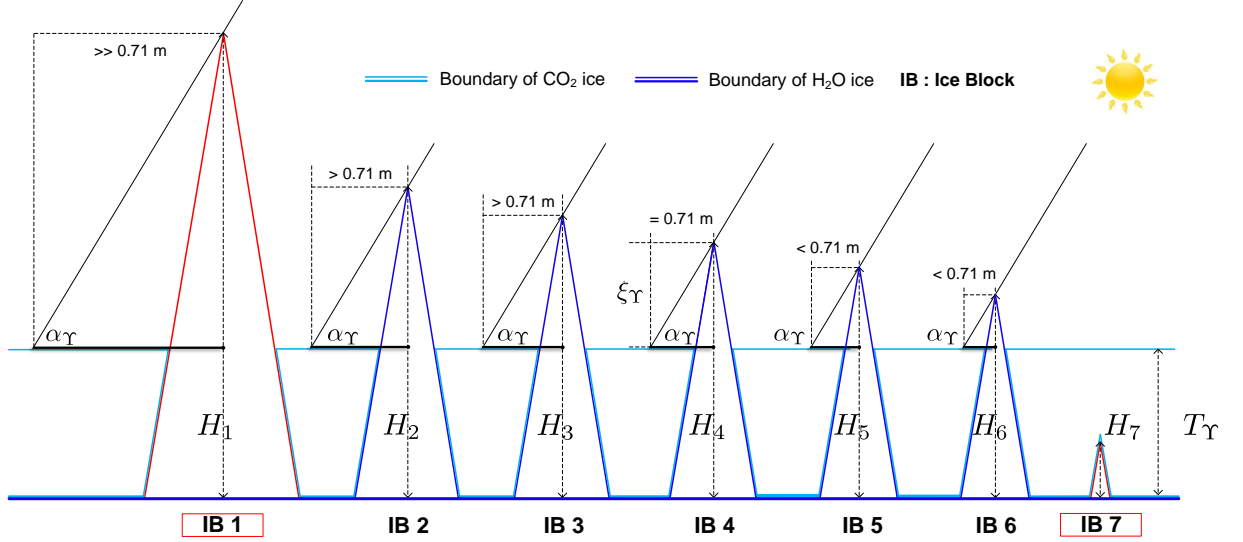


Figure 3: Schematic showing the offset inherited in the derived bounding constraints on the thickness of the seasonal layer at  $L_s = \Upsilon^\circ$  in late winter or spring from the “BOUNDING” approach. IBs 2 and 3 are examples of the locally smallest ice blocks visually determined to be uncovered by the seasonal layer to place upper bounds on its thickness ( $T_\Upsilon$ ). Meanwhile, IBs 5 and 6 are examples of the locally largest ice blocks visually identified to be completely covered with the aim to place the corresponding lower bounds. IBs 1 and 7 marked in red are representative ice blocks that are respectively too large and too small to put tight bounds on the thickness of the seasonal layer, which are thus not included in our analysis. The criterion by which we visually determine if an ice block is fully covered or not is if its shadow length is greater than the identification threshold of 2.83 pixels, or 0.71 m when the spatial resolution of the image is 0.25 m. Thus, the height of the bounding ice block during summertime ( $H_m$ ,  $m = 1, 2, 3, \dots, 7$ ) always offsets the thickness of the seasonal deposits by a magnitude of  $\xi_\Upsilon$ . This offset can be shown in the ideal case of IB 4 where its shadow length exactly equals the threshold of 2.83 pixels, which can then precisely constrain the seasonal deposits’ thickness to be  $T_\Upsilon = H_4 - \xi_\Upsilon$ . The offset, that is  $-\xi_\Upsilon$ , can be related to the spatial resolution of the image and the solar elevation angle as in Equation 10. The boundaries for different types of ices are just for illustration purposes as there also exists directly condensed and  $\text{CO}_2$ -snowfall-scavenged water ice within the seasonal deposits (Appéré et al., 2011; Alsaed & Hayne, 2022).

355 stick out the frozen layer. We only select peaked and triangular-prism-shaped ice blocks to min-  
 356 imize the impact of accumulation of snow particles over the ice blocks which otherwise can bias  
 357 the thickness inversion (Section 5.4). As shown in Figure 2, snow/ice deposits are deepest in  
 358 late winter and early spring with a thickness of  $T_1$ , then as the solar insolation increases with  
 359 time,  $\text{CO}_2$  starts to sublimate and the thickness starts to decline and reach  $T_2$  at mid-spring  
 360 and  $T_3$  in late spring, respectively. Surface is free of the seasonal layer during the adjacent sum-  
 361 mer where the heights of the ice blocks can be measured using the geometric model presented  
 362 in Section 2.2. For  $T_1$ , we can utilize IBs 4 and 1 to place the lower and upper bounds, respec-  
 363 tively. IB 4 is the locally highest ice block that has been completely covered during late win-  
 364 ter and early spring, and IB 1 is the locally lowest ice block that has not been completely sub-  
 365 merged. In a similar way, we can locate the ice blocks, marked using corresponding colors in  
 366 Figure 2, to place bounds on  $T_2$  and  $T_3$ , respectively. The mathematical expressions can be put  
 367 as follows:

$$368 \quad \begin{cases} T_1 \in [H_4, H_1] \\ T_2 \in [H_6, H_7] , \\ T_3 \in [H_2, H_3] \end{cases} \quad (9)$$

369 where  $H_m$  denotes the height of IB  $m$  measured in the adjacent summer. We term this alter-  
 370 native approach as “BOUNDing” for simplicity and to distinct it from the “SUBTRACTing”  
 371 approach that subtracts the ice block heights in the summer to that in the spring (Sections 2.3).

372 Attention should be drawn to the fact that the pixel size of HiRISE (down to 0.25 m) lim-  
 373 its the detection of shadows under 0.71 m in length ( $2\sqrt{2} = 2.83$  pixels). As such, when we  
 374 determine a locally shortest ice block that has not been completely submerged or a locally tallest  
 375 ice block that has been completely covered, it has already stuck out the seasonal layer at least  
 376 or at most by

$$377 \quad \xi_{\Upsilon} = 2\sqrt{2} \times sr \times \tan \alpha_{\Upsilon} . \quad (10)$$

378 Here,  $\xi_{\Upsilon}$  denotes magnitude of the offset at  $L_s = \Upsilon^\circ$  during late winter or spring. The variable  
 379  $sr$  represents the spatial resolution of the images which is mostly 0.25 m but can also be 0.5 m  
 380 for that acquired in late winter and early spring. The symbol  $\alpha_{\Upsilon}$  denotes the solar elevation  
 381 angle at the acquisition of the image with seasonal snow/ice cover. A schematic illustrating the  
 382 offset is shown in Figure 3. We correct the derived thickness bounds for the offset of  $-\xi_{\Upsilon}$  oth-  
 383 erwise they would be systematically higher than that derived from the “SUBTRACTing” ap-  
 384 proach.

385 For illustration purposes, abstract probability distributions of bounding constraints at spe-  
 386 cific solar longitudes are computed using the Kernel Density Estimation (KDE; Silverman, 1986).  
 387 In our case, we perform the KDE process using the Gaussian kernel ( $\kappa$ ) and use the Silverman’s  
 388 rule to compute an optimal bandwidth of  $\sigma$  to ensure moderate smoothness of the obtained den-

389 sity distribution:

$$390 \quad \rho_{\kappa}(x) = \frac{1}{N\sigma} \sum_{i=1}^N \kappa(x - x_j; \sigma) \quad \text{with} \quad \kappa(x; \sigma) \propto \exp\left(-\frac{x^2}{2\sigma^2}\right), \quad (11)$$

391 where  $N$  is the total number of ice block height measurements, that is  $x_j$ , used to set upper  
 392 or lower limits on the seasonal snow/ice depth. Violin plots are used for visualization purpose.  
 393 We have also tried the Improved Sheather Jones (ISJ) algorithm for choosing the bandwidth  
 394 which should be used when data is far from normal or multimodal (Botev et al., 2010). Un-  
 395 fortunately, the limited number of available constraints in our case prevents its effective appli-  
 396 cation.

397 For statistically significant number of constraints, the thickness of the seasonal deposits  
 398 at a specific solar longitude can be expected to fall within the interval formed by medians of  
 399 the lower and upper bounds. To obtain more realistic uncertainty estimates, we take the stan-  
 400 dard errors of the median bounds into consideration using a scaled Median Absolute Deviation  
 401 (SMAD; Leys et al., 2013). The SMAD is related to the median of the absolute deviations from  
 402 the samples' median as

$$403 \quad \text{SMAD}_{\Upsilon} = sf \times \text{Md} [|\mathbf{T}_{\Upsilon} - \text{Md}[\mathbf{T}_{\Upsilon}]|], \quad (12)$$

404 where  $\mathbf{T}_{\Upsilon}$  denotes the sample vector which contains all the thickness constraints at  $\text{Ls} = \Upsilon^{\circ}$   
 405 in late winter or spring,  $\text{Md}[\ ]$  is the median operator, and  $sf = 1.4826$  is the scale factor. The  
 406 scaled metric can be treated as a consistent estimator similar to the standard deviation of a Gaus-  
 407 sian distribution. We extend the median lower bound downwards and the median upper bound  
 408 upwards to obtain the adjusted bounding range:

$$409 \quad \Theta_{\Upsilon}^{\text{T}} = \left[ \text{Md}_{\Upsilon\_lb} - \frac{3 \times \text{SMAD}_{\Upsilon\_lb}}{\sqrt{N_{\Upsilon\_lb}}}, \text{Md}_{\Upsilon\_ub} + \frac{3 \times \text{SMAD}_{\Upsilon\_ub}}{\sqrt{N_{\Upsilon\_ub}}} \right], \quad (13)$$

410 where  $\text{Md}_{\Upsilon\_lb}$  and  $\text{Md}_{\Upsilon\_ub}$  denote the medians of the lower and upper bounds at  $\text{Ls} = \Upsilon^{\circ}$ ,  
 411 respectively. Meanwhile,  $N_{\Upsilon\_lb}$  and  $N_{\Upsilon\_ub}$  denote the number of available lower and upper  
 412 bounds at  $\text{Ls} = \Upsilon^{\circ}$ , respectively.

### 413 3 Study area

414 Ice blocks analyzed in this study lie at the bottom of an equator-facing steep scarp. The  
 415 scarp is centered at (85.0°N, 151.5°E) with a total length of  $\sim 20$  km (refer to its location in Fig-  
 416 ure 4). This scarp is the same as that studied in Su, Fanara, Zhang, et al. (2023) and termed  
 417 Scarp 1. The scarp is visually distinguishable by its bright water ice layers (Figure 5). The rel-  
 418 atively flat top of the NPLDs features a residual layer of mostly dust-free water ice and can grow  
 419 to a few meters at most (Figure 4). Over the surface a homogeneous pitted texture at length  
 420 scales of 10 to 20 m is revealed, which appears to be the result of differential sublimation. Fallen  
 421 ice blocks from the steep scarp reside at the surface of the Basal Unit. A typical example of  
 422 a clustering of ice blocks is shown in Figure 5. The Basal Unit is a low-albedo, interbedded sandy  
 423 and icy deposits that lie stratigraphically below the NPLDs (Grima et al., 2009; T. Brothers

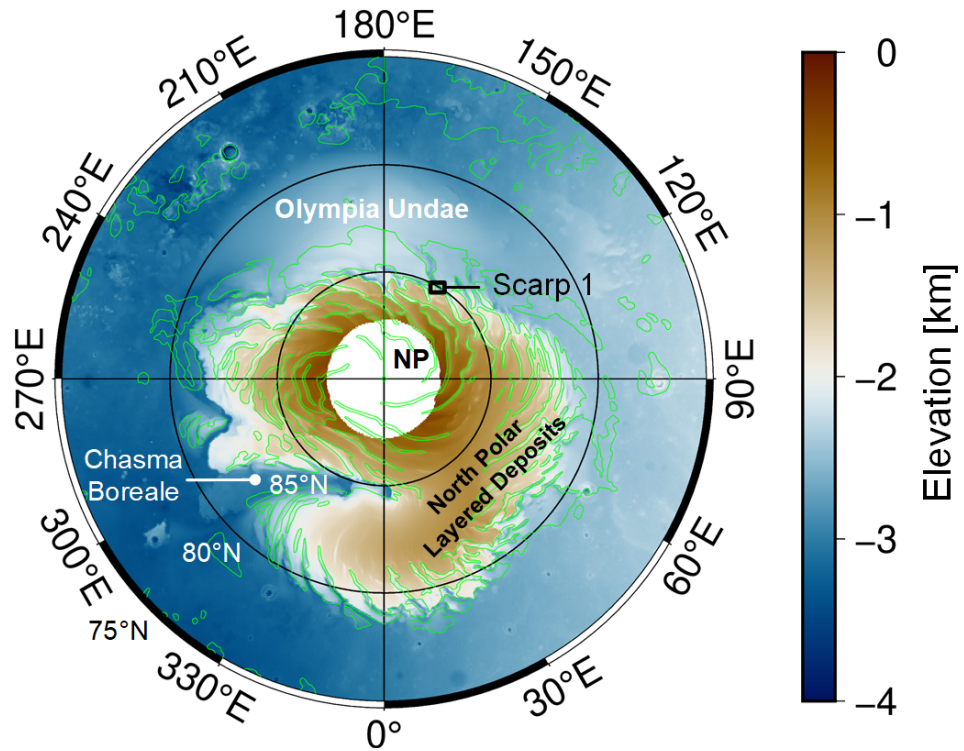


Figure 4: Topography of the Martian North Pole represented by the reference DEM from re-processed and then self-registered MOLA altimetric profiles (Xiao, Stark, Schmidt, et al., 2021). The elevation is referenced to a Martian ellipsoid with an equatorial radius of 3,396.19 km and a mean polar radius of 3,376.20 km. The missing coverage poleward of 87°N is due to a lack of nadir-pointing profiles, a limitation related to the orbital inclination of the spacecraft. The map projection is north polar stereographic, with coverage poleward of 75°N and a spatial resolution of 1 km/pixel. The Residual North Polar Cap (green polygons), Chasma Boreale, and the study site (Scarp 1) are marked.

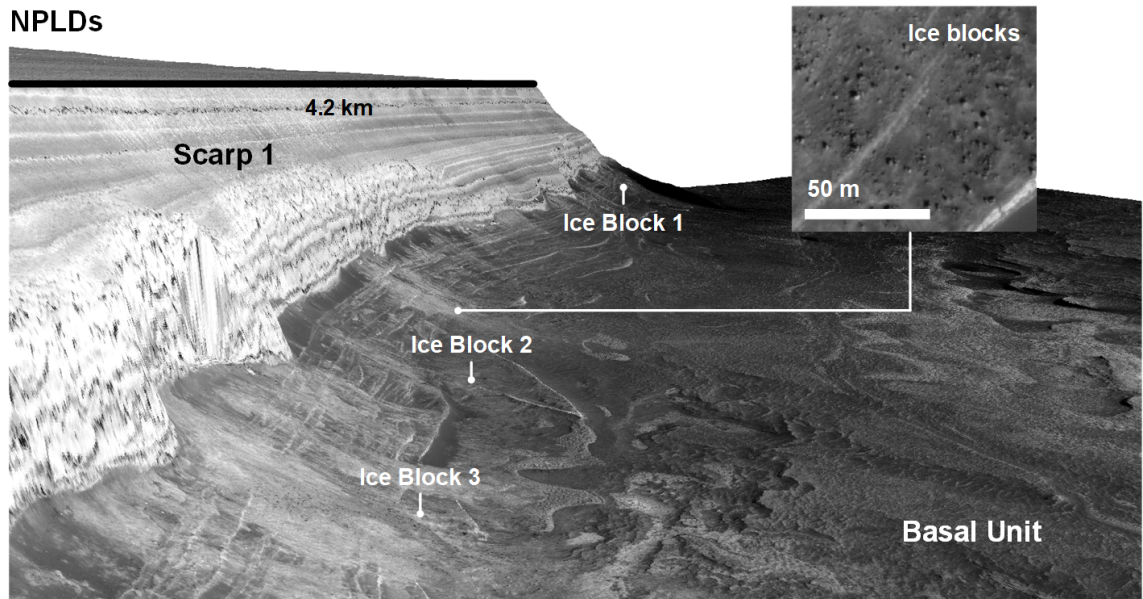


Figure 5: Illustration of the NPLDs and ice blocks at the foot of the steep scarp (Scarp 1) by a 3D view with the HiRISE image acquired during the summertime of MY29 (PSP\_009648\_2650\_RED) draped on the HiRISE DEM generated in this study (no vertical exaggeration). Elevation difference from top of the NPLDs to the Basal Unit at the bottom is  $\sim 600$  m. Site is centered at  $(85.0^{\circ}\text{N}, 151.5^{\circ}\text{E})$ . Wide patches and aprons of debris are readily visible at the foot of the scarp. Inset map shows typical examples of ice blocks at foot of the scarp. It should be noted that the Basal Unit outcrops where ice blocks reside can still feature significant terrain slope (up to  $\sim 30^{\circ}$ ). We mark the locations of Ice Blocks 1, 2, and 3 used for the purpose of this study. For reference, the distance between Ice Blocks 1 and 3 is 4,564 m.

424 et al., 2015), and may be one of the largest reservoirs of water-ice on Mars after the PLDs (Ojha  
425 et al., 2019). The Basal Unit outcrops beneath Scarp 1 belong to the Cavi unit where it tran-  
426 sitions into the NPLDs (S. Brothers et al., 2018; Nerozzi et al., 2022). Although the majority  
427 of the ice blocks originate from steep scarps of the NPLDs, some of them can also source from  
428 the upper part of the Basal Unit with a slope of up to  $30^\circ$  (Su, Fanara, Zhang, et al., 2023).

## 429 4 Results

### 430 4.1 Bundle adjustment, DEM generation, and image orthorectification

431 A total of 50 images are available for Ice Blocks 1, 2, and 3 with a pixel size ranging from  
432 0.25 m (39) to 0.50 m (11). Most of them (33) were acquired from 2010 to 2013 (MY30 – 32)  
433 with the earliest coverage extended to 2008 (MY29) and the latest ones taken during 2021 (MY36).  
434 These images are bundled adjusted all together. Unfortunately, the bundle adjustment fails to  
435 rectify 8 images acquired in late winter or early spring when the seasonal layer is thick, due to  
436 a lack of small-scale features and “distorted” feature shapes owing to distinct illumination con-  
437 ditions with respect to the rest of the images. Then, the stereo pair ESP\_018905\_2650\_RED and  
438 ESP\_019222\_2650\_RED acquired on 8 August 2010 and 2 September 2010 in the summer of MY30  
439 is used to create a DEM (the same pair as used in Su, Fanara, Zhang, et al. (2023)). The stereo  
440 pair respectively imaged the Scarp 1 area with spacecraft rolls of  $-3.6^\circ$  and  $-15.5^\circ$  to achieve  
441 a good base-to-height ratio for the purpose of obtaining a reliable 3D model of the surface. The  
442 emission angles for these two images are  $4.0^\circ$  and  $17.0^\circ$ , respectively. These images were acquired  
443 relatively close in time, with an interval of 25 Earth days, which can minimize differences in  
444 solar illumination and surface properties between the stereo pairs. Similarities between the stereo  
445 pair can aid in the image matching and parallax determination processes to reconstruct the ob-  
446 ject heights. The DEM is gridded with  $1 \times 1$  m pixels (Figure 5). Limited interpolation spikes  
447 and long lines due to CCD seams have been spotted while inspecting the hillshade generated  
448 from the DEM, verifying the correctness and reliability of the bundle adjustment and image  
449 matching processes. The bundled-adjusted images are then automatically orthorectified using  
450 the aforementioned DEM and used for measurements of the shadows. Visual examination of  
451 the orthorectified images show they mutually align well at their overlapping portions. In com-  
452 bination with solar conditions at the acquisition times of the images, local slope and aspect are  
453 extracted from this DEM for converting the shadow length variations to temporal thickness evo-  
454 lution of the seasonal  $\text{CO}_2$  layer.

### 455 4.2 Snow/ice thickness in middle-to-late spring from “SUBTRACTing”

456 We identify three reference ice blocks at Scarp 1 for the purpose of measuring the seasonal  
457 snow/ice depth evolution at these specific spots. All of these three ice blocks meet the eligibil-  
458 ity criteria. Meanwhile, they are capable of yielding the largest number of reliable and self-consistent  
459 thickness measurements among 10 candidates. The other ice blocks are not included in our anal-

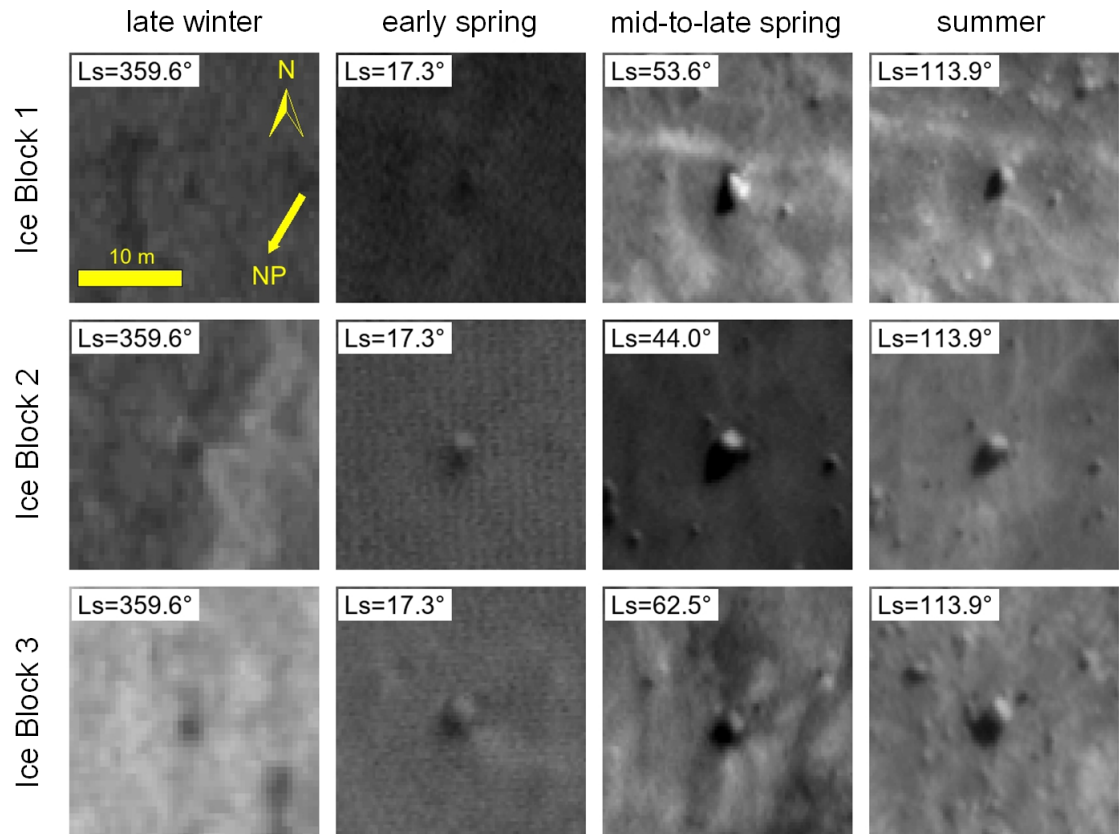


Figure 6: Images of Ice Blocks 1, 2, and 3 (centered at the sub-frames) during different seasons from late winter to summer. The images used are `ESP_032856_2650_RED` at  $L_s = 359.6^\circ$  in MY31, `ESP_024509_2650_RED` at  $L_s = 17.3^\circ$  in MY31, `ESP_016439_2650_RED` at  $L_s = 44.0^\circ$  in MY30, `ESP_016716_2650_RED` at  $L_s = 53.6^\circ$  in MY30, `ESP_034610_2650_RED` at  $L_s = 62.5^\circ$  in MY32, and `ESP_053730_2650_RED` at  $L_s = 113.9^\circ$  in MY34, respectively. The projection adopted is polar stereographic centered at the North Pole. The north of the projected map and direction to the North Pole are marked. Illumination is to the bottom-left corner. Note that ice blocks in springtime feature no circumferential shadows that are indicative of moating.

460 ysis due to large oscillations of the measured thicknesses there and wider temporal gaps between  
 461 them. We term the selected three ice blocks as Ice Block 1 (84.984°N, 151.907°E), Ice Block 2  
 462 (85.006°N, 151.231°E), and Ice Block 3 (85.008°N, 151.072°E), respectively. Refer to Figure 5  
 463 for their locations. The distance between Ice Blocks 1 and 2 is 3,745 m, 832 m between Ice Blocks 2  
 464 and 3, and 4,564 m between Ice Blocks 1 and 3. Regional slope at Ice Blocks 1, 2, and 3 are  
 465 around 11°, 2.5°, and 6°, which are generally gentle compared to that right at the foot of the  
 466 scarp which can be up to 30°. This can be conceived as ice blocks tend to stop and reside where  
 467 terrain is flat or when barricaded by obstacles along their paths. Typical HiRISE images of these  
 468 ice blocks from late winter and spring, when the surface is covered with seasonal deposits, to  
 469 summer, when the seasonal layer completely sublimates away, are shown in Figure 6. Ice Block 3  
 470 is triangular-prism-shaped while the other two feature clear peaks. Ice Blocks 1, 2, and 3 are  
 471 relatively stable over MY29 to MY36, with average summer heights of  $\sim 1.2$  m,  $\sim 1.4$  m, and  
 472  $\sim 1.8$  m, respectively (Section 5.1). During late winter, with the Sun being less than  $\sim 5^\circ$  above  
 473 the horizon, the CO<sub>2</sub> snow/ice is the thickest. Significant portion of the ice blocks are submerged  
 474 by the seasonal deposits, and there exists no clear and unique identification of their cast shad-  
 475 ows. This situation does not improve much at the very early of spring and only until early-to-  
 476 mid spring, when the deposits gradually sublimate back to the atmosphere, we can unambigu-  
 477 ously distinct the shadows of the target ice blocks from the background. Continuing into the  
 478 summer, the surface is entirely free of the seasonal deposits and the surrounding smaller ice blocks  
 479 reappear.

480 At Ice Block 1, the images used, solar and slope conditions, along with the ice block heights  
 481 and seasonal snow/ice depth are summarized in Table S1. The number of valid measurements  
 482 during northern spring can vary from three in MY32 and MY36 and five in MY31 to six in MY30.  
 483 All measurements except for one in MY31 fall within 35° and 70° in solar longitude. Some ob-  
 484 servations during the springtime have been excluded in the analysis due to bad image quality  
 485 or no clear identification of the shadows. The curves generally feature decreasing trends, con-  
 486 sistent with the phenomenon that during spring the sun rises above the horizon and the solar  
 487 insolation increases with time. It is interesting to note that MY30/32 and MY31/36 share sim-  
 488 ilar patterns, respectively. However, both patterns reach a thickness of  $\sim 0.35$  m at around Ls =  
 489 37.5°. The maximum difference between these two patterns is limited to be within  $\sim 0.2$  m. The  
 490 uncertainty of the thickness inversion is about 0.11 m as illustrated in Section 5.1, these inter-  
 491 annual differences could thus not be confirmed from a statistical point of view. For Ice Blocks 2  
 492 and 3, the images used, solar and slope conditions, along with the ice block heights and snow/ice  
 493 depth are summarized in Tables S2 and S3, respectively. Their thickness evolution results are  
 494 shown in Figure 7. They share similar trends with that of Ice Block 1, although the interan-  
 495 nual dispersions are much more obvious than that of Ice Block 1 (but still limited to be less than  
 496  $\sim 0.2$  m). The depth inversion uncertainties at these two ice blocks are 0.10 m and 0.16 m, re-  
 497 spectively (Section 5.1). Thus, these multiyear variations could not be confidently confirmed.  
 498 For all of the three ice blocks, the earliest measurements fall within 20° and 25° in solar lon-

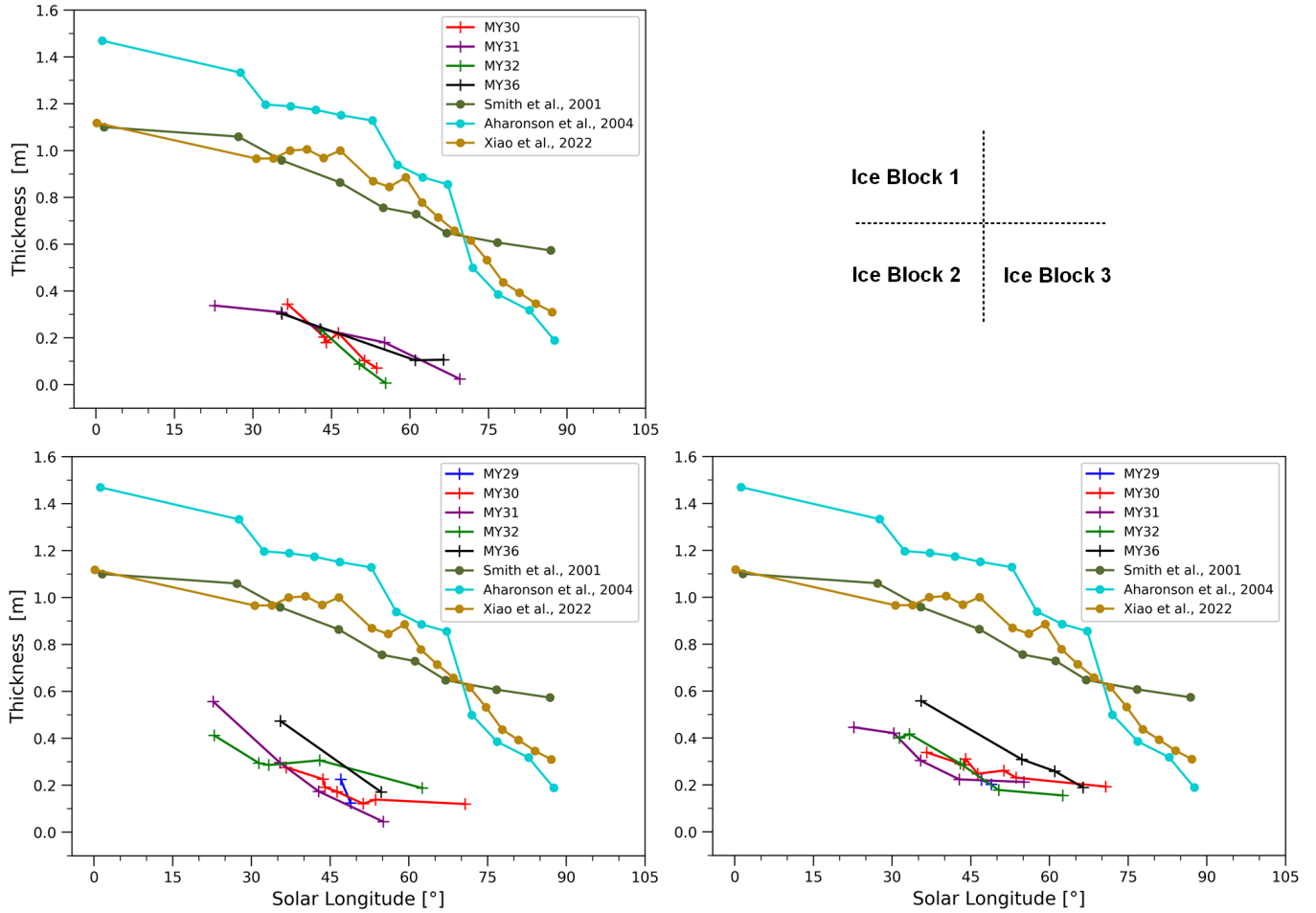


Figure 7: Upper left: Seasonal snow/ice thickness from MY30 to MY36 for Ice Block 1 at Scarp 1 (85.053°N, 151.833°E) during the northern spring. Bottom left: Seasonal snow/ice thickness evolution from MY29 to MY36 for Ice Block 2. Bottom right: Seasonal snow/ice thickness evolution from MY29 to MY36 for Ice Block 3. Measurements from this study are marked by crosses, and previous MOLA results are marked by dots. It should be noted that for [D. E. Smith et al. \(2001\)](#), the result shown is along the latitudinal annulus centered at 85.5°N. For [Aharonson et al. \(2004\)](#), it is the latitudinal annulus centered at 86°N.

500 gitude. There are images acquired in late winter and early spring, but as the elevation angle  
 501 of the solar rays is less than  $10^\circ$ , the images are dimly-lit and attempts to measure the shadow  
 502 length have failed. Furthermore, the bundle adjustment of these images can fail and no orthorec-  
 503 tified versions are available for the measurements. These issues can be circumvented by the “BOUND-  
 504 ing” approach for which the thickness measurements are extended to cover late winter and early

505 Three previous MOLA results in the springtime of MY25, that is, [D. E. Smith et al. \(2001\)](#)  
 506 at the latitudinal annulus  $85.5^\circ\text{N}$ , [Aharonson et al. \(2004\)](#) at the latitudinal annulus  $86^\circ\text{N}$ , and  
 507 [Xiao, Stark, Schmidt, Hao, Steinbrügge, et al. \(2022\)](#) at the grid element centered at ( $85^\circ\text{N}$ ,  $155^\circ\text{E}$ )  
 508 and of size  $0.5^\circ$  in latitude and  $10^\circ$  in longitude are shown for comparison (Figure 7). Before  
 509  $L_s = 70^\circ$ , the results from [D. E. Smith et al. \(2001\)](#) and [Xiao, Stark, Schmidt, Hao, Steinbrügge,](#)  
 510 [et al. \(2022\)](#) are generally consistent with each other, with a maximum thickness of  $\sim 1.1$  m at  
 511 the beginning of spring and declining with time. Interestingly, all of the MOLA results consis-  
 512 tently predicted a depth of  $\sim 0.64$  m at around  $L_s = 70^\circ$ , before which the thickness measure-  
 513 ments of [Aharonson et al. \(2004\)](#) are consistently the largest. When approaching summer sol-  
 514 stance ( $L_s = 90^\circ$ ), all of the MOLA results feature non-zero thickness values, with that of [D. E. Smith](#)  
 515 [et al. \(2001\)](#) being as high as  $\sim 0.6$  m. These deviations are considered outliers due to biases  
 516 in the MOLA results as discussed in Section 5.5. Surprisingly, these MOLA results are consis-  
 517 tently higher, by a magnitude of up to  $\sim 1$  m, than our measurements using shadows of the ice  
 518 blocks. However, it should be noted that at this point the effects of direct condensation onto  
 519 the tops of the ice blocks have not been considered, and the thickness measurements can be viewed  
 520 as that contributed solely by snowfalls. These aspects are thoroughly discussed in Section 5.4.  
 521 Possible explanations of the remaining offsets after the correction for these effects are exam-  
 522 ined in Section 5.5.

### 523 4.3 Snow/ice thickness in late winter and spring from “BOUNDing”

524 At Scarp 1, HiRISE images taken in late winter are available only in MY31. Thus, we ap-  
 525 ply the “BOUNDing” approach to all the images in MY31 with an attempt to place bounds on  
 526 the snow/ice thickness all the way from late winter to spring, at solar longitudes of  $7.0^\circ$ ,  $17.3^\circ$ ,  
 527  $22.7^\circ$ ,  $30.3^\circ$ ,  $35.4^\circ$ ,  $42.8^\circ$ ,  $55.1^\circ$ ,  $69.5^\circ$ , and  $350.7^\circ$ , respectively. The corresponding images are  
 528 ESP\_024232\_2650\_RED, ESP\_024509\_2650\_RED, ESP\_024654\_2650\_RED, ESP\_024865\_2650\_RED,  
 529 ESP\_025010\_2650\_RED, ESP\_025221\_2650\_RED, ESP\_025577\_2650\_RED, ESP\_025999\_2650\_RED,  
 530 and ESP\_032632\_2650\_RED, respectively. The solar elevation angles during acquisitions of these  
 531 images are  $7.9^\circ$ ,  $12.2^\circ$ ,  $14.3^\circ$ ,  $17.3^\circ$ ,  $19.2^\circ$ ,  $21.7^\circ$ ,  $25.3^\circ$ ,  $28.3^\circ$ , and  $0.9^\circ$  (late winter), respectively.  
 532 The results obtained during late winter and early spring serve the purpose of filling the tem-  
 533 poral gap of the “SUBTRACTing”-derived results. Meanwhile, the results obtained during mid-  
 534 to-late spring can cross-validate the “SUBTRACTing”-derived results and check if the thick-  
 535 ness measurements obtained at Scarp 1 are indeed much lower than the MOLA-derived values.

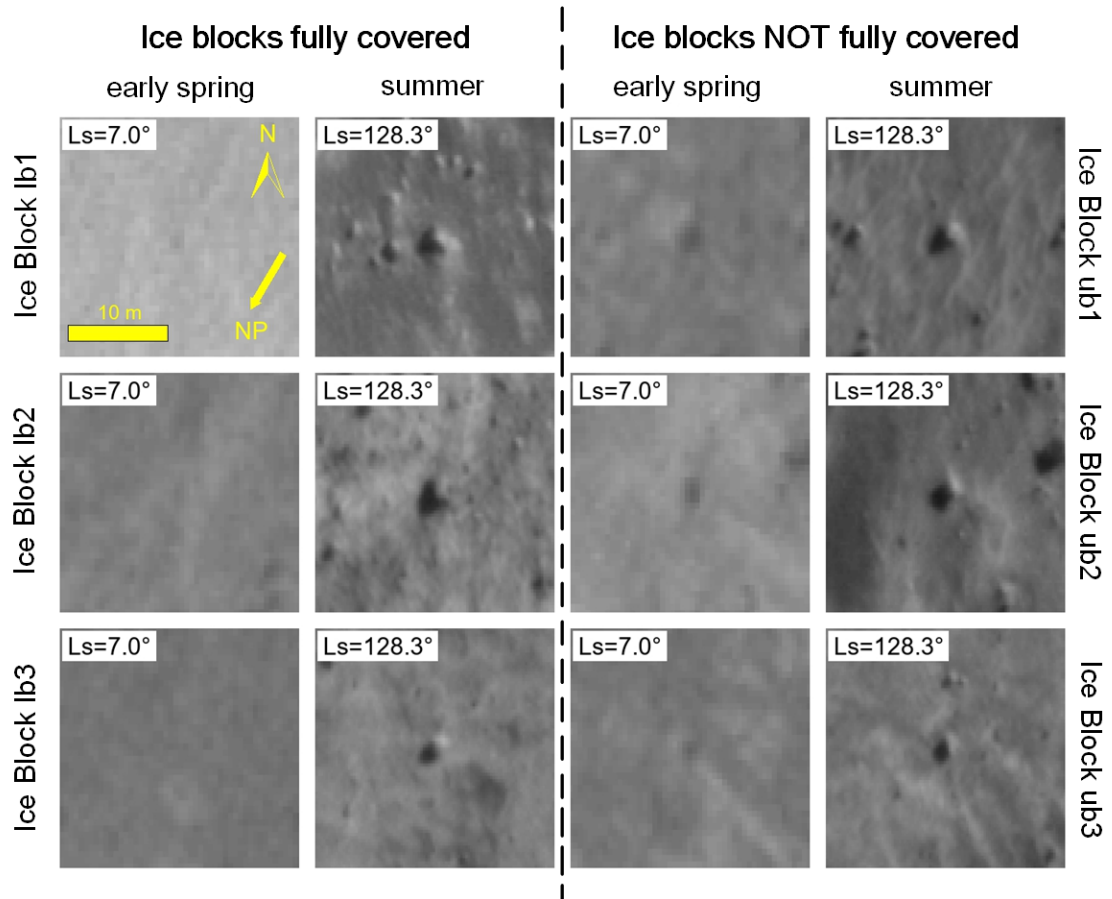


Figure 8: Images of example bounding ice blocks (centered at the sub-frames) at  $L_s = 7.0^\circ$  in early spring and  $L_s = 128.3^\circ$  in summer in MY31, respectively. The images used are ESP\_024232\_2650\_RED and ESP\_027674\_2650\_RED, respectively. These ice blocks are utilized to place bounds on the thickness of the seasonal snow/ice cover at  $L_s = 7.0^\circ$ . The subscript “lb” means the ice block has been totally submerged and is capable of placing a lower bound on the thickness. Similarly, the subscript “ub” indicates the ice block in question has not been completely submerged and is capable of placing an upper bound on the thickness. Map projection and scale are as in Figure 6. Illumination is to the bottom-left corner.

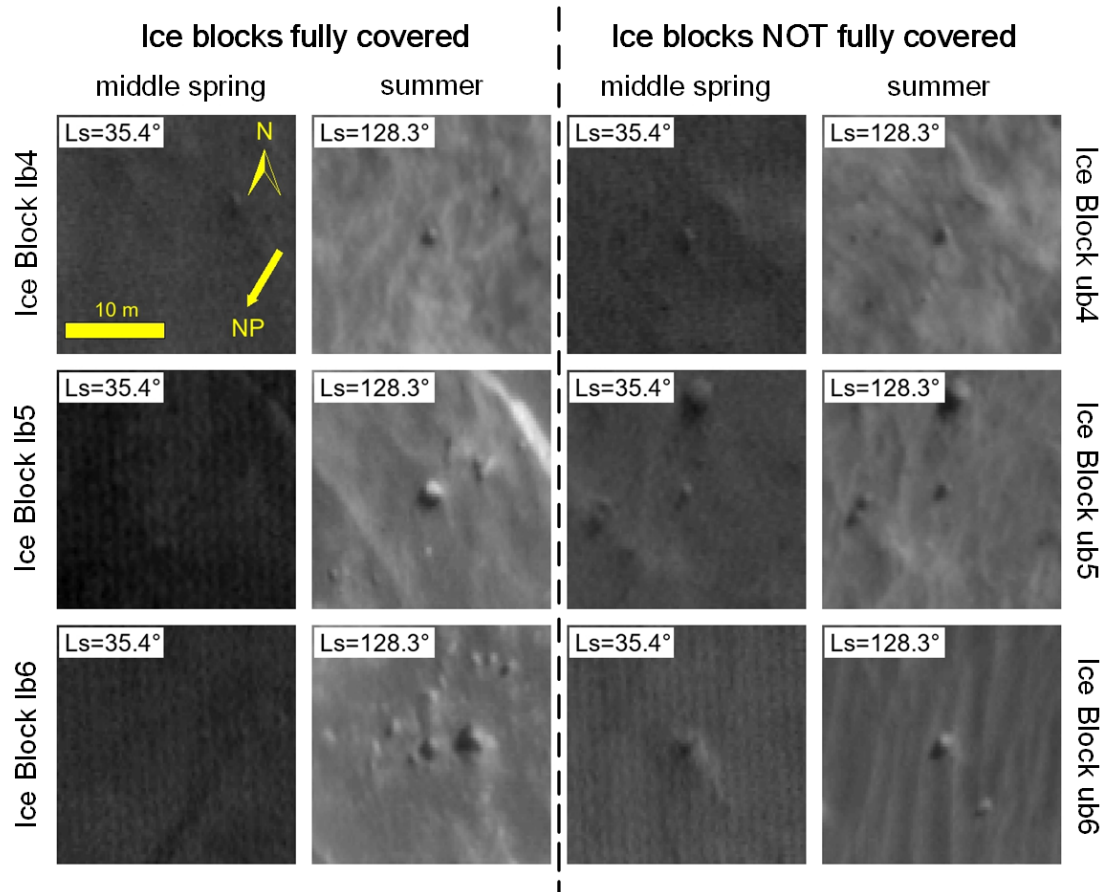


Figure 9: Images of three example bounding ice blocks (centered at the sub-frames) at  $L_s = 35.4^\circ$  in middle spring and  $L_s = 128.3^\circ$  in summer in MY31, respectively. The images used are ESP\_025010\_2650\_RED and ESP\_027674\_2650\_RED, respectively. These ice blocks are utilized to place bounds on the thickness of the seasonal snow/ice cover at  $L_s = 35.4^\circ$ . Map properties and meaning of the subscripts in the ice block names are as in Figures 6 and 8. Illumination is to the bottom-left corner.

536 For late winter and early spring images acquired at  $L_s = 7.0^\circ$ ,  $L_s = 17.3^\circ$ , and  $L_s = 350.7^\circ$   
 537 that fail to be rectified during the bundle adjustment and subsequent orthorectification, we geo-  
 538 reference them to the summer image taken at  $L_s = 128.3^\circ$  in MY31 (ESP\_027674\_2650\_RED).  
 539 For this purpose, we select a total of around 10 control points that are homogeneously distributed  
 540 over the image. These tie points are chosen to be stable ice blocks, corner points of protrusions  
 541 from layers of the icy stratigraphy in the scarp, and large-scale topographic features over the  
 542 Basal Unit outcrops. The affine transformation is then applied to tie these image to the sum-  
 543 mer one when is free of the seasonal layer. We proceed to select the locally tallest ice blocks,  
 544 that is, with the longest shadows, and locally shortest ice blocks over Scarp 1. After that, the  
 545 heights of these bounding ice blocks are measured in the summer image and serve as constraints  
 546 on the seasonal snow/ice depth.

547 For demonstration purpose, we show example ice blocks used to bound the thickness of  
 548 the seasonal cover at  $L_s = 7.0^\circ$  in early spring and  $L_s = 35.4^\circ$  in middle spring in MY31, re-  
 549 spectively. At  $L_s = 7.0^\circ$ , we display three example ice blocks that have been fully submerged,  
 550 termed Ice Blocks lb1, lb2, and lb3, which can then indicate the minimum snow/ice depth in  
 551 the Scarp 1 region (left panel in Figure 8). During the early spring, images reveal no texture  
 552 related to the underlying ice blocks, demonstrating that the ice blocks have been completely  
 553 buried underneath. Their heights measured in the subsequent summer when surface is free of  
 554 seasonal deposits stand at 0.97 m, 1.02 m, and 0.93 m, respectively. After the correction of  $-\xi_\gamma =$   
 555  $-0.20$  m, these values become 0.77 m, 0.82 m, and 0.73 m, respectively. We proceed to show-  
 556 case three other ice blocks that have not been fully submerged, named Ice Blocks ub1, ub2, and  
 557 ub3, and hence can put upper limits on the snow/ice depth (right panel in Figure 8). Their heights  
 558 measured at the coming summer stand at 1.20 m, 1.12 m, and 1.10 m, respectively. After the  
 559 correction of  $-\xi_\gamma = -0.20$  m, these values become 1.00 m, 0.92 m, and 0.90 m, respectively.  
 560 These lower and upper bounds are extremely self-consistent with mean values of 0.77 m and  
 561 0.94 m, respectively. Thus, thickness of the seasonal layer at  $L_s = 7.0^\circ$  is most likely to be within  
 562 0.77 m to 0.94 m. At  $L_s = 35.4^\circ$  during middle spring in MY31, we show three example ice  
 563 blocks that have been fully submerged, termed Ice Blocks lb4, lb5, and lb6, respectively. Their  
 564 heights can place lower limits on the snow/ice depth in the Scarp 1 region (left panel in Fig-  
 565 ure 9). Their heights measured at the coming summer stand at 0.53 m, 0.61 m, and 0.56 m,  
 566 respectively. After the correction of  $-\xi_\gamma = -0.25$  m, these values become 0.28 m, 0.36 m, and  
 567 0.31 m, respectively. We then illustrate three other example ice blocks that have not been fully  
 568 submerged, named Ice Blocks ub4, ub5, and ub6, and hence can render indication as to the max-  
 569 imum snow/ice depth (right panel in Figure 9). Their heights measured at the coming sum-  
 570 mer are 0.64 m, 0.64 m, and 0.70 m, respectively. After the correction of  $-\xi_\gamma = -0.25$  m, these  
 571 values become 0.39 m, 0.39 m, and 0.45 m, respectively. These bounding values are largely self-  
 572 consistent with deviations of less than 0.1 m. Thickness of the seasonal layer at  $L_s = 35.4^\circ$   
 573 is most likely to be within 0.32 m to 0.41 m.

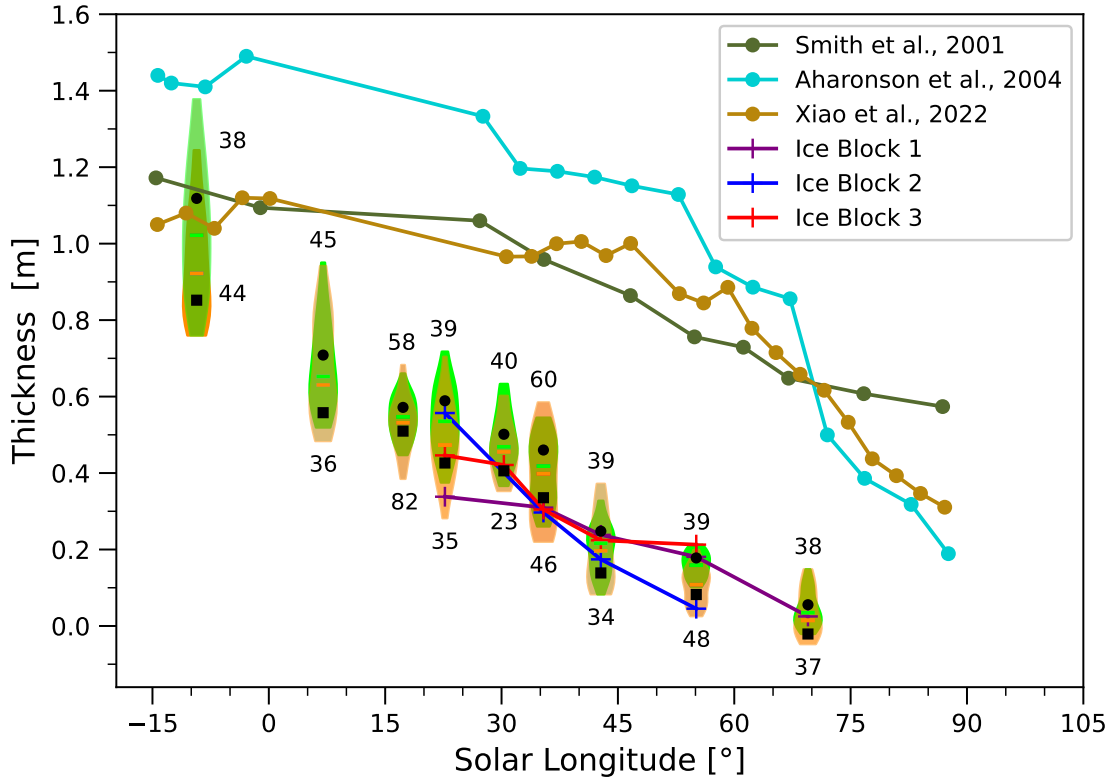


Figure 10: Results from both “SUBTRACTing” and “BOUNDing” in MY31, and their comparison to the existing MOLA results. The “SUBTRACTing” results for Ice Blocks 1, 2, and 3 are marked by crosses and connected by broken lines. The “BOUNDing” results have been corrected for the offset of  $-\xi_{\tau}$ , and are represented by the violin plots with medians of the upper and lower limits shown as horizontal lines. Upper bounds shown in lime while lower bounds in orange, and the corresponding number of bounding ice blocks adopted are marked alongside the violin plots. Black squares and dots denote adjusted bounds in consideration of the standard errors of the median constraints. For simplicity and temporal continuity, the constraints obtained at  $L_s = 350.7^\circ$  in late winter are plotted at  $L_s = -9.3^\circ$ .

574 The bounding ice blocks used are quasi-uniformly distributed along Scarp 1 between 150.82°E  
 575 and 151.95°E in longitude (Figure S2). Majority of them horizontally fall within 100 m to 600 m  
 576 away from the foot of the scarp. The number of bounding ice blocks used at each solar longi-  
 577 tude ranges from 23 at  $L_s = 30.3^\circ$  to 82 at  $L_s = 17.3^\circ$  (marked in Figure 10). The resulting  
 578 correction of  $-\xi_\gamma$  ranges from  $-0.02$  m at  $L_s = 350.7^\circ$  to  $-0.38$  m at  $L_s = 69.5^\circ$ . The cor-  
 579 rected results from “BOUNDing” in MY31, in comparison to that from “SUBTRACTing” in MY31  
 580 and MOLA dataset in MY25, are shown in Figure 10. Note that the “SUBTRACTing” yield  
 581 results for Ice Blocks 1, 2, and 3 (Section 4.2), while the “BOUNDing” results represent large-  
 582 scale average constrains measured at tens of bounding ice blocks distributed over Scarp 1 (Fig-  
 583 ure S2). Ice Blocks 1, 2, and 3, at more than 1.2 m, are much higher than that of the bound-  
 584 ing ice blocks, which are at a similar level with depth of the seasonal deposits to be constrained.  
 585 The “BOUNDing” approach can yield estimates in late winter and early spring while “SUBTRACT-  
 586 ing” are temporally limited to mid-to-late spring. Thickness bounded by median limits are high-  
 587 est during late winter with values most likely falling between 0.92 m and 1.02 m at  $L_s = 350.7^\circ$ ,  
 588 then that decrease to be between 0.63 m and 0.65 m at  $L_s = 7.0^\circ$  in early spring, between 0.20 m  
 589 and 0.22 m at  $L_s = 42.8^\circ$  in middle spring, and gradually decrease to be within 0.01 m and  
 590 0.03 m at  $L_s = 69.5^\circ$  in late spring. The thin layer at  $L_s = 69.5^\circ$  is not in conflict with the  
 591 statement of Piqueux et al. (2015) that the area of the SNPC shrunk to zero at around  $L_s =$   
 592  $80^\circ$  in MY31. Differences between upper and lower limits are smaller than 0.1 m at all exam-  
 593 ined solar longitudes, demonstrating the high precision of the average thickness estimates from  
 594 “BOUNDing” approach. Apart from shadow length measurement errors and the inclusion of  
 595 overly tall (in the uncovered case) or short (in the completely covered case) bounding ice blocks,  
 596 dispersion of the thickness constraints at each examined solar longitude can to some extent re-  
 597 flect regional variability of the snow/ice depth. The bulk upper and lower constraints overlap  
 598 well at all examined solar longitudes. This can be partially attributed to, other than the afore-  
 599 mentioned factors, the tendency that ice blocks used to derive lower bounds are more likely to  
 600 be located where feature thicker snow/ice cover, while that for generating the upper bounds  
 601 more frequently fall within regions with shallower snow/ice deposits. The adjusted bounds tak-  
 602 ing into consideration of the standard errors of the medians from Equation 13 are represented  
 603 by black squares and dots in Figure 10, respectively. The updated bounding intervals feature  
 604 half ranges from 0.03 m at  $L_s = 17.3^\circ$  to 0.13 m at  $L_s = 350.7^\circ$ , and with typical values of  
 605  $\sim 0.05$  m (Table S4). The measurements from “BOUNDing” are largely consistent with that from  
 606 “SUBTRACTing”, especially when considering the uncertainty of the latter which ranges from  
 607 0.10 m to 0.16 m (Section 5.1). This demonstrates the feasibility and correct implementation  
 608 of the proposed approaches. Interestingly, both of these results offset the MOLA ones by up  
 609 to 1 m. However, it should be noted the overlying layers over the ice blocks due to direct con-  
 610 densation have not been considered in the “SUBTRACTing” and “BOUNDing” models. These  
 611 thickness measurements thus represent the sole contribution by the snowfalls. Estimation of

612 these effects and the correspondent correction of the “BOUNDing” thickness constraints in MY31  
 613 are discussed and described in Section 5.4.

614 **5 Discussion**

615 **5.1 Long-term stability of the ice block heights and precision of the “SUB-**  
 616 **TRACTing” thickness measurements**

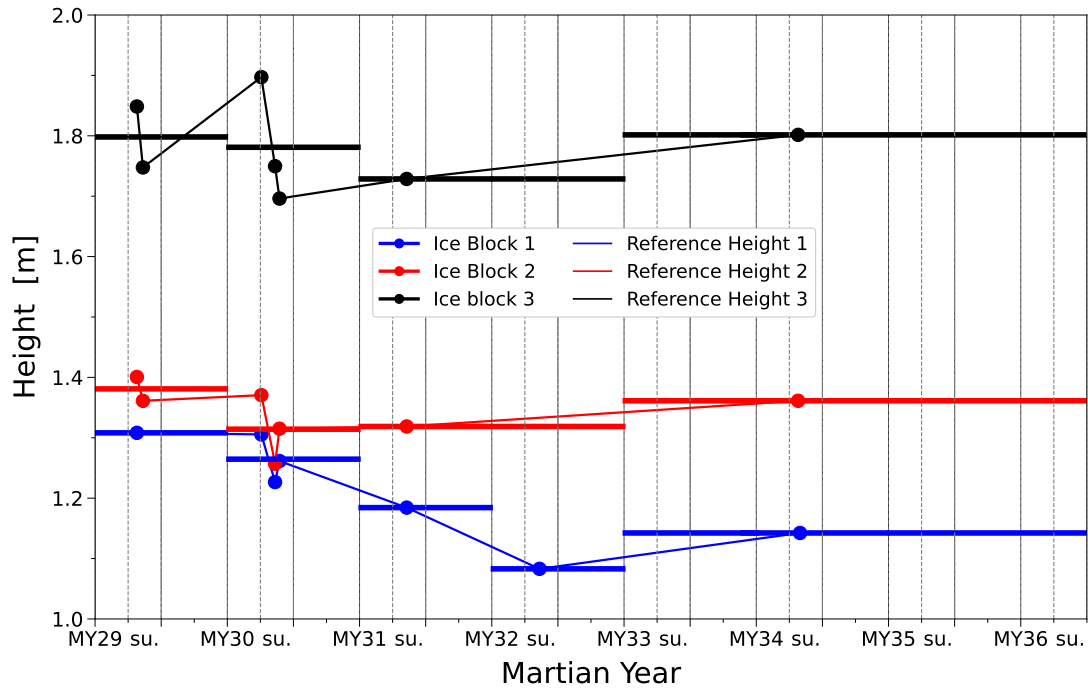


Figure 11: Ice block heights (dots) measured at summertime when free of snow/ice cover and the resultant reference heights (horizontal lines), the latter of which are used for the calculation of the CO<sub>2</sub> snow/ice thickness in the springtime. Note that there exists no height measurements in MY33, MY35, and MY36 due to the lack of image coverage, and the measurement at the adjacent MY34 is used instead as the reference height. Temporal separation between contiguous ticks in the horizontal axis is 90° in solar longitude, that is, a Martian season. su. is the abbreviation for summer.

617 Here, we discuss the stability of the heights of Ice Blocks 1, 2, and 3 which are used as  
 618 reference when computing the snow/ice thickness during the springtime. We also discuss the  
 619 precision of the resultant thickness measurements from the “SUBTRACTing” method.

620 Ice block heights measured when the CO<sub>2</sub> snow/ice cover completely sublimated in var-  
 621 ious summers are shown as dots in Figure 11. Summer images used are marked in bold in Ta-  
 622 bles S1, S2, and S3 for Ice Blocks 1, 2, and 3, respectively. When multiple ice block height mea-  
 623 surements exist within the same summer, their average is taken as the reference value (hori-

624 zontal lines in Figure 11). The bare heights of Ice Blocks 1, 2, and 3 are generally stable with  
 625 variations within  $\sim 0.1$  m for Ice Blocks 2 and 3 but can be up to 0.2 m for Ice Block 1. It is  
 626 worthy to note that these heights generally exhibit a gentle decline from MY29 to MY33, af-  
 627 ter which an increase in MY34 can be spotted. These long-term decreases in ice blocks heights  
 628 could be due to tumbling under its own gravity or that triggered by external forces. Meanwhile,  
 629 aeolian erosion may also be responsible. To mitigate the effects of quasi-stability, we assign the  
 630 heights measured at temporally adjacent summers as the baseline for inverting for thickness of  
 631 the seasonal deposits during the spring (Figure 11). While it is reasonable to speculate their  
 632 decreases in heights due to wind erosion and disintegration of the upper parts due to conden-  
 633 sation/sublimation of the seasonal ice cover, we hardly find any physical explanations for their  
 634 growth. Thus, we attribute these abnormal height increases to potential errors in the reference  
 635 measurements. The induced systematic biases in the thickness values obtained in the spring-  
 636 time for Ice Blocks 1, 2, and 3 are then 0.06 m, 0.05 m, and 0.07 m, respectively.

637 To look into the random errors that can also deteriorate the precision of our thickness mea-  
 638 surements, we combine two types of observables. If there are two or more height measurements  
 639 during each Martian summer, the inconsistencies between measurement pairs are used as a rea-  
 640 sonable gauge of the random errors. Additionally, we examine the repeatability between thick-  
 641 ness measurement pairs in the springtime if their temporal separations are within an empiri-  
 642 cal threshold of  $5^\circ$  in solar longitude. In this case, seasonal snow/ice sublimation within these  
 643 relatively short timespans can be neglected and the aforementioned deviations from zero can  
 644 gain us insights into the precision of our measurements. The standard deviation is calculated  
 645 as follows:

$$646 \quad \sigma_H = \sqrt{\frac{1}{n-1} \sum_{i=1}^n \left( \frac{\Delta H_i}{2} \right)^2}, \quad (14)$$

647 where  $\Delta H_i$  represents the  $i^{\text{th}}$  qualified height discrepancy, out of a total of  $n$ , to be evaluated.  
 648 We scale the random error  $\sigma_H$  by a factor of three for the metric to be robust. For Ice Block 1,  
 649 there are three qualified values during the summers and seven values during the springs. The  
 650 random error of Ice Block 1 is 0.09 m. For Ice Block 2, there are five qualified height discrep-  
 651 ancies during the summers and nine values during the springs, respectively. And, the random  
 652 error of Ice Block 2 is calculated at 0.09 m, which is the same as that of Ice Block 1. Meanwhile,  
 653 for Ice Block 3, five qualified values are available during the summertime and nine during the  
 654 springtime. The random error of Ice Block 3 stands at 0.15 m.

655 We proceed to calculate the Mean Square Error (MSE) that takes into consideration of  
 656 both the systematic bias expressed as  $\varepsilon_H$  and random error, expressed as  $3\sigma_H$ , at each of the  
 657 three locations. These quantities are related as

$$658 \quad \text{MSE}(\hat{T}) = \mathbb{E} \left[ (\hat{T} - T)^2 \right] = \text{Var}(\hat{T}) + \text{Bias}^2(\hat{T}) = 9\sigma_H^2 + \varepsilon_H^2, \quad (15)$$

659 where  $T$  denotes the thickness measurement during springtime. The square roots of the MSE  
 660 errors for thickness measurements for Ice Blocks 1, 2, and 3 are 0.11 m, 0.10 m, and 0.16 m,

661 respectively. The uncertainty of our thickness measurements from ice blocks can thus be  $\sim 0.1$  m  
 662 at the best scenarios, which is on similar level with the statement from [Mount & Titus \(2015\)](#).  
 663 These empirical uncertainties represent the cumulative impacts of a combination of factors such  
 664 as variations in image quality and solar condition, uncertainties in HiRISE DEMs, image or-  
 665 thorectification errors, and shadow length measurement errors.

666 Although these precision statistics do not allow unambiguous confirmation of possible sea-  
 667 sonal thickness variations over multiple years (up to  $\sim 0.2$  m), they do validate the notion that  
 668 no significant thickness variations exist in middle-to-late springs from MY29 to MY36. In ad-  
 669 dition, it strengthens the statement that our thickness measurements are much lower than pre-  
 670 vious MOLA results. This statement is independently verified using the “BOUNDing” approach  
 671 as shown in Section 4.3.

## 672 5.2 Characteristics of the “BOUNDing” approach and its automation

673 Compared to “SUBTRACTing”, the “BOUNDing” approach avoids the need to clearly iden-  
 674 tify and accurately measure the shadow length of the ice blocks during late winter and spring.  
 675 Instead, one only needs to check if there exist cast shadows around the ice blocks to decide whether  
 676 they have been completely covered or not. That is a delightful advantage over the “SUBTRACT-  
 677 ing” approach, especially during late winter or early spring when the shadow boundaries of the  
 678 ice blocks can be unidentifiable due to low solar elevation and thick seasonal layer. This ad-  
 679 vantage means that images obtained during wintertime and springtime are not necessarily re-  
 680 quired to be bundled adjusted and orthorectified, which can greatly boost computation efficiency.  
 681 In fact, bundle adjustment can fail with images acquired in late winter or early spring which  
 682 cannot be utilized in the “SUBTRACTing” approach. For these aforementioned reasons, the  
 683 “BOUNDing” approach can temporally extend to cover late winter and early spring. Unfortu-  
 684 nately, “BOUNDing” can be difficult to implement during late spring as the snow/ice depth shrinks  
 685 to a low level. In such case, the bounding ice blocks along with their shadows required to place  
 686 the lower and upper limits become too small to be resolved in the HiRISE images. In addition,  
 687 the strength of the constraints that can be placed by the “BOUNDing” approach depends on  
 688 the height gap between the bounding ice blocks. For scarps with good concentration of ice blocks,  
 689 the precision of the obtained thickness constraints would be satisfying. Further improvement  
 690 can be expected by spatial averaging of the thickness bounds over a large area. However, “BOUND-  
 691 ing” can fail in regions where number of ice blocks are limited or the distribution of the ice block  
 692 heights does not overlap with the seasonal snow/ice thickness to be constrained, for example,  
 693 in fields where only debris and extremely small ice blocks remain. Despite various merits of “BOUND-  
 694 ing” over “SUBTRACTing”, these two approaches can be complementary to each other. For tem-  
 695 poral extension to late winter and early spring, and spatial extension to a large set of ice block  
 696 clusterings at individual scarps, automatic version of “BOUNDing” would be the choice. How-  
 697 ever, in case high spatial resolution is required within regions of interest, for example, over spe-

698 cific surface features, or when available ice blocks are scarce, “SUBTRACTing” should be ap-  
 699 plied instead. Meanwhile, in a situation when both approaches can work, their results at mid-  
 700 to-late springtime can be used for cross-validation purposes.

701 We would like to stress that “BOUNDing” can actually be applied to all good-quality im-  
 702 ages acquired from MY29 on and form thickness evolution time series in multiple years (Sec-  
 703 tion 4.3). Unfortunately, that would require a tremendous amount of efforts to manually iden-  
 704 tify the proper bounding ice blocks and measure their shadows in the summer images. As such,  
 705 we plan to build on previously-developed automatic software for this purpose, by combining  
 706 computer vision for delineating the shape of the ice blocks (Fanara et al., 2020a,b) with Con-  
 707 volutional Neural Networks for identifying newly-placed ice blocks (Su, Fanara, Xiao, et al., 2023).  
 708 In order to infer their corresponding heights, extracted horizontal boundary of the ice blocks  
 709 can be fitted using ellipsoids, triangular prisms, circular cones, or pyramids according to the  
 710 delineated shape of the shadows. These software programs are established and well maintained  
 711 in Institute of Geodesy and Geoinformation Science, Technische Universität Berlin. Existing  
 712 tools that automatically locate and measure boulders on Mars (for example, Golombek et al.,  
 713 2008; Nagle-McNaughton et al., 2020; Hood et al., 2022), will be adapted for detecting ice blocks  
 714 and used for cross-validation purposes. The main idea is to automatically identify the ice blocks,  
 715 exclude newly-formed ice blocks, and determine the corrected ratio of the ice blocks that have  
 716 not been completely submerged during late winter and spring as compared to that in the sum-  
 717 mer. Meanwhile, the approximated sizes of the ice blocks, including approximated vertical di-  
 718 mension, during the summertime should be automatically determined. Then, we can statisti-  
 719 cally relate the detected ratio to the thickness of the seasonal ice layer according to probabil-  
 720 ity distribution of the ice block heights:

$$721 \quad \int_{T_{\Upsilon}}^{H_{\max}} p(H) dH = \Delta, \quad s.t. \quad \int_0^{H_{\max}} p(H) dH = 1, \quad (16)$$

722 where  $T_{\Upsilon}$  is the thickness of the seasonal layer at  $L_s = \Upsilon^{\circ}$  corresponding to the acquisition  
 723 time of a specific HiRISE image,  $H_{\max}$  is the maximum height of the ice blocks within an ex-  
 724 amined region, and  $p(H)$  is the normalized probability density of the ice block heights. Mean-  
 725 while,  $\Delta$  is the software-determined quantity ratio of ice blocks that have not been fully sub-  
 726 merged at  $L_s = \Upsilon^{\circ}$ . It should be noted that Equation 16 should be in its discretized form as  
 727 the number of ice blocks within an interest region does not reach infinity. The expected advan-  
 728 tage of this automatic approach, tentatively termed automatic “BOUNDing”, is the capability  
 729 to be efficiently applied to entire set of active scarps across the North Pole (refer to Section 5.7  
 730 for locations) and to monitor the depth evolution in real time once a HiRISE image beams back  
 731 to Earth. An additional merit would be that it can completely avoid the cumbersome proce-  
 732 dure of measuring dimensions of the shadows, as required in “SUBTRACTing” and “BOUND-  
 733 ing”.

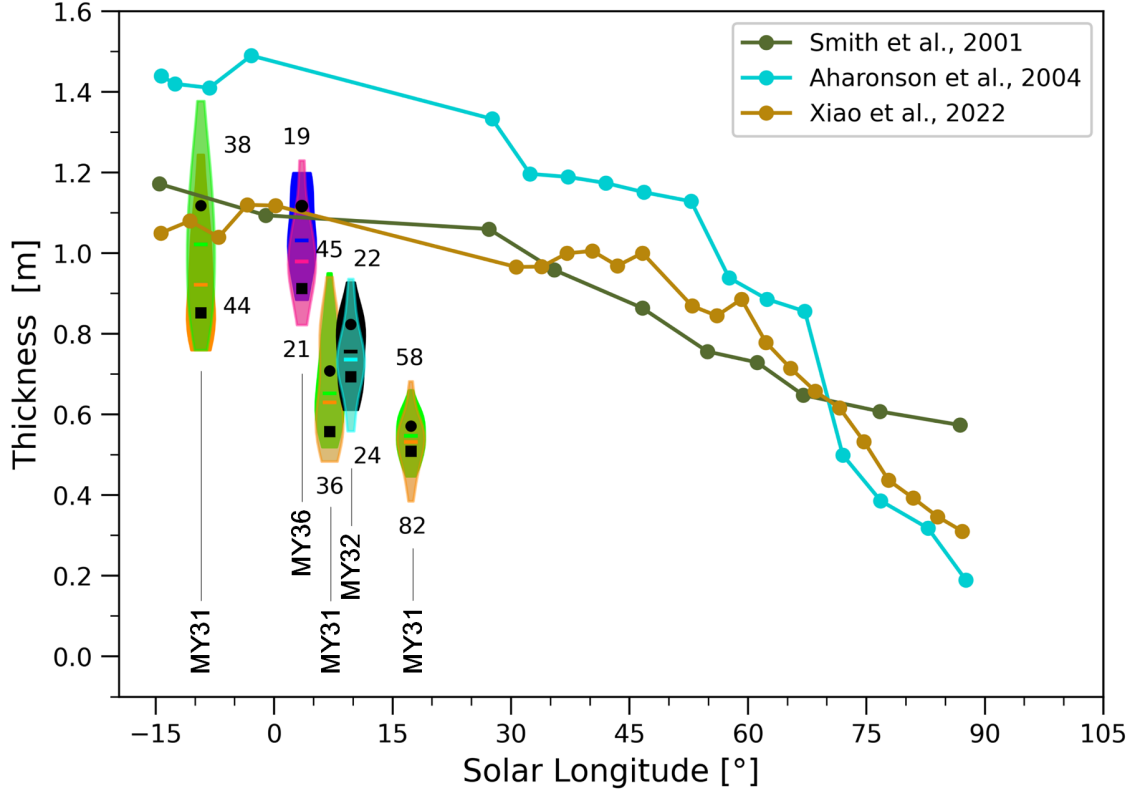


Figure 12: Comparison of thickness results in early springs of MY31 (same as in Figure 10), MY32, and MY36 from the “BOUNding” approach. The bounding limits have been corrected for the offset of  $-\xi_{\gamma}$ . The results are represented by the violin plots with medians of the upper and lower limits shown as horizontal lines. The corresponding number of bounding ice blocks adopted are marked alongside the violin plots. Black squares and dots denote adjusted bounds in consideration of the standard errors of the median constraints (Equation 13). For simplicity and temporal continuity, the constraints obtained at  $L_s = 350.7^\circ$  in late winter of MY31 are plotted at  $L_s = -9.3^\circ$ . Existing MOLA results are shown for reference.

### 734 **5.3 Interannual snowfall variations from “BOUNDing”**

735 Due to high precision of the “BOUNDing” method over scarp-scale area, we proceed to  
 736 apply it to examine possible interannual thickness variations in the very early spring (before  
 737  $L_s = 10^\circ$ ) when the seasonal layer is among the thickest. After excluding images with bad qual-  
 738 ity, only ESP\_024232\_2650\_RED acquired at  $L_s = 7.0^\circ$  in MY31, ESP\_033120\_2650\_RED at  $L_s =$   
 739  $9.7^\circ$  in MY32, and ESP\_068224\_2650\_RED at  $L_s = 3.5^\circ$  in MY36 are available. For MY31 and  
 740 MY32, the same summer reference image is used (ESP\_027674\_2650\_RED) and the corrections  
 741 of  $-\xi_\gamma = -0.20$  m and  $-\xi_\gamma = -0.22$  m are respectively applied to the overestimated thick-  
 742 ness values. For MY36, the summer image acquired in MY34 is used (ESP\_053730\_2650\_RED)  
 743 and a correction of  $-\xi_\gamma = -0.08$  m is adopted. Bounding ice blocks are selected over the en-  
 744 tire Scarp 1. The corrected results and their comparison are shown in Figure 12. The results  
 745 at  $L_s = 350.7^\circ$  and  $L_s = 17.3^\circ$  in MY31 are also shown alongside that at  $L_s = 7.0^\circ$  in MY31  
 746 to illustrate the general depth evolution trend during the beginning of spring (same as in Fig-  
 747 ure 10). The median depth bound at  $L_s = 9.7^\circ$  in MY32 is from 0.74 m to 0.76 m. Meanwhile,  
 748 the median depth bound at  $L_s = 3.5^\circ$  in MY36 ranges from 0.98 m to 1.03 m, which is  $\sim 0.36$  m  
 749 larger than between 0.63 m and 0.65 m at  $L_s = 7.0^\circ$  in MY31. Considering the adjusted bounds  
 750 at the examined solar longitudes in MY31 and MY36 (black squares and dots in Figure 12),  
 751 the interannual variation of  $\sim 0.36$  m can be deemed credible. Indeed, treating the thickness  
 752 bounds at MY31 and MY36 as being independent, the propagated uncertainty associated with  
 753 the MY31 to MY36 thickness variation is 0.13 m. A supporting evidence is that there exist plenty  
 754 of ice blocks that are visually detectable at  $L_s = 7.0^\circ$  in MY31 can stay completely covered  
 755 at  $L_s = 3.5^\circ$  in MY36. We can also see in the plot that all of the examined thickness values  
 756 are lower than the existing MOLA results, by a magnitude of 0.1 m to 1 m. However, we note  
 757 again that the effects of crowning layers on top of the ice blocks due to direct condensation have  
 758 not been considered in the applied “BOUNDing” model. As such, the detected multiyear thick-  
 759 ness variation refers to that solely induced by the snowfalls (Section 5.4). This is the first time  
 760 that an interannual variation in the amount of Martian snowfalls is detected, stressing the im-  
 761 portance of carrying out long-term monitoring of the Martian volatile and dust cycles.

### 762 **5.4 Crown depth estimation and correction in MY31**

763 In the presented geometric models (Figures 1, 2 and 3), we have not attempted to cor-  
 764 rect for the effects of moating and crowning. For rocks, moats form in the fall while they are  
 765 still warm with stored heat energy from summertime solar insolation (Mount & Titus, 2015).  
 766 Snow/ice falling around the warm rocks will sublime, leaving a void. Moating has been exten-  
 767 sively observed around the rocks in the dune fields (Mount & Titus, 2015), which can be at-  
 768 tributed to the large contrast in thermal inertia of rocks (relatively high) and sands (relatively  
 769 low). The ice blocks fallen from the NPLDs, as investigated in our case, are made mainly of  
 770 water ice, which feature very high thermal inertia. However, the upper layer of the Basal Unit

771 deposits where the ice blocks reside is presumably composed of previously fallen ice blocks, lead-  
 772 ing to its sloped surface at the foot of the NPLDs. Evidence has it that the potentially active  
 773 scarps generally feature a higher overall slope from Basal Unit outcrop top to bottom than the  
 774 potentially quiescent ones (Russell et al., 2010). As a result, the contrast in thermal inertia be-  
 775 tween the ice blocks and the underlying Basal Unit top layer should be limited. Thus, exten-  
 776 sive moating well into the springtime should be unlikely. Indeed, we have not observed any in-  
 777 stance of moating around the ice blocks during springtime with typical examples shown in Fig-  
 778 ures 6, 8, and 9. The formation of a topping ice layer, that is, crowning, has been properly ac-  
 779 counted for when using shadowing of the rocks to invert for thickness evolution of the seasonal  
 780 snow/ice deposits (Mount & Titus, 2015). For rocks, crowns form in the winter, after they have  
 781 lost sufficient heat and are expected to be most prevalent in early to mid-spring. If crowns form  
 782 then the measured shadow length will be longer than in the case without, making the uncor-  
 783 rected rock height larger and thus reducing the calculated snow/ice thickness. For ice blocks,  
 784 the crowning can also happen and should be properly accounted for. Indeed, we have observed  
 785 systematic widening of the ice block walls in the HiRISE images which is due to direct conden-  
 786 sation of CO<sub>2</sub> as frosts (Figure 13).

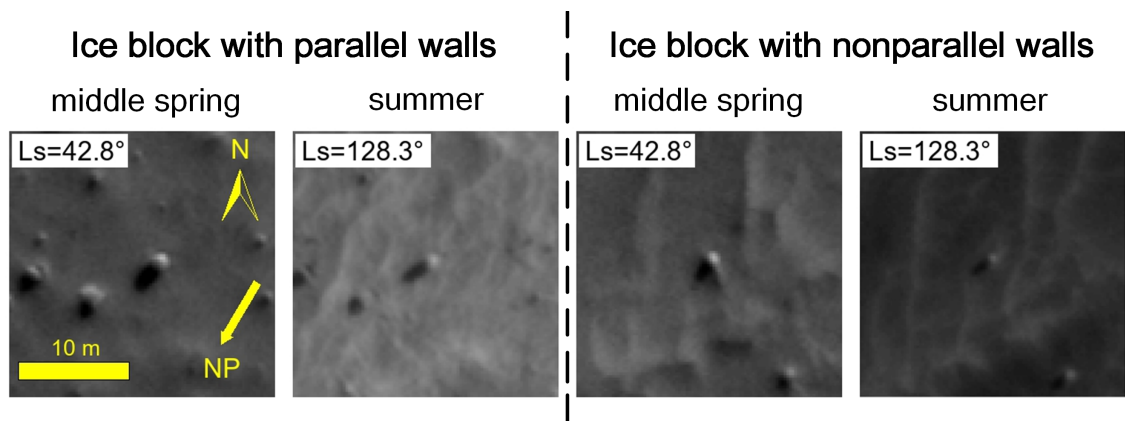


Figure 13: Images of example ice blocks (centered at the sub-frames) used to deduce depth of topping crowns. Acquisition time stamps of the images are  $L_s = 42.8^\circ$  in middle spring and  $L_s = 128.3^\circ$  in summer in MY31, respectively. The images used are ESP\_025221\_2650\_RED and ESP\_027674\_2650\_RED, respectively. Left panel shows an ice block with parallel walls and its shadow, the thinning of which from middle spring to summer is obvious. Right panel refers to the change of a cone-shaped ice block. Map projection and scale are as in Figures 6, 8, and 9. Illumination is to the bottom-left corner.

787 Mount & Titus (2015) corrected for the crowning and moating by adding the increases  
 788 in snow/ice depths between consecutive solar longitudes to all prior depths. This forces the ice  
 789 depth to either decrease or remain the same between different solar longitudes, and the corrected  
 790 values serve as minimum bounds to the seasonal snow/ice depth. The representative ice depth

791 curve before correction in their study features significant increases during middle-to-late spring  
 792 (Figure S3 in Mount & Titus (2015)). However, in our case we have not seen significant off-season  
 793 increases (Figures 7, 10, and 12), so the results should not change much after incorporating their  
 794 correction scheme. This indicates that the depths of the crowns over the ice blocks in this study  
 795 likely quasi-linearly decrease to zero right at when the seasonal deposits completely sublime  
 796 back into the atmosphere. To conclude, the correction scheme described in Mount & Titus (2015)  
 797 can be inapplicable in our case. We thus propose an original way to estimate and correct for  
 798 the effects of the crowning on top of the ice blocks. The proposed correction scheme relies on  
 799 three reasonable assumptions: (1) Atmospheric deposition as snowfalls do not accumulate over  
 800 the top of the selected spiky ice blocks and over steep ice block walls. In fact, it is known that  
 801 aeolian processes can redistribute the carbon dioxide snow crystals into topographic lows, damp-  
 802 ing the topography (Mount & Titus, 2015). Ice blocks shaped like triangular prisms or feature  
 803 lone peaks are used in the demonstration of the “SUBTRACTing” and “BOUNDing” approaches  
 804 (Figures 6, 8, and 9), which makes significant accumulation of snow particles over the ice blocks  
 805 unlikely. Thus, the crowns in our case can be solely composed of directly condensed frosts; (2)  
 806 Frosts through direct condensation are homogeneously distributed around the ice blocks and  
 807 their adjacent surroundings. This hypothesis can be corroborated by the fact that there exist  
 808 limited thermal contrast between the ice blocks and the Basal Unit outcrops where they reside  
 809 on. It is further justified by similar depths of ice block crowns at a specific solar longitude over  
 810 the entire scarp, as illustrated in Figure 14; (3) Negligible moating around the ice blocks, as  
 811 previously demonstrated in this section. These assumptions mean that the contributions of the  
 812 snowfalls and frosts to the thickness of the seasonal ice deposits can be decomposed and esti-  
 813 mated separately. The thickness measurements from “SUBTRACTing” and “BOUNDing” ( $T_{\Upsilon}$   
 814 at  $L_s = \Upsilon^\circ$ ) can be considered as merely contributed by snowfalls (Figures 7, 10, and 12). In-  
 815 deed, if there exists no snowfall, then the shadow length of the ice blocks would remain unchanged  
 816 and thickness measurements from “SUBTRACTing” and “BOUNDing” should all equal zero.  
 817 These assumptions also enable us to use the widening of the ice blocks as a proxy to approx-  
 818 imate the depths of the crowning frost layers over the ice blocks ( $T_{\Upsilon}^c$  at  $L_s = \Upsilon^\circ$ ). The total  
 819 thickness of the seasonal layer then can be calculated as the sum of  $T_{\Upsilon}$  and  $T_{\Upsilon}^c$ .

820 To approximate the depths of the crowns, we first examine the widening of cylinder-shaped  
 821 ice blocks with parallel walls, mostly vertical walls, during late winter and spring as compared  
 822 to their dimensions during the summertime when the enveloping seasonal CO<sub>2</sub> frost layer com-  
 823 pletely sublimates away. A typical example of these particular ice blocks is shown in Figure 13.  
 824 Within the portion of the shadow with parallel bounding lines, the width of the shadow, and  
 825 hence that of the ice block itself, can be directly measured along any transverse line running  
 826 perpendicular to the solar illumination. Then, the crown depth at  $L_s = \Upsilon^\circ$  can be approxi-  
 827 mated by

$$828 \quad \hat{T}_{\Upsilon}^c = \frac{W_{\Upsilon}^1 - W^2}{2}, \quad (17)$$

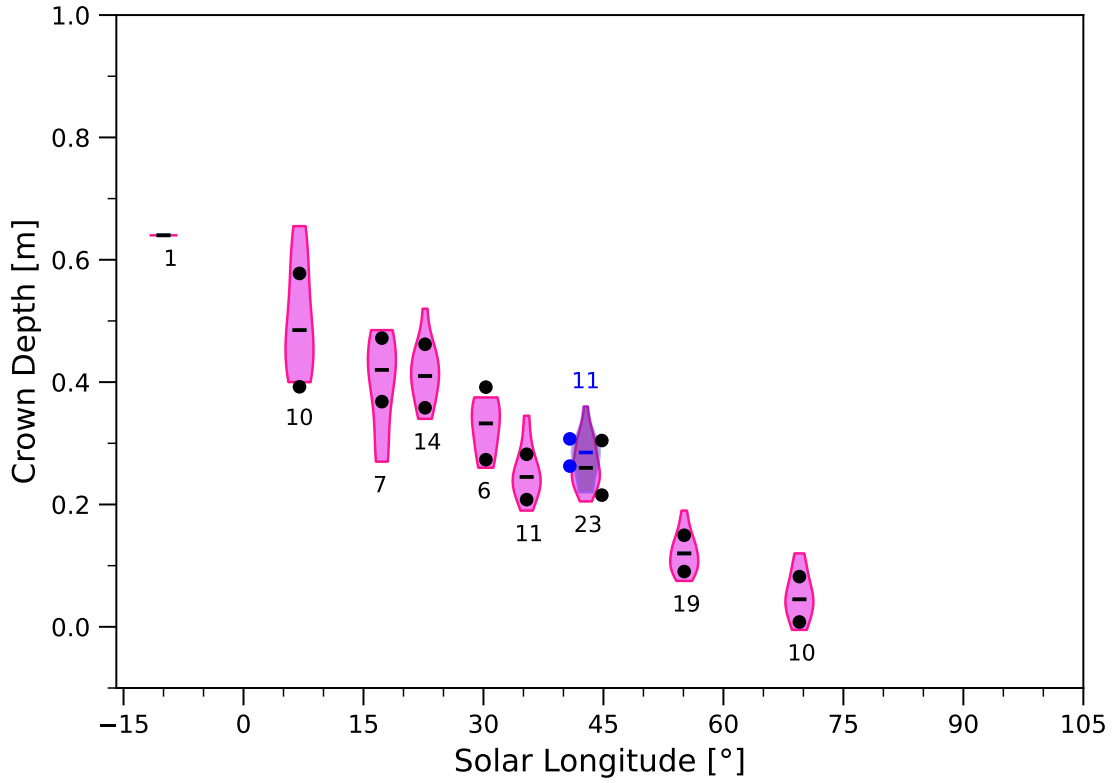


Figure 14: Depth estimates of the crowns from direct condensation over Scarp 1 in MY31, as represented by the violin plots with medians shown as horizontal lines. The corresponding number of independent measurements are marked alongside the violin plots. Pink violins represent measurements using ice blocks with parallel walls and the blue one at  $L_s = 42.8^\circ$  refers to that from ice blocks with nonparallel walls. Black and blue dots denote derived bounding intervals by taking into account of the standard errors of the medians. For simplicity and temporal continuity, the single constraint obtained at  $L_s = 350.7^\circ$  in late winter is plotted at  $L_s = -9.3^\circ$ .

829 where  $W_{\Upsilon}^1$  is the width of the shadow of the ice block during late winter or spring, and  $W^2$  de-  
 830 notes that of the same ice block during summertime. Temporal evolution of the crown depth  
 831 over the late winter and spring in MY31 is illustrated in Figure 14. The abstract probability  
 832 distribution of crown depth measurements at a specific solar longitude is approximated using  
 833 Equation 11 and represented using a pink violin. At  $L_s = 42.8^\circ$ , the image features the best  
 834 sharpness and the most measurements are made (a total of 23), with a median value of 0.26 m.  
 835 In contrast, at  $L_s = 350.7^\circ$  in late winter the image is the most severely blurred and only one  
 836 valid measurement is obtained with a value of 0.64 m. For early spring images acquired at  $L_s =$   
 837  $7.0^\circ$  and  $L_s = 17.3^\circ$ , the dispersions of the measurements are relatively large due to degraded  
 838 quality associated with still low solar elevation angles. As can be seen in the plot, the crown  
 839 depth quasi-linearly decreases from 0.64 m at  $L_s = 350.7^\circ$  in late winter, 0.26 m at  $L_s = 42.8^\circ$   
 840 in middle spring, to 0.045 m at  $L_s = 69.5^\circ$  in late spring. The approximately quasi-linearly  
 841 declining trend corroborates our previous conjecture in the light of limited middle-to-late spring  
 842 thickness increases present in our uncorrected results. Like it has been done in Equation 13,  
 843 we derive adjusted bounding intervals for the most likely crown depths at  $L_s = \Upsilon^\circ$  by taking  
 844 the standard errors of the medians into account:

$$845 \quad \Theta_{\Upsilon}^c = \left[ \text{Md}_{\Upsilon}^c - \frac{3 \times \text{SMAD}_{\Upsilon}^c}{\sqrt{N_{\Upsilon}^c}}, \text{Md}_{\Upsilon}^c + \frac{3 \times \text{SMAD}_{\Upsilon}^c}{\sqrt{N_{\Upsilon}^c}} \right], \quad (18)$$

846 which are marked as black dots in Figure 14. The half ranges of these bounding intervals are  
 847 from 0.02 m at  $L_s = 55.1^\circ$  to 0.09 m at  $L_s = 7.0^\circ$ , with typical values on the order of 0.05 m  
 848 (Table S4). The limited dispersions in crown depths, or ice block widening, over the entire scarp  
 849 at individual solar longitudes can to some extent reflect the spatial uniformity of the directly  
 850 condensed layer in the vertical dimension. This serves as an additional line of evidence to jus-  
 851 tify our second assumption that the directly condensed frost layer is of the same thickness over  
 852 the ice blocks and their adjacent surroundings. The estimated 0.64 m deep frost layer due to  
 853 direct condensation in late winter is significantly shallower than the snow layer with a thick-  
 854 ness of  $0.97 \pm 0.13$  m (Section 4.3). In terms of thickness and volume, the snowfalls can make  
 855 up 60.2% of the seasonal deposits in late winter. However, assuming the crowns to be slab ice  
 856 that features a density greater than or equal to  $1,190 \text{ kg/m}^3$  ( $\leq 26\%$  porosity,  $\geq 8,000 \mu\text{m}$  grains)  
 857 and the snow to feature a density of less than or equal to  $420 \text{ kg/m}^3$  ( $\geq 74\%$  porosity,  $\leq 1,000 \mu\text{m}$   
 858 grains) (Mount & Titus, 2015), then snowfalls should account for less than 34.9% of the sea-  
 859 sonal deposits in terms of mass during late winter.

860 As majority of the ice blocks used in the demonstration of the ‘‘SUBTRACTing’’ and ‘‘BOUND-  
 861 ing’’ methods are peaked or triangular-prism-shaped, we wonder if similar amount of frosts is  
 862 directly condensed onto these nonparallel walls. Thus, we also look into the widening of the cone-  
 863 shaped ice blocks. The schematic of the geometry with shadow width measuring points marked  
 864 is illustrated in Figure 15. As the boundaries of the shadows of these peaked ice blocks are triangular-  
 865 shaped, shadow width measurements have to be made at properly adjusted positions so that  
 866 they can be directly compared to reveal the widening. From Equation 6, the relation between

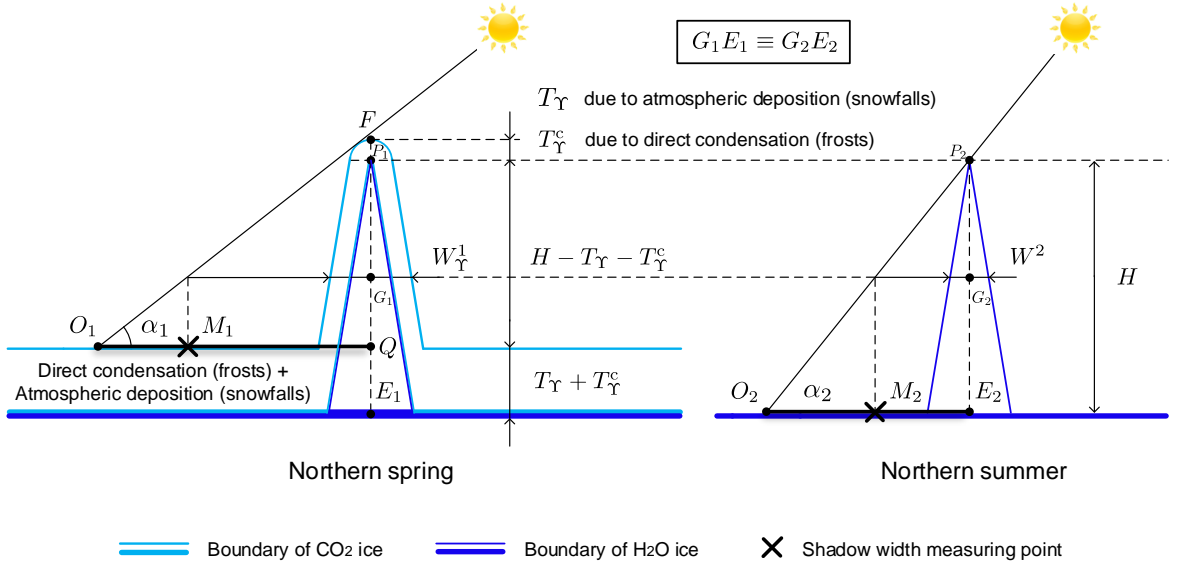


Figure 15: Schematic showing how to measure the width widening of a cone-shaped ice block at  $L_s = \Upsilon^\circ$ . In spring, the ice block and its surrounding surface are covered with a layer of  $\text{CO}_2$  deposits, with a thickness of  $T_\Upsilon^c$  over the former and  $T_\Upsilon + T_\Upsilon^c$  over the latter. The variable  $T_\Upsilon$  denotes the thickness of the seasonal deposits accumulated by snowfalls, and  $T_\Upsilon^c$  the contribution from direct condensation as frosts. During summertime, the seasonal deposits have completely sublimated back into the atmosphere and allows the bare height of the ice block ( $H$ ) to be estimated. Slope and aspect of the local terrain are neglected. Locations of the shadow width measurements to be compared are marked by black crosses which ensure  $G_1E_1 \equiv G_2E_2$ . Note that directly condensed and  $\text{CO}_2$ -snowfall-scavenged water ice particles within the seasonal deposits are not marked.

867 the height of the ice block ( $H$ ) and the measured shadow length ( $L_S$ ) in the summer image can  
 868 be written as follows:

$$869 \quad H = L_S \times (\cos \omega \sin \beta + \tan \alpha \cos \beta). \quad (19)$$

870 To simplify the model, we only use ice blocks situated over gentle slopes of less than  $5^\circ$ . Ne-  
 871 glecting the slope in Equation 19, that is  $\beta = 0$ , then it reduces to be

$$872 \quad H = O_2E_2 \times \tan \alpha_2, \quad (20)$$

873 where  $O_2E_2$  is the shadow length of the ice block when it is free of seasonal  $\text{CO}_2$  snow/ice in  
 874 the summertime (Figure 15). We now define  $\delta_1$  and  $\delta_2$  as the ratios of the distances from the  
 875 shadow top to the width measuring point along the solar illumination to the full shadow length  
 876 at spring and summer images, respectively. From the geometry of the ice block and the over-  
 877 lying seasonal layer, these two ratios can be defined as follows:

$$878 \quad \begin{cases} \delta_1 = \frac{O_1M_1}{O_1Q} = \frac{G_1Q}{FQ} = \frac{G_1Q}{H - T_\Upsilon} \\ \delta_2 = \frac{O_2M_2}{O_2E_2} = \frac{G_2E_2}{P_2E_2} = \frac{G_2E_2}{H} \end{cases}. \quad (21)$$

879 where  $T_\Upsilon$  is the average depth of the seasonal layer at Scarp 1 from the ‘‘BOUNDing’’ approach  
 880 at  $L_s = \Upsilon^\circ$  (Figure 10). What we need to do is determine  $\delta_2$  given a known  $\delta_1$ , satisfying  $G_1E_1 \equiv$   
 881  $G_2E_2$ . From the definition of  $\delta_1$ , we know

$$882 \quad G_1Q = (H - T_\Upsilon) \times \delta_1. \quad (22)$$

883 Then  $P_1G_1$  can be related to  $G_1Q$  as

$$884 \quad P_1G_1 = H - T_\Upsilon - \check{T}_\Upsilon^c - G_1Q = H - T_\Upsilon - \check{T}_\Upsilon^c - (H - T_\Upsilon) \times \delta_1, \quad (23)$$

885 where  $\check{T}_\Upsilon^c$  is the a priori crown depth and we set it to be the median value of the measurements  
 886 from inspecting the ice blocks with parallel walls (black horizontal lines in Figure 14):

$$887 \quad \check{T}_\Upsilon^c = T_\Upsilon^c. \quad (24)$$

888 The ratio  $\delta_2$  can be calculated by relating to  $P_1G_1$  and the ratio  $\delta_1$  as

$$889 \quad \delta_2 = \frac{H - P_2G_2}{H} = \frac{H - P_1G_1}{H} = \frac{T_\Upsilon + \check{T}_\Upsilon^c + (H - T_\Upsilon) \times \delta_1}{H}. \quad (25)$$

890 Taking the extreme of  $\delta_1 = 0$ , then  $\delta_2 = \frac{T_\Upsilon + \check{T}_\Upsilon^c}{H}$ . Adopting another extreme of  $\delta_1 = 1$ ,  
 891 then  $\delta_2 = \frac{H + \check{T}_\Upsilon^c}{H} > 1$  which is reasonable as the width in the summer image cannot be mea-  
 892 sured. Finally, widths are measured along the traverse lines crossing the shadow measuring points  
 893 and running perpendicular to the sunlight in the spring ( $W_\Upsilon^1$ ) and summer images ( $W^2$ ), re-  
 894 spectively. The depth of the crown over the ice block can be approximated again by utilizing  
 895 Equation 17. If  $\hat{T}_\Upsilon^c - \check{T}_\Upsilon^c \leq 0.1$  m, then their average is taken as the measured crown depth  
 896 over the ice block in question, that is  $\hat{T}_\Upsilon^c \leftarrow \frac{\hat{T}_\Upsilon^c + \check{T}_\Upsilon^c}{2}$ . Else, the a priori crown depth is up-  
 897 dated  $\check{T}_\Upsilon^c \leftarrow \hat{T}_\Upsilon^c$  and the iteration is started again to make sure the difference between the a

898 priori value and posterior estimate reduces to within 0.1 m. This approach using the cone-shaped  
 899 ice blocks pre-requires clear identification of the triangular-shaped shadow boundary and thus  
 900 permits much less valid estimates than those using the ice blocks with parallel walls. In fact,  
 901 it is inapplicable to images acquired in late winter and early spring. Here, we only apply this  
 902 approach to the image acquired at  $L_s = 42.8^\circ$  which features the best quality in MY31. We  
 903 obtain a total of 11 valid measurements that range from 0.22 m to 0.36 m, with a median of  
 904 0.29 m (blue violin in Figure 14). One of these measurements reaches convergence after two it-  
 905 erations while all the rest satisfy the stopping criterion after just one iteration. These measure-  
 906 ments overlap well with those obtained using ice blocks with parallel walls with a median of  
 907 0.26 m. Meanwhile, the bounding interval in light of the standard error of the median constraint  
 908 is highly consistent with that from the ice blocks with parallel walls (blue and black dots in Fig-  
 909 ure 14, respectively). That means the steepness of the ice block walls does not significantly in-  
 910 fluence the depth of the directly condensed frosts. This conclusion also corroborates our sec-  
 911 ond assumption that the thickness of the directly condensed frosts is the same over the ice block  
 912 walls and top, which permits us to use the widening of the ice blocks as a proxy to approximate  
 913 the depths of the overlying crowns.

914 Eventually, we correct the snowfall thickness measurements from “BOUNDing” in MY31  
 915 for these direct condensation effects (Figure 16). The total thickness of the seasonal deposits  
 916 at  $L_s = \Upsilon^\circ$  is calculated as follows:

$$917 \quad T_{\Upsilon}^{\text{sum}} = T_{\Upsilon} + \hat{T}_{\Upsilon}^c = \frac{\bar{\Theta}_{\Upsilon}^T + \bar{\Theta}_{\Upsilon}^c}{2}, \quad (26)$$

918 with its bounding interval set by treating the snowfall thickness estimates and the crown depths  
 919 as two independent variables:

$$920 \quad \Theta_{\Upsilon}^{\text{sum}} = \left[ T_{\Upsilon}^{\text{sum}} - \frac{\sqrt{\Delta\Theta_{\Upsilon}^T{}^2 + \Delta\Theta_{\Upsilon}^c{}^2}}{2}, T_{\Upsilon}^{\text{sum}} + \frac{\sqrt{\Delta\Theta_{\Upsilon}^T{}^2 + \Delta\Theta_{\Upsilon}^c{}^2}}{2} \right], \quad (27)$$

921 where  $\bar{\Theta}_{\Upsilon}^T$  and  $\Delta\Theta_{\Upsilon}^T$  denote the average and range of the bounding interval for the snowfall thick-  
 922 nesses from the “BOUNDing” approach (Equation 13 and Figure 10), respectively. Meanwhile,  
 923  $\bar{\Theta}_{\Upsilon}^c$  and  $\Delta\Theta_{\Upsilon}^c$  are the average and range of the crown depth bounding interval by examining  
 924 the ice blocks with parallel walls (Equation 18 and Figure 14), respectively. For  $L_s = 350.7^\circ$   
 925 in late winter, there exists no bound interval for the crown depth as there is only one valid es-  
 926 timate. We then tentatively set its interval range to be two times that at the proximate  $L_s =$   
 927  $7.0^\circ$ . The bounding intervals from Equation 27 are shown as error bars in Figure 16. The cor-  
 928 rected thickness stands at 1.63 m with a half interval range of 0.22 m at  $L_s = 350.7^\circ$  in late  
 929 winter, 0.45 m with a half interval range of 0.06 m at  $L_s = 42.8^\circ$  in middle spring, and decreases  
 930 to 0.06 m with a half interval range of 0.05 m at  $L_s = 69.6^\circ$  in late spring. A majority of the  
 931 bounding interval half ranges are less than 0.1 m (Table S4). The offsets between these corrected  
 932 thicknesses and existing MOLA results are thus significantly reduced. At late winter, our thick-  
 933 ness estimate of  $1.63 \pm 0.22$  m is  $\sim 0.5$  m above that of D. E. Smith et al. (2001) and Xiao, Stark,  
 934 Schmidt, Hao, Steinbrügge, et al. (2022). However, it is compatible with that of Aharonson et

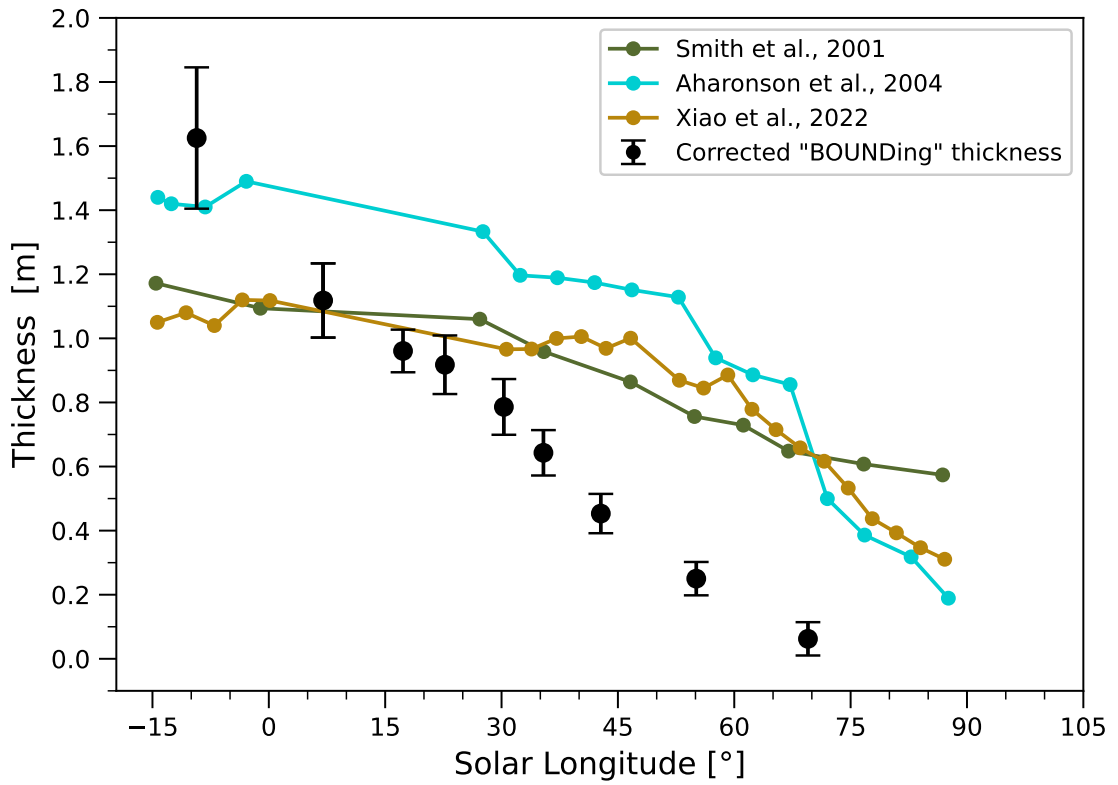


Figure 16: Thickness evolution of the seasonal layer in MY31 from “BOUNDing” after the correction for the crowns over the ice blocks, and their comparison to the existing MOLA results. Uncertainty bars denote the accumulated errors from both the uncorrected thickness measurements and the crown depth estimates. For simplicity and temporal continuity, the constraints obtained at  $L_s = 350.7^\circ$  in late winter of MY31 are plotted at  $L_s = -9.3^\circ$ .

935 al. (2004) considering the associated uncertainty of  $\sim 0.2$  m. Then, the thickness estimates in  
 936 this study quasi-linearly decline towards summer solstice. In comparison, the MOLA results  
 937 decline more gently than ours before  $L_s = \sim 60^\circ$  in late spring. The gap between our results  
 938 and the MOLA ones thus forms at the beginning of spring and enlarges to be up to 0.8 m at late  
 939 spring. These lingering offsets and possible reasons behind are thoroughly discussed in the sub-  
 940 sequent Section 5.5.

941 From late winter to spring, the solar elevation angle increases and so does the solar in-  
 942 solation. If assuming the albedo and average density of the seasonal deposits to be constant through-  
 943 out winter and spring, then the slope of the thickness evolving curve should increase with time.  
 944 The not-so-varying declining rate of our curve as in Figure 16 thus indicates the combined ef-  
 945 fects of density variations, like densification due to gravity-induced self-compaction and re-crystallization  
 946 (Eluszkiewicz et al., 2005; Mount & Titus, 2015; Xiao, Stark, Schmidt, Hao, Steinbrügge, et  
 947 al., 2022), and albedo variations that take place in the seasonal deposits (Pommerol et al., 2013;  
 948 Gary-Bicas et al., 2020). Indeed, we note that thickness evolution of the seasonal deposits at  
 949 the three study sites in Mount & Titus (2015) features distinct trends during the spring: quasi-  
 950 constant thinning rate at Phoenix’s landing site ( $68^\circ\text{N}$ ,  $233^\circ\text{E}$ ); temporally decelerating thin-  
 951 ning rate at a dune field labeled Dunes ( $75^\circ\text{N}$ ,  $282^\circ\text{E}$ ); temporally accelerating thinning rate  
 952 at a crater site called Louth ( $70^\circ\text{N}$ ,  $103^\circ\text{E}$ ).

## 953 5.5 Comparison to previous MOLA results

954 Inconsistencies up to 0.4 m exist between the existing MOLA results (Figures 7 and 10).  
 955 The difference between the curve of Xiao, Stark, Schmidt, Hao, Steinbrügge, et al. (2022) and  
 956 that of Aharonson et al. (2004) could mainly be attributed to different post-correction strate-  
 957 gies utilized to correct for the global temporal bias in the MOLA dataset. This bias has been  
 958 observed at all latitudes, and it features a peak-to-peak amplitude of 2 m and a phase that re-  
 959 sembles the synodic period of Mars (Xiao, Stark, Steinbrügge, et al., 2022). Xiao, Stark, Schmidt,  
 960 Hao, Steinbrügge, et al. (2022) corrected for the bias assuming it to be constant at the North  
 961 Pole and equals that obtained at annulus  $50^\circ\text{N}$ . In contrast, Aharonson et al. (2004) param-  
 962 eterized the systematic biases of the MOLA tracks by 3D overlapping polynomials and inverted  
 963 the coefficients by minimizing height residuals at cross-overs equatorward of  $57^\circ\text{S/N}$  and that  
 964 acquired within 15 Earth days in the North Pole. Essentially, their correction for this global  
 965 temporal bias at the North Pole was extrapolated from the polynomials fitted within  $57^\circ\text{S/N}$ .  
 966 D. E. Smith et al. (2001) differentiated the thickness variation in each polar annulus to that  
 967 acquired at  $60^\circ\text{S/N}$  to correct for the global temporal bias. Their thickness variation is surpris-  
 968 ingly lower compared to the other MOLA results, which may arise from additional smoothing  
 969 they have applied. Unfortunately, Xiao, Stark, Steinbrügge, et al. (2022) confirmed latitude-  
 970 dependence of the global temporal bias in the MOLA heights, and the simple treatment of it  
 971 by assuming it to be constant in the polar regions can introduce temporal bias into the MOLA

972 thickness evolution curves. It is imperative that we pin down the root cause for this global tem-  
973 poral bias and correct the MOLA heights for it at the local scale in the future.

974 After the correction for direct condensation effects, offsets up to  $\sim 0.8$  m in magnitude be-  
975 tween the results using shadowing of the ice blocks and the available MOLA results can still  
976 be observed during the spring of MY31 (Section 5.4). Here we discuss several aspects that could  
977 possibly be responsible for these offsets: (1) Discrepancies in geographical and year-to-year cov-  
978 erage that exist between the results. Result from [D. E. Smith et al. \(2001\)](#) represents the av-  
979 erage pattern at latitudinal annulus  $85.5^\circ\text{N}$ , and that of [Aharonson et al. \(2004\)](#) at latitudinal  
980 annulus  $86^\circ\text{N}$ . Meanwhile, result from [Xiao, Stark, Schmidt, Hao, Steinbrügge, et al. \(2022\)](#) is  
981 representative of thickness evolution at a grid element of size  $0.5^\circ$  in latitude and  $10^\circ$  in lon-  
982 gitude. Furthermore, MOLA results date back to MY24/25 while results in this study are from  
983 MY29 to MY36. Therefore, geographical differences and inter-annual variability might partially  
984 contribute to the offsets; (2) Biases related to the MOLA results. [Wang & Ingersoll \(2002\)](#) made  
985 a map of the north polar regions of Mars using the Mars Global Surveyor (MGS) Mars Orbiter  
986 Camera (MOC) wide-angle swaths at  $L_s = 111^\circ$  right after the summer solstice in MY25. No  
987 apparent seasonal deposits can be observed at that time outside of the NPLDs. Meanwhile, [Piqueux](#)  
988 [et al. \(2015\)](#) carried out continuous tracking of the SNPC edges at multiple Mars Years using  
989 MGS Thermal Emission Spectrometer (TES) and showed that it completely sublimated away  
990 at around  $L_s = 80^\circ$  in late spring of MY25. Thus, the biases are at least  $\sim 0.60$  m ([D. E. Smith](#)  
991 [et al., 2001](#)),  $\sim 0.35$  m ([Aharonson et al., 2004](#)), and  $\sim 0.41$  m ([Xiao, Stark, Schmidt, Hao, Stein-](#)  
992 [brügge, et al., 2022](#)) for these MOLA results, respectively. In fact, various complicated processes  
993 can affect and bias the MOLA results, for example, pulse saturation due to high albedo of the  
994 polar ice, the absence of a variable gain amplifier, and limited recording digital ranges ([Neu-](#)  
995 [mann et al., 2001, 2003](#)), interference of the laser pulses with dynamic and rough surface, in-  
996 complete correction for the global temporal bias, and penetration of the laser pulses into the  
997 translucent and sloped slab ice ([Xiao, Stark, Schmidt, Hao, Steinbrügge, et al., 2022](#)). Unfor-  
998 tunately, each of these listed factors is difficult to model and quantify; (3) Interannual varia-  
999 tions. Possible variations in the quantities of snowfalls and frosts can exist between MY24/25  
1000 (acquisition time of MOLA footprints) and MY31 (for example, Figure 12). However, these mul-  
1001 tiyear variations should generally decrease with time in spring as the seasonal layer thins and  
1002 finally vanishes, which contradicts the observed temporal evolution of the offset. To conclude,  
1003 there exists strong evidence to argue that a large portion of these discrepancies result from bi-  
1004 ases inherited in the MOLA dataset.

## 1005 5.6 Comparison to predicted snowfall quantities

1006 In this section, we discuss our measured snowfall thickness as compared to that predicted  
1007 by a simple  $\text{CO}_2$  cloud settling model using atmospheric profiles acquired by MCS onboard the  
1008 MRO ([Alsaeed & Hayne, 2022](#)). We now know that the snowfall rates are significantly larger

1009 in the north than those in the south, because the former features larger surface air pressure and  
 1010 a thicker water ice polar hood that can serve as condensation nuclei for the CO<sub>2</sub> snowfalls (Gary-  
 1011 Bicas et al., 2020; Alsaeed & Hayne, 2022). Alsaeed & Hayne (2022) concluded that the CO<sub>2</sub>  
 1012 snowfall equivalent thickness accumulated throughout fall and winter is on the order of several  
 1013 millimeters poleward of 65°N. Surprisingly, these theoretical values are two orders of magnitude  
 1014 smaller than the measured  $\sim 0.97 \pm 0.13$  m thick snow layer during late winter at Scarp 1. The  
 1015 depth of  $\sim 0.97 \pm 0.13$  m due to snowfalls even significantly exceeds that of the frost layer due  
 1016 to direct condensation ( $0.64 \pm 0.18$  m at late winter). However, it's worth mentioning that  
 1017 there exist gaps in the MCS data in the lowest atmosphere (approximately up to 5 km in al-  
 1018 titude) where the instrument cannot probe through the optically thick clouds. This means that  
 1019 the effects of localized storms which can rapidly drive up snowfall rates were not captured in  
 1020 Alsaeed & Hayne (2022). In addition, zonal averaging applied in the MCS analysis can further  
 1021 erase out local aggregation of the snowfalls. Thus, the theoretical thickness values from Alsaeed  
 1022 & Hayne (2022) can only be considered as the lower limits. Then, it should be interesting to  
 1023 obtain snowfall thicknesses at active scarps over the entire North Pole (Section 5.7) and check  
 1024 if our measurements are consistently way higher than the modeled ones. If yes, that would mean  
 1025 the snowfalls on Mars are much more frequent and violent than we thought and the cloud set-  
 1026 tling model applied by Alsaeed & Hayne (2022) is missing some important ingredients. As the  
 1027 condensed water ice particles serve as condensation nuclei for the CO<sub>2</sub> particles during atmo-  
 1028 spheric deposition, higher CO<sub>2</sub> snowfall rates then mean a larger fraction of the Martian wa-  
 1029 ter cycle happens through this scavenging mechanism at the poles.

### 1030 5.7 Availability of ice blocks across the North Pole

1031 Here we discuss the spatial availability of the ice blocks as to examine the maximum cov-  
 1032 erage of upcoming mass-application of the proposed approaches.

1033 Russell et al. (2010, 2012) examined HiRISE images covering  $\sim 70$  Basal Unit outcrops  
 1034 around the NPLDs for scattered ice blocks and debris on Basal Unit slopes, and qualitatively  
 1035 grouped a total of 20 potentially active outcrops into three categories in terms of “likelihood  
 1036 of recent mass-wasting activity”. None of the peripheral scarps without Basal Unit exposure  
 1037 features likely mass-wasted NPLD detritus at their base (Russell et al., 2012). This indicates  
 1038 an important role the Basal Unit may play in steepness of the scarps and the related mass wast-  
 1039 ing processes. These active scarps are spatially limited to be within 80°N and 85°N. In addi-  
 1040 tion, there exists no active scarps in Gemina Lingula and Gemini Scopuli due to the lack Basal  
 1041 Unit outcrops (Fishbaugh & Head III, 2005; Nerozzi et al., 2022). However, the number of HiRISE  
 1042 observations available was relatively small back then in 2012.

1043 We seek to carry out a comprehensive search for scarps with ice blocks where our approach  
 1044 can be potentially applicable to get insights into the condensation/sublimation cycle of the po-  
 1045 lar seasonal deposits. The search is done by merely examining the available HiRISE images.

1046 Note that there also exist other optical images captured by Mars Express’s High Resolution Stereo  
1047 Camera (HRSC; [Neukum & Jaumann, 2004](#)), the MRO Context Camera (CTX; [Malin et al.,](#)  
1048 [2007](#)), and the ExoMars Trace Gas Orbiter (TGO) Colour and Stereo Surface Imaging System  
1049 (CaSSIS; [N. Thomas et al., 2017](#)). However, the best resolution of these images can range from  
1050 4 to 12.5 m/pixel, which is not enough to even capture the ice blocks with maximum size of  
1051  $\sim 5$  m ([Fanara et al., 2020b](#)). The search combines two aspects of efforts: (1) We locate all of  
1052 the sites over the NPLDs and their close vicinity where have been observed for at least five times,  
1053 and randomly select a summer image for visual inspection of fallen ice blocks. Multiple images  
1054 of the same sites can facilitate the cross-validation of the obtained snow/ice thickness values  
1055 and enable insights into the interannual depth variations (Section 5.3). It should be noted that  
1056 these regions of interest are not limited to steep marginal scarps, but can also cover spiral troughs  
1057 that expose stratigraphic layers (Figure 4), ice-filled craters over the residual polar cap, dynamic  
1058 dune fields, and so forth; (2) We make use of the topographic information from a reference DEM  
1059 gridded from updated and adjusted MOLA profiles ([Xiao, Stark, Schmidt, Hao, Steinbrügge,](#)  
1060 [et al., 2022](#)), and examine all available summer images that overlap with indicated sloped sur-  
1061 faces (with slope greater than an empirical threshold of  $15^\circ$ ). If there are visible ice blocks, then  
1062 we mark the corresponding scarp as positive. We set no height constraints on the ice blocks as  
1063 they should be at least tall enough to resolve the thin layer of seasonal deposits during middle-  
1064 to-late northern spring. Actually, the pixel size of HiRISE (down to 0.25 m) limits the detec-  
1065 tion of ice blocks and shadows under 0.71 m in size and length, respectively ( $2\sqrt{2}=2.83$  pix-  
1066 els). Thus, the images themselves have already filtered out small ice blocks. In reality, there  
1067 should exist a large quantify of these small blocks, as indicated by the frequency-size distribu-  
1068 tion of detected newly-fallen ice blocks, which generally follows a power law ([Fanara et al., 2020b](#)).

1069 The reference DEM is derived based on the co-registration technique ([Gläser et al., 2013;](#)  
1070 [Stark et al., 2015](#)). We apply the concept of “self-registration” to improve the positioning of in-  
1071 dividual laser profiles. A random subset of laser profiles (fixed at 0.25) is selected and then co-  
1072 registered to a footprint point cloud formed from the remaining profiles. After enough repeats  
1073 (set to 30), we effectively remove all offsets between the profiles due to residual errors in laser  
1074 alignment calibration, spacecraft attitude, timing, and trajectory. In Text S1, we perform a prob-  
1075 abilistic analysis on the number of iterations needed to be performed in the self-registration pro-  
1076 cess which justifies the repeats for up to 30 times. The DEM is gridded with 1 km in pixel size  
1077 and cannot fully resolve steep scarps (normally with a width of some hundreds of meters in the  
1078 images or less depending on the steepness), instead the indicated slopes are average represen-  
1079 tative over large-scale topography, for example, the transition zone between NPLDs and Basal  
1080 Unit. The DEM pixels with slope greater than an empirical threshold of  $15^\circ$  are shown in Fig-  
1081 ure 17. This relatively low threshold is set to ensure that all scarps with ice block presence will  
1082 lie in the search path. The extracted sloped surfaces include the marginal scarps, with heights  
1083 that range from 200 m to more than 1,200 m, delineated by [Massé et al. \(2012\)](#). Indeed, this

1084 relatively low threshold also leads to plenty of instances of spiral troughs being indicated as can-  
 1085 didates to search for ice blocks.

1086 We locate 138 sites of which there are, at least, 5 different observations and an additional  
 1087 of 210 sites, a majority of which feature no repeated observation or with only one extra cov-  
 1088 erage, along the sloped surfaces indicated by the MOLA terrain model. The summer images  
 1089 at those sites are manually examined and the ones with presence of ice blocks are shown in Fig-  
 1090 ure 17. A total of 66 images over various locations show signs of recent activity (39 out of 138  
 1091 and 27 out of 210 from the two categories, respectively). Active scarps with more than or equal  
 1092 to 5 repeated observations cluster in Olympia Rupes (including Scarp 1), Abalos Scopuli, and  
 1093 Boreum Cavus together with Tenius Cavus within Chasma Boreale. Apart from Olympia Ru-  
 1094 pes and Chasma Boreale, active scarps located through slope indicator extend to Rupes Tenuis  
 1095 and Gemini Scopuli. However, it's worth mentioning that the scarps at Olympia Rupes, Aba-  
 1096 los Scopuli, and Chasma Boreale are much more dynamic than those at the other places, as in-  
 1097 dicated by the large number of aprons of debris and ice blocks spotted there. These mass-wasting  
 1098 activities are spatially correlated with Basal Unit exposure at their base (compare to Figure 2  
 1099 in [Nerozzi et al. \(2022\)](#)). In contrast, scarps along Rupes Tenuis lack apparent aprons of de-  
 1100bris but ice blocks reside right at the layered terrain of the scarps (refer to Inset 1 in Figure 17  
 1101 for an example). Actually, Rupes Tenuis itself belongs to the exposed Basal Unit, and not the  
 1102 NPLDs. However, to prevent unnecessary confusion, we do not attempt to distinguish these scarps  
 1103 from those of the NPLDs. Scarps in Gemini Scopuli over Gemina Lingula also lack aprons of  
 1104 debris, and ice blocks are large in quantity and extremely uniformly-distributed at close vicin-  
 1105 ity of the scarps (refer to Inset 2 in Figure 17 for an example). Comparing the summer images  
 1106 in MY29 and MY36 at the location of Inset 2 shows no apparent fracture-caused detachment  
 1107 of fragments over the scarp, indicating these ice blocks, being contiguous to the scarp, may be  
 1108 anteriorly emplaced. The scarps with visible ice blocks spatially cover latitudes from 78°N to  
 1109 86°N. In terms of longitude, there exist a major gap from 27°E to 117°E over the Gemini Scop-  
 1110uli where Udzha Crater (81.8°N, 75.0°E) is the only site that has been spotted with ice blocks  
 1111 (refer to Figure 17 for location). It should be noted that the complete set of HiRISE images  
 1112 that have been examined do not cover all of the scarps. When searching through the images,  
 1113 only the ones acquired in the summertime have been downloaded and inspected. Additionally,  
 1114 there exist gaps in HiRISE coverage of the scarps which can be expected to be gradually bridged  
 1115 as more upcoming observations have been planned. As such, the set of scarps with presence of  
 1116 ice blocks presented in Figure 17 should stand as the lower limit on the maximum spatial ex-  
 1117 tend of the expected outputs by the proposed approaches.

1118 With ice blocks being spatially limited to high latitudes where the thickest seasonal layer  
 1119 is expected ([Xiao, Stark, Schmidt, Hao, Steinbrügge, et al., 2022](#); [Gary-Bicas et al., 2020](#)), rocks  
 1120 at regions surrounding the north polar cap, either over the crater rims or between the dune fields  
 1121 in the polar erg, and at lower latitudes can also be utilized for the purpose of measuring the

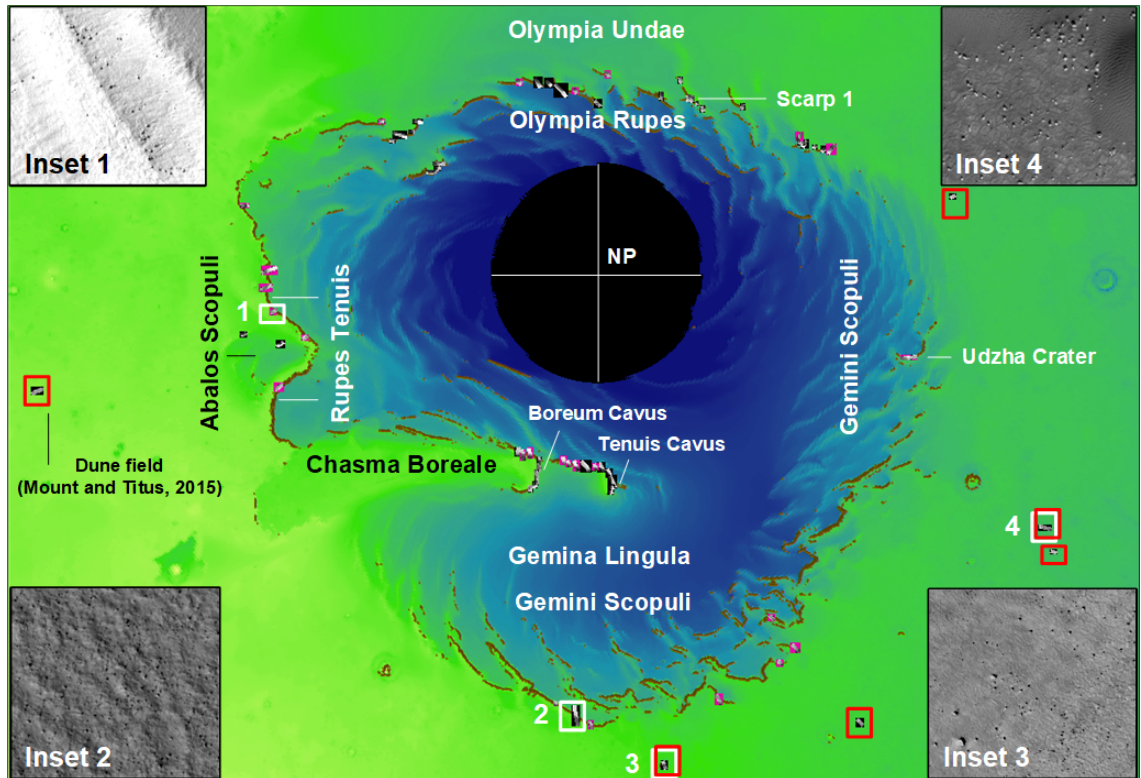


Figure 17: Locations of scarps with presence of ice blocks as examined in the HiRISE images. Locations with slope greater than  $15^\circ$ , represented by dark orange points, are draped over the 1 km/pixel reference DEM from reprocessed and then self-registered MOLA profiles (Xiao, Stark, Schmidt, et al., 2021). Images with the presence of ice blocks at locations where at least five repeated observations have been made by the HiRISE camera are shown with black background. Meanwhile, images examined to feature ice blocks along troughs and scarps indicated by MOLA slope map are exhibited with pink background. Images enclosed by white rectangles are taken as examples and enlarged in the corresponding insets to show the present ice blocks (Insets 1 and 2) and rocks (Insets 3 and 4), respectively. Images enclosed by red rectangles are examples with the presence of rocks in the circumpolar regions, including the polar erg, that is, massive dune fields surrounding the NPLDs. The barchanoid dune field with rocks at ( $75^\circ\text{N}$ ,  $282^\circ\text{E}$ ), studied in Mount & Titus (2015) to infer the depth of the seasonal deposits, is marked. Names of regions that feature clusterings of scarps with ice blocks are annotated. The Udzha Crater is marked of which only the topmost sharp-edged rims rise above the polar layered deposits to hint at its circular shape. Scarp 1 studied in this paper is also marked for reference.

1122 thickness of the seasonal layer (Cull et al., 2010; Mount & Titus, 2015). Some typical rock sites  
1123 are enclosed by red rectangles in Figure 17, with Insets 3 and 4 showing zoom-in views of the  
1124 rocks over the crater rim and between the dune fields, respectively. For large boulders over the  
1125 craters and their vicinity, they could be ejected during the impacts. The dune field, named Dunes,  
1126 within which the rocks have been utilized in Mount & Titus (2015) to infer the thickness of the  
1127 seasonal deposits there is also taken as an example. Unfortunately, no rocks have been spot-  
1128 ted between the massive linear dune fields in Olympia Undae where maximum depth up to  $\sim 4$  m  
1129 and off-season thickness variations up to  $\sim 3$  m in magnitude have been claimed after examin-  
1130 ing the dynamic MOLA height records (Xiao, Stark, Schmidt, Hao, Steinbrügge, et al., 2022).  
1131 Instead, lingering patches of bright materials between the dunes have been spotted which can  
1132 persist throughout the northern summer. Early evidence suggested that they show more gyp-  
1133 sum than water ice signatures (Fishbaugh et al., 2007; Horgan et al., 2009). In addition to gyp-  
1134 sum, there might exist other evaporitic minerals as small interannual variations of these bright  
1135 patches have also been observed.

1136 By establishing the automatic “BOUNDing” approach to circumvent massive demands on  
1137 human resources and applying it to all available sites with ice blocks and rocks in the polar re-  
1138 gion, we can obtain good spatial samplings of the thickness evolution of the seasonal deposits  
1139 and shed comprehensive insights into the long-term vertical growth and retreat of the SNPC.  
1140 In particular, these results can be used to examine the question that if the seasonal deposits  
1141 are much shallower than the MOLA-derived results during springtime over the entire Martian  
1142 North Pole (Section 5.5)? If yes, that means the the average bulk density of the seasonal de-  
1143 posits in spring should be much higher than we thought, which can have implications for snow/ice  
1144 metamorphism and translucency of the deposits (for example, Eluszkiewicz et al., 2005; Mat-  
1145 suo & Heki, 2009; Mount & Titus, 2015; Xiao, Stark, Schmidt, Hao, Steinbrügge, et al., 2022).  
1146 The expected measurements can also shed light on the spatially variable proportions of direct  
1147 condensation as frosts and atmospheric precipitation as snowfalls in forming the seasonal layer.  
1148 These proportions can help determine if CO<sub>2</sub> snowing storms are much more frequent and vi-  
1149 olent than we thought (Section 5.6). Meanwhile, “SUBTRACTing” can be applied to specific  
1150 (relatively tall) ice blocks to look into the thickness evolution at individual spots of interest.  
1151 Possible significant interannual depth variations with magnitudes of more than 0.2 m can be  
1152 identified and interpreted in the context of Martian climate change. Those enhanced understand-  
1153 ings can place crucial constraints on the Martian volatile cycles and climate models (for exam-  
1154 ple, Mischna et al., 2003; Forget et al., 2013). Meanwhile, the thickness of the seasonal layer  
1155 can assist in designing of future landers, rovers, or helicopters that are to drill in the spiral troughs  
1156 and decipher the Late Amazonian climate of Mars stored in the NPLDs (I. B. Smith et al., 2020;  
1157 Matthies et al., 2022).

## 1158 5.8 Limitations and outlook

1159 Spatially and temporally inhomogeneous growth and retreat of the seasonal polar caps  
 1160 have been identified and analyzed over various seasons using the MOLA records (Xiao, Stark,  
 1161 Schmidt, Hao, Su, et al., 2022; Xiao, Stark, Schmidt, Hao, Steinbrügge, et al., 2022). Unfor-  
 1162 tunately, a realistic error propagation is not possible without ground truth for assessment. As  
 1163 a result, the unexpected features observed, for example, exceptionally high maximum depth ( $\sim 4$  m)  
 1164 and off-season depth trends observed within Olympia Undae, remain to be verified from inde-  
 1165 pendent dataset. Indeed, current accuracy assessment of the MOLA results rely merely on in-  
 1166 direct evidence, for example, cross-validation of results from various teams or deviations from  
 1167 expected values (normally zero) at specific regions and solar longitudes (D. E. Smith et al., 2001;  
 1168 Aharonson et al., 2004; Xiao, Stark, Schmidt, Hao, Su, et al., 2022; Xiao, Stark, Schmidt, Hao,  
 1169 Steinbrügge, et al., 2022). The large biases in MOLA-derived results during spring as stated  
 1170 in Section 5.5 stress the importance of proper calibration of the MOLA results.

1171 Although temporally limited to late winter and spring (Section 4) and spatially confined  
 1172 to high latitudes (Section 5.7), the results by inspecting the ice blocks and rocks over the North  
 1173 Pole in HiRISE images can serve to calibrate the existing MOLA results. Then, extrapolation  
 1174 of the calibrated MOLA results to uncovered latitudes can be implemented in combination of  
 1175 boundary constraints, for example, CROCUS dates from optical cameras and thermal infrared  
 1176 spectrometers (for example, Schmidt et al., 2009; Piqueux et al., 2015). The term introduced  
 1177 by Kieffer et al. (2000), is a helpful mnemonic marker, which identifies the time in spring at  
 1178 which the snow/ice has completely disappeared. Meanwhile, these expected results can serve  
 1179 as ground truth for validating the processing procedure of the SHARAD radar sounding and  
 1180 altimetric measurements for the purpose of looking into the depth evolution of the seasonal de-  
 1181 posits. These radar records harbor the potential to decipher long-term depth evolution patterns  
 1182 of both seasonal polar caps of Mars (for example, Raguso & Nunes, 2021; Steinbrügge et al.,  
 1183 2021). As an ongoing activity, we seek to establish and apply the automatic “BOUNDing” ap-  
 1184 proach to HiRISE images acquired over all active scarps and at fields with presence of rocks  
 1185 at the Martian North Pole (Section 5.7). Meanwhile, we also advocate for more future obser-  
 1186 vations of the HiRISE camera of the active scarps and circumpolar rock fields at the North Pole,  
 1187 including stereo pairs.

1188 The depth evolution curves from “SUBTRACTing” and “BOUNDing” can achieve an un-  
 1189 certainty of better than 0.1 m at best scenarios, which is mainly limited by the spatial resolu-  
 1190 tion of the HiRISE camera (down to 0.25 m). This dictates that delicate interannual variations,  
 1191 for example, less than  $\sim 0.2$  m, cannot be confidently detected at the current stage. Thus, fu-  
 1192 ture super-resolution cameras to orbit Mars would dramatically enhance the performance of  
 1193 the proposed approaches to delve into the snow/ice depth evolution patterns. Indeed, the Mars  
 1194 Next Orbiter Science Analysis Group (NEX-SAG) already identified a baseline instrument of  
 1195 a super-high-resolution optical imager (HiRISE class at 30 cm/pixel; or even with a better res-

1196 olution of 10 – 15 cm/pixel) to reveal detailed morphology over limited areas for science and  
1197 site reconnaissance (Zurek et al., 2021). This recommended imager is capable of, for example,  
1198 capturing stratigraphic details, and thus the Late Amazonian climate records, stored in the po-  
1199 lar layered deposits (I. B. Smith et al., 2020) and better observing various surface dynamics such  
1200 as those related to slopes (Dundas et al., 2021).

1201 Using MOLA-measured thickness variations of the seasonal deposits from Xiao, Stark, Schmidt,  
1202 Hao, Su, et al. (2022) and Xiao, Stark, Schmidt, Hao, Steinbrügge, et al. (2022), Wagner et al.  
1203 (2023) modeled the loading-induced lithospheric deflection based on mechanical properties of  
1204 the Martian interior. They found that the deflection can be up to  $\sim 6$  cm in magnitude at the  
1205 poles and can be unambiguously detected by upcoming Interferometric Synthetic Aperture Radars  
1206 (InSARs) or next-generation laser altimeters. We note that the thickness variations of the sea-  
1207 sonal deposits from MOLA altimetric records were retrieved by examining the surface height  
1208 changes, which actually represent the combined effects of CO<sub>2</sub> deposition/sublimation and the  
1209 resultant lithospheric deflection. In contrast, thickness measurements from “SUBTRACTing”  
1210 and “BOUNDing” are obtained by examining the shadows of the ice blocks and thus remain un-  
1211 affected by the lithospheric deflection. It is anticipated that we can extract the periodic litho-  
1212 spheric deflection by comparing the surface height variations from future InSARs or laser al-  
1213 timeters with the seasonal deposit thicknesses from examining the ice blocks. Constraints on  
1214 the lithospheric deflection can inform us about the structure and rheology of the Martian crust  
1215 and mantle which have important implications for Mars’ thermal history. It will be challeng-  
1216 ing to differentiate between currently plausible Mars interior models as the precision in mea-  
1217 suring the deflection would need to be in the millimeter or even sub-millimeter level (Wagner  
1218 et al., 2023). However, this proposed concept does harbor some potential by including a large  
1219 amount of independent surface height variation and snow/ice depth measurements for spatial  
1220 and temporal averaging purposes. The fact that the lithospheric deflection peaks at high po-  
1221 lar latitudes where ice blocks are located further enhances the feasibility of the measuring con-  
1222 cept. Meanwhile, a future super-high-resolution optical imager to Mars would greatly build up  
1223 the prospects (Zurek et al., 2021). A factor that will need to be considered and thoroughly mod-  
1224 eled in the determination of the subtle lithospheric deflection is the solid body tidal deforma-  
1225 tion from the Sun and Phobos which maximizes at around the equator and reduces to less than  
1226 1 cm at the poles (Wagner et al., 2023).

## 1227 6 Conclusion

1228 We propose to use the shadow variations of the ice blocks at the foot of the NPLD steep  
1229 scarps, complementing that of the rocks, to infer the vertical evolution of the Martian seasonal  
1230 deposits. We relate the shadow length of an ice block to its height using a rigorous geometric  
1231 model, which is based on bundle adjusted and orthorectified high-resolution HiRISE images and  
1232 takes both the solar and slope properties into consideration. Building on this model, we present

1233 two independent and yet complementary approaches: (1) “SUBTRACTing” that subtracts the  
1234 ice block heights in the summer to that observed in the spring; (2) “BOUNDing” that locates  
1235 ice blocks that have been completely covered to place lower limits on the thickness of the sea-  
1236 sonal deposits, and ice blocks that still stick out of the seasonal cover to put upper limits. We  
1237 experimentally apply the methods to a steep scarp centered at (85.0°N, 151.5°E). The results  
1238 show that the average thickness due to accumulation of snowfalls in MY31 is  $0.97\pm 0.13$  m at  
1239  $L_s = 350.7^\circ$  in late winter,  $0.64\pm 0.08$  m at  $L_s = 7.0^\circ$  in early spring,  $0.21\pm 0.05$  m at  $L_s =$   
1240  $42.8^\circ$  in middle spring, and gradually decreases towards summer solstice ( $L_s = 90^\circ$ ). The max-  
1241 imum snowfall thickness of  $\sim 1$  m is two orders of magnitude larger than theoretical values pre-  
1242 dicted by [Alsaeed & Hayne \(2022\)](#). We proceed to make reasonable assumptions and use the  
1243 widening of the ice blocks as a proxy to approximate the depth of the directly condensed layer  
1244 over the ice blocks. We show that average thickness of the frost layer in MY31 reaches  $0.64\pm 0.18$  m  
1245 at  $L_s = 350.7^\circ$  in late winter, quasi-linearly declines to  $0.26\pm 0.03$  m at  $L_s = 42.8^\circ$  in middle  
1246 spring and to  $0.045\pm 0.035$  m at  $L_s = 69.5^\circ$  in late spring. We thus show that atmospheric de-  
1247 position as snowfalls, compared to direct surface condensation as frosts, can even contribute  
1248 more to the thickness and volume of the seasonal snow/ice layer at Scarp 1 during wintertime.  
1249 The aggregate thickness of the seasonal deposits at Scarp 1 in MY31 then stands at  $1.63\pm 0.22$  m  
1250 at  $L_s = 350.7^\circ$  in late winter which then gradually declines to  $0.45\pm 0.06$  m at  $L_s = 42.8^\circ$  in  
1251 middle spring and  $0.06\pm 0.05$  m at  $L_s = 69.5^\circ$  in late spring. The majority of the associated  
1252 uncertainties can be better than  $\sim 0.1$  m. Compared to the existing MOLA results, our thick-  
1253 ness estimates are consistently lower, by a magnitude of up to 0.8 m, throughout the spring.  
1254 We attribute a large portion of these inconsistencies to biases inherited in the MOLA-derived  
1255 thickness measurements. The available HiRISE images can temporally span from MY29 to MY36  
1256 (2008 to 2021), and we observe the snowfall thickness in the very early spring in MY36 is  $1.01\pm 0.10$  m,  
1257 exceeding that in MY31 by a magnitude of  $0.36\pm 0.13$  m. Building on this study, we will de-  
1258 velop automatic version of the approaches and extend the measurements to all scarps with pres-  
1259 ence of ice blocks, covered by multiple HiRISE images at the same time, at the Martian North  
1260 Pole. Meanwhile, we will also apply the proposed approaches to the circumpolar regions with  
1261 presence of rocks to extend the thickness evolution measurements to lower polar latitudes. These  
1262 expected results can answer the raised question that if the seasonal cap over the entire Mar-  
1263 tian North Pole during its recession in spring is much shallower than we previously thought?  
1264 Meanwhile, the proportions of snowfall and frosts in constituting the seasonal deposits over the  
1265 entire polar region can be expected to be revealed. These future results can also serve as ground  
1266 truth to calibrate previous MOLA results and validate contemporary anticipated SHARAD re-  
1267 sults. Besides, these expected outcomes can help to examine the long-term spatial-temporal het-  
1268 erogeneity of the surface-atmosphere exchange and determine the mass balance of the NPLDs.  
1269 As such, we suggest more frequent targeting of the HiRISE camera to the active scarps where  
1270 ice blocks exist and circumpolar fields with presence of rocks. Meanwhile, anticipated super-  
1271 high-resolution optical cameras to Mars would enable unambiguous identification of small in-

1272 terannual depth variations, for example, less than 0.2 m in magnitude, of the seasonal deposits.  
 1273 Thickness measurements from examining the ice blocks, in combination with high-precision sur-  
 1274 face height variations from future InSARs or laser altimeters, have the potential of inferring the  
 1275 polar dynamic lithospheric deflection which can shed light on the Martian interior.

## 1276 Acknowledgments

1277 The authors would like to thank Nicholas L. Wagner (Baylor University) and Noora R. Alsaeed  
 1278 (University of Colorado Boulder) for helpful discussions. We also acknowledge the MRO and  
 1279 HiRISE teams for providing the great products that enabled this research. SS thanks the China  
 1280 Scholarship Council (CSC) for financial support of studying in Germany. FS acknowledges sup-  
 1281 port from the “Institut National des Sciences de l’Univers” (INSU), the “Centre National de la  
 1282 Recherche Scientifique” (CNRS), and “Centre National d’Etudes Spatiales” (CNES) through  
 1283 the “Programme National de Planétologie.” LML and PJG acknowledge financial support from  
 1284 project PID2021-126365NB-C21 (MCI/AEI/FEDER, UE) and from the grant CEX2021-001131-  
 1285 S funded by MCI/AEI/ 10.13039/501100011033.

## 1286 Author contributions

1287 **Conceptualization:** HX; **Formal Analysis:** HX, FS, and PJG; **Funding Acquisition:** HX;  
 1288 **Investigation:** HX and YX; **Methodology:** HX, FS, and PJG; **Project Administration:**  
 1289 HX; **Software:** HX and SS; **Visualization:** HX and YX; **Supervision:** HX, PJG, FS, and  
 1290 LML; **Validation:** HX; **Writing – original draft:** HX; **Writing – review & editing:** HX,  
 1291 SS, PJG, FS, and LML.

## 1292 Conflict of Interest

1293 The authors declare no conflicts of interest relevant to this study.

## 1294 Open Research

1295 HiRISE images are available at <https://www.uahirise.org/hiwish/browse> and [https://ode](https://ode.rsl.wustl.edu/mars/)  
 1296 [.rsl.wustl.edu/mars/](https://ode.rsl.wustl.edu/mars/) (accessed on 20 December 2022). The self-registered MOLA reference  
 1297 DEM and thickness variation time series from Xiao, Stark, Schmidt, Hao, Steinbrügge, et al.  
 1298 (2022) at the North Pole are published under <https://doi.org/10.17632/x953mzxxvv.1> (Xiao,  
 1299 Stark, Schmidt, et al., 2021, accessed on 12 May 2023). The SPICE kernels used for calcula-  
 1300 tion of the solar condition are available at [https://naif.jpl.nasa.gov/pub/naif/pds/data/](https://naif.jpl.nasa.gov/pub/naif/pds/data/mgs-m-spice-6-v1.0/mgsp_1000/data/)  
 1301 [mgs-m-spice-6-v1.0/mgsp\\_1000/data/](https://naif.jpl.nasa.gov/pub/naif/pds/data/mgs-m-spice-6-v1.0/mgsp_1000/data/) (accessed on 18 March 2023).

## 1302 References

1303 Acton, C. H. J. (1996). Ancillary data services of NASA’s Navigation and Ancillary Information

- 1304 Facility. *Planetary and Space Science*, *44*(1), 65–70. doi: 10.1016/0032-0633(95)00107-7
- 1305 Aharonson, O., Zuber, M. T., Smith, D. E., Neumann, G. A., Feldman, W. C., & Prettyman,  
1306 T. H. (2004). Depth, distribution, and density of CO<sub>2</sub> deposition on Mars. *Journal of*  
1307 *Geophysical Research: Planets*, *109*(E5). doi: 10.1029/2003JE002223
- 1308 Alsaeed, N., & Hayne, P. O. (2022). Transport of water into the polar regions of Mars through  
1309 scavenging by CO<sub>2</sub> snowfall. *Journal of Geophysical Research: Planets*, *127*(11),  
1310 e2022JE007386. doi: 10.1029/2022JE007386
- 1311 Andrieu, F., Schmidt, F., Douté, S., & Chassefière, E. (2018). Ice state evolution during spring  
1312 in Richardson crater, Mars. *Icarus*, *315*, 158–173. doi: 10.1016/j.icarus.2018.06.019
- 1313 Appéré, T., Schmitt, B., Langevin, Y., Douté, S., Pommerol, A., Forget, F., . . . Bibring, J.-P.  
1314 (2011). Winter and spring evolution of northern seasonal deposits on Mars from OMEGA on  
1315 Mars Express. *Journal of Geophysical Research: Planets*, *116*(E5). doi:  
1316 10.1029/2010JE003762
- 1317 Becerra, P., Smith, I. B., Hibbard, S., Andres, C., Bapst, J., Bramson, A. M., . . . Yoldi, Z.  
1318 (2021). Past, present, and future of Mars polar science: Outcomes and outlook from the 7<sup>th</sup>  
1319 International Conference on Mars Polar Science and Exploration. *Planetary Science Journal*,  
1320 *2*(5), 209. doi: 10.3847/PSJ/ac19a5
- 1321 Becerra, P., Sori, M. M., & Byrne, S. (2017). Signals of astronomical climate forcing in the  
1322 exposure topography of the North Polar Layered Deposits of Mars. *Geophysical Research*  
1323 *Letters*, *44*(1), 62–70. doi: 10.1002/2016GL071197
- 1324 Benson, J. L., Kass, D. M., & Kleinböhl, A. (2011). Mars’ north polar hood as observed by the  
1325 Mars Climate Sounder. *Journal of Geophysical Research: Planets*, *116*(E3). doi:  
1326 10.1029/2010JE003693
- 1327 Beyer, R. A., Alexandrov, O., & McMichael, S. (2018). The Ames Stereo Pipeline: NASA’s open  
1328 source software for deriving and processing terrain data. *Earth and Space Science*, *5*(9),  
1329 537–548. doi: 10.1029/2018EA000409
- 1330 Blackburn, D. G., Bryson, K. L., Chevrier, V. F., Roe, L. A., & White, K. F. (2010).  
1331 Sublimation kinetics of CO<sub>2</sub> ice on Mars. *Planetary and Space Science*, *58*(5), 780–791. doi:  
1332 10.1016/j.pss.2009.12.004
- 1333 Botev, Z. I., Grotowski, J. F., & Kroese, D. P. (2010). Kernel density estimation via diffusion.  
1334 *Annals of Statistics*, *38*(5), 2916–2957. doi: 10.1214/10-AOS799
- 1335 Brothers, S., Kocurek, G., & Holt, J. (2018). Sequence architecture of the cavi unit, Chasma  
1336 Boreale, Mars. *Icarus*, *308*, 42–60. doi: 10.1016/j.icarus.2017.06.024
- 1337 Brothers, T., Holt, J., & Spiga, A. (2015). Planum Boreum basal unit topography, Mars:  
1338 Irregularities and insights from SHARAD. *Journal of Geophysical Research: Planets*, *120*(7),  
1339 1357–1375. doi: 10.1002/2015JE004830
- 1340 Brown, A. J., Calvin, W. M., Becerra, P., & Byrne, S. (2016). Martian north polar cap summer  
1341 water cycle. *Icarus*, *277*, 401–415. doi: 10.1016/j.icarus.2016.05.007

- 1342** Byrne, S., Sori, M., Russell, P., Pathare, A., Becerra, P., Molaro, J., . . . Team, H. (2017). Mars  
**1343** polar cliffs: Stressed out and falling apart. In *European Planetary Science Congress* (Vol. 11).  
**1344** Calvin, W., James, P., Cantor, B., & Dixon, E. (2015). Interannual and seasonal changes in the  
**1345** north polar ice deposits of Mars: Observations from MY 29–31 using MARCI. *Icarus*, *251*,  
**1346** 181–190. doi: 10.1016/j.icarus.2014.08.026
- 1347** Cull, S., Arvidson, R. E., Mellon, M., Wiseman, S., Clark, R., Titus, T., . . . McGuire, P. (2010).  
**1348** Seasonal H<sub>2</sub>O and CO<sub>2</sub> ice cycles at the Mars Phoenix landing site: 1. Prelanding CRISM and  
**1349** HiRISE observations. *Journal of Geophysical Research: Planets*, *115*(E4). doi:  
**1350** 10.1029/2009JE003340
- 1351** Defraigne, P., de Viron, O., Dehant, V., Van Hoolst, T., & Hourdin, F. (2000). Mars rotation  
**1352** variations induced by atmosphere and ice caps. *Journal of Geophysical Research: Planets*,  
**1353** *105*(E10), 24563–24570. doi: 10.1029/1999JE001227
- 1354** Dundas, C. M., Becerra, P., Byrne, S., Chojnacki, M., Daubar, I. J., Diniega, S., . . . Valantinas,  
**1355** A. (2021). Active Mars: A dynamic world. *Journal of Geophysical Research: Planets*, *126*(8),  
**1356** e2021JE006876. doi: 10.1029/2021JE006876
- 1357** Eluszkiewicz, J., Moncet, J.-L., Titus, T. N., & Hansen, G. B. (2005). A microphysically-based  
**1358** approach to modeling emissivity and albedo of the Martian seasonal caps. *Icarus*, *174*(2),  
**1359** 524–534. doi: 10.1016/j.icarus.2004.05.025
- 1360** Fanara, L., Gwinner, K., Hauber, E., & Oberst, J. (2020a). Automated detection of block falls  
**1361** in the north polar region of Mars. *Planetary and Space Science*, *180*, 104733. doi:  
**1362** 10.1016/j.pss.2019.104733
- 1363** Fanara, L., Gwinner, K., Hauber, E., & Oberst, J. (2020b). Present-day erosion rate of north  
**1364** polar scarps on Mars due to active mass wasting. *Icarus*, *342*, 113434. doi:  
**1365** 10.1016/j.icarus.2019.113434
- 1366** Fishbaugh, K. E., & Head III, J. W. (2005). Origin and characteristics of the Mars north polar  
**1367** basal unit and implications for polar geologic history. *Icarus*, *174*(2), 444–474. doi:  
**1368** 10.1016/j.icarus.2004.06.021
- 1369** Fishbaugh, K. E., Poulet, F., Chevrier, V., Langevin, Y., & Bibring, J.-P. (2007). On the origin  
**1370** of gypsum in the Mars north polar region. *Journal of Geophysical Research: Planets*, *112*(E7).  
**1371** doi: 10.1029/2006JE002862
- 1372** Forget, F., Wordsworth, R., Millour, E., Madeleine, J.-B., Kerber, L., Leconte, J., . . . Haberle,  
**1373** R. M. (2013). 3D modelling of the early Martian climate under a denser CO<sub>2</sub> atmosphere:  
**1374** Temperatures and CO<sub>2</sub> ice clouds. *Icarus*, *222*(1), 81–99. doi: 10.1016/j.icarus.2012.10.019
- 1375** Gary-Bicas, C., Hayne, P., Horvath, T., Heavens, N., Kass, D., Kleinböhl, A., . . . McCleese, D.  
**1376** (2020). Asymmetries in snowfall, emissivity, and albedo of Mars’ seasonal polar caps: Mars  
**1377** Climate Sounder observations. *Journal of Geophysical Research: Planets*, *125*(5),  
**1378** e2019JE006150. doi: 10.1029/2019JE006150
- 1379** Gläser, P., Haase, I., Oberst, J., & Neumann, G. A. (2013). Co-registration of laser altimeter

- 1380 tracks with digital terrain models and applications in planetary science. *Planetary and Space*  
 1381 *Science*, 89, 111–117. doi: 10.1016/j.pss.2013.09.012
- 1382 Golombek, M. P., Huertas, A., Marlow, J., Mcgrane, B., Klein, C., Martinez, M., ... Tamppari,  
 1383 L. K. (2008). Size-frequency distributions of rocks on the northern plains of Mars with special  
 1384 reference to Phoenix landing surfaces. *Journal of Geophysical Research: Planets*, 113(E3).  
 1385 doi: 10.1029/2007JE003065
- 1386 Grima, C., Kofman, W., Mouginot, J., Phillips, R. J., Hérique, A., Biccari, D., ... Cutigni, M.  
 1387 (2009). North polar deposits of Mars: Extreme purity of the water ice. *Geophysical Research*  
 1388 *Letters*, 36(3). doi: 10.1029/2008GL036326
- 1389 Hansen, C., Byrne, S., Portyankina, G., Bourke, M., Dundas, C., McEwen, A., ... Thomas, N.  
 1390 (2013). Observations of the northern seasonal polar cap on Mars: I. Spring sublimation  
 1391 activity and processes. *Icarus*, 225(2), 881–897. doi: 10.1016/j.icarus.2012.09.024
- 1392 Hansen, C., Thomas, N., Portyankina, G., McEwen, A., Becker, T., Byrne, S., ... Mellon, M.  
 1393 (2010). HiRISE observations of gas sublimation-driven activity in Mars' southern polar  
 1394 regions: I. Erosion of the surface. *Icarus*, 205(1), 283–295. doi: 10.1016/j.icarus.2009.07.021
- 1395 Hayward, R., Fenton, L., Tanaka, K., Titus, T., Colaprete, A., & Christensen, P. (2010). Mars  
 1396 Global Digital Dune Database: MC-1, US Geological Survey Open-File Report 2010–1170. *US*  
 1397 *Geological Survey: Flagstaff, AZ, USA*. doi: 10.3133/ofr20101170
- 1398 Head III, J. W., Hiesinger, H., Ivanov, M. A., Kreslavsky, M. A., Pratt, S., & Thomson, B. J.  
 1399 (1999). Possible ancient oceans on Mars: Evidence from Mars Orbiter Laser Altimeter data.  
 1400 *Science*, 286(5447), 2134–2137. doi: 10.1126/science.286.5447.2134
- 1401 Hepburn, A. J., Holt, T., Hubbard, B., & Ng, F. (2019). Creating HiRISE digital elevation  
 1402 models for Mars using the open-source Ames Stereo Pipeline. *Geoscientific Instrumentation,*  
 1403 *Methods and Data Systems*, 8(2), 293–313. doi: 10.5194/gi-8-293-2019
- 1404 Hood, D. R., Sholes, S. F., Karunatillake, S., Fassett, C. I., Ewing, R. C., & Levy, J. (2022).  
 1405 The Martian Boulder Automatic Recognition System, MBARS. *Earth and Space Science*,  
 1406 9(9), e2022EA002410. doi: 10.1029/2022EA002410
- 1407 Horgan, B., Bell III, J., Noe Dobreá, E., Cloutis, E., Bailey, D., Craig, M., ... Mustard, J.  
 1408 (2009). Distribution of hydrated minerals in the north polar region of Mars. *Journal of*  
 1409 *Geophysical Research: Planets*, 114(E1). doi: 10.1029/2008JE003187
- 1410 Kieffer, H. H., Titus, T. N., Mullins, K. F., & Christensen, P. R. (2000). Mars south polar  
 1411 spring and summer behavior observed by TES: Seasonal cap evolution controlled by frost  
 1412 grain size. *Journal of Geophysical Research: Planets*, 105(E4), 9653–9699. doi:  
 1413 10.1029/1999JE001136
- 1414 Laskar, J., Levrard, B., & Mustard, J. F. (2002). Orbital forcing of the Martian Polar Layered  
 1415 Deposits. *Nature*, 419(6905), 375–377. doi: 10.1038/nature01066
- 1416 Leighton, R. B., & Murray, B. C. (1966). Behavior of carbon dioxide and other volatiles on  
 1417 Mars. *Science*, 153(3732), 136–144. doi: 10.1126/science.153.3732.136

- 1418 Le Maistre, S., Rivoldini, A., Caldiero, A., Yseboodt, M., Baland, R.-m., Beuthe, M., ...  
 1419 Banerdt, W. B. (2023). Spin state and deep interior structure of Mars from InSight radio  
 1420 tracking. *Nature*, 1–5. doi: 10.1038/s41586-023-06150-0
- 1421 Leys, C., Ley, C., Klein, O., Bernard, P., & Licata, L. (2013). Detecting outliers: Do not use  
 1422 standard deviation around the mean, use absolute deviation around the median. *Journal of*  
 1423 *Experimental Social Psychology*, 49(4), 764–766. doi: 10.1016/j.jesp.2013.03.013
- 1424 Määttänen, A., & Montmessin, F. (2021). Clouds in the Martian atmosphere. In *Oxford*  
 1425 *Research Encyclopedia of Planetary Science*. doi: 10.1093/acrefore/9780190647926.013.114
- 1426 Malin, M. C., Bell, J. F., Cantor, B. A., Caplinger, M. A., Calvin, W. M., Clancy, R. T., ...  
 1427 Wolff, M. J. (2007). Context Camera Investigation on board the Mars Reconnaissance  
 1428 Orbiter. *Journal of Geophysical Research: Planets*, 112(E5). doi: 10.1029/2006JE002808
- 1429 Massé, M., Bourgeois, O., Le Mouélic, S., Verpoorter, C., Spiga, A., & Le Deit, L. (2012). Wide  
 1430 distribution and glacial origin of polar gypsum on Mars. *Earth and Planetary Science Letters*,  
 1431 317, 44–55.
- 1432 Matsuo, K., & Heki, K. (2009). Seasonal and inter-annual changes of volume density of Martian  
 1433 CO<sub>2</sub> snow from time-variable elevation and gravity. *Icarus*, 202(1), 90–94. doi:  
 1434 10.1016/j.icarus.2009.02.023
- 1435 Matthies, L., Kennett, A., Kerber, L., Fraeman, A., & Anderson, R. C. (2022). Prospects for  
 1436 very long-range Mars rover missions. In *2022 IEEE Aerospace Conference (AERO)* (pp. 1–11).  
 1437 doi: 10.1109/AERO53065.2022.9843681
- 1438 McEwen, A. S. (2005). *MRO Mars High Resolution Image Science Experiment EDR V1.0*.  
 1439 NASA Planetary Data System. doi: 10.17189/1520179
- 1440 McEwen, A. S., Eliason, E. M., Bergstrom, J. W., Bridges, N. T., Hansen, C. J., Delamere,  
 1441 W. A., ... Weitz, C. M. (2007). Mars Reconnaissance Orbiter's High Resolution Imaging  
 1442 Science Experiment (HiRISE). *Journal of Geophysical Research: Planets*, 112(E5). doi:  
 1443 10.1029/2005JE002605
- 1444 McGlasson, R. A., Bramson, A. M., Morgan, G. A., & Sori, M. M. (2023). Varied histories of  
 1445 outlier polar ice deposits on Mars. *Journal of Geophysical Research: Planets*, e2022JE007592.  
 1446 doi: 10.1029/2022JE007592
- 1447 Mc Keown, L., Diniega, S., Portyankina, G., Hansen, C., Aye, K., Piqueux, S., & Scully, J. E.  
 1448 (2023). Martian araneiforms: A review. *Journal of Geophysical Research: Planets*, 128(4).  
 1449 doi: 10.1029/2022JE007684
- 1450 Métivier, L., Karatekin, Ö., & Dehant, V. (2008). The effect of the internal structure of Mars on  
 1451 its seasonal loading deformations. *Icarus*, 194(2), 476–486. doi: 10.1016/j.icarus.2007.12.001
- 1452 Mischna, M. A., Richardson, M. I., Wilson, R. J., & McCleese, D. J. (2003). On the orbital  
 1453 forcing of Martian water and CO<sub>2</sub> cycles: A general circulation model study with simplified  
 1454 volatile schemes. *Journal of Geophysical Research: Planets*, 108(E6). doi:  
 1455 10.1029/2003JE002051

- 1456 Mount, C. P., & Titus, T. N. (2015). Evolution of Mars' northern polar seasonal CO<sub>2</sub> deposits:  
1457 Variations in surface brightness and bulk density. *Journal of Geophysical Research: Planets*,  
1458 *120*(7), 1252–1266. doi: 10.1002/2014JE004706
- 1459 Nagle-McNaughton, T. P., Williams, J. M., Gallegos, Z. E., Wilkie, H. A., Martinez, D. C., &  
1460 Scuderi, L. A. (2020). Geographic information system based detection and quantification of  
1461 boulders using HiRISE imagery: A case study in Jezero Crater. *Journal of Applied Remote*  
1462 *Sensing*, *14*(1), 014522–014522. doi: 10.1117/1.JRS.14.014522
- 1463 Navarro, T., Madeleine, J.-B., Forget, F., Spiga, A., Millour, E., Montmessin, F., & Määttänen,  
1464 A. (2014). Global climate modeling of the Martian water cycle with improved microphysics  
1465 and radiatively active water ice clouds. *Journal of Geophysical Research: Planets*, *119*(7),  
1466 1479–1495. doi: 10.1002/2013JE004550
- 1467 Nerozzi, S., & Holt, J. (2019). Buried ice and sand caps at the north pole of Mars: Revealing a  
1468 record of climate change in the cavi unit with SHARAD. *Geophysical Research Letters*,  
1469 *46*(13), 7278–7286. doi: 10.1029/2019GL082114
- 1470 Nerozzi, S., Ortiz, M. R., & Holt, J. W. (2022). The north polar basal unit of Mars: An  
1471 Amazonian record of surface processes and climate events. *Icarus*, *373*, 114716. doi:  
1472 10.1016/j.icarus.2021.114716
- 1473 Neukum, G., & Jaumann, R. (2004). HRSC: The high resolution stereo camera of Mars Express.  
1474 In *Mars Express: The Scientific Payload* (Vol. 1240, pp. 17–35).
- 1475 Neumann, G. A., Abshire, J. B., Aharonson, O., Garvin, J. B., Sun, X., & Zuber, M. T. (2003).  
1476 Mars Orbiter Laser Altimeter pulse width measurements and footprint-scale roughness.  
1477 *Geophysical Research Letters*, *30*(11), 1561. doi: 10.1029/2003GL017048
- 1478 Neumann, G. A., Rowlands, D. D., Lemoine, F. G., Smith, D. E., & Zuber, M. T. (2001).  
1479 Crossover analysis of Mars Orbiter Laser Altimeter data. *Journal of Geophysical Research:*  
1480 *Planets*, *106*(E10), 23753–23768. doi: 10.1029/2000JE001381
- 1481 Ojha, L., Nerozzi, S., & Lewis, K. (2019). Compositional constraints on the north polar cap of  
1482 Mars from gravity and topography. *Geophysical Research Letters*, *46*(15), 8671–8679. doi:  
1483 10.1029/2019GL082294
- 1484 Piqueux, S., Kleinböhl, A., Hayne, P. O., Kass, D. M., Schofield, J. T., & McCleese, D. J.  
1485 (2015). Variability of the Martian seasonal CO<sub>2</sub> cap extent over eight Mars Years. *Icarus*,  
1486 *251*, 164–180. doi: 10.1016/j.icarus.2014.10.045
- 1487 Plaut, J. J., Picardi, G., Safaeinili, A., Ivanov, A. B., Milkovich, S. M., Cicchetti, A., ...  
1488 Edenhofer, P. (2007). Subsurface radar sounding of the South Polar Layered Deposits of Mars.  
1489 *Science*, *316*(5821), 92–95. doi: 10.1126/science.1139672
- 1490 Pommerol, A., Appéré, T., Portyankina, G., Aye, K.-M., Thomas, N., & Hansen, C. (2013).  
1491 Observations of the northern seasonal polar cap on Mars III: CRISM/HiRISE observations of  
1492 spring sublimation. *Icarus*, *225*(2), 911–922. doi: 10.1016/j.icarus.2012.08.039
- 1493 Portyankina, G., Markiewicz, W. J., Thomas, N., Hansen, C. J., & Milazzo, M. (2010). HiRISE

- 1494 observations of gas sublimation-driven activity in Mars' southern polar regions: III. Models of  
 1495 processes involving translucent ice. *Icarus*, 205(1), 311–320. doi: 10.1016/j.icarus.2009.08.029  
 1496
- 1497 Raguso, M., & Nunes, D. (2021). Monitoring of CO<sub>2</sub> seasonal variations at the Martian polar ice  
 1498 caps using SHARAD data. In *Lunar and Planetary Science Conference* (p. 2438).
- 1499 Russell, P., Byrne, S., & Hansen, C. J. (2010). Active mass wasting of ice layers and seasonal  
 1500 CO<sub>2</sub> frost in the north polar region of Mars. In *Lunar and Planetary Science Conference*.
- 1501 Russell, P., Byrne, S., Pathare, A., & Herkenhoff, K. (2012). Active erosion and evolution of  
 1502 Mars north polar scarps. In *Lunar and Planetary Science Conference* (p. 2747).
- 1503 Russell, P., Thomas, N., Byrne, S., Herkenhoff, K., Fishbaugh, K., Bridges, N., . . . Alfred, M.  
 1504 (2008). Seasonally active frost-dust avalanches on a north polar scarp of Mars captured by  
 1505 HiRISE. *Geophysical Research Letters*, 35(23). doi: 10.1029/2008GL035790
- 1506 Schmidt, F., Douté, S., Schmitt, B., Vincendon, M., Bibring, J.-P., Langevin, Y., & the  
 1507 OMEGA Team. (2009). Albedo control of Seasonal South Polar Cap recession on Mars.  
 1508 *Icarus*, 200(2), 374–394. doi: 10.1016/j.icarus.2008.12.014
- 1509 Schmidt, F., & Portyankina, G. (2018). The exotic processes driving ephemeral seasonal surface  
 1510 change on Mars. In *Dynamic Mars: Recent and current landscape evolution of the Red Planet*  
 1511 (pp. 157–186). Elsevier. doi: 10.1016/B978-0-12-813018-6.00005-4
- 1512 Schmidt, F., Way, M. J., Costard, F., Bouley, S., Séjourné, A., & Aleinov, I. (2022).  
 1513 Circumpolar ocean stability on Mars 3 Gy ago. *Proceedings of the National Academy of*  
 1514 *Sciences*, 119(4), e2112930118. doi: 10.1073/pnas.2112930118
- 1515 Silverman, B. W. (1986). *Density estimation for statistics and data analysis* (Vol. 26). CRC  
 1516 press.
- 1517 Smith, D. E., Zuber, M. T., & Neumann, G. A. (2001). Seasonal variations of snow depth on  
 1518 Mars. *Science*, 294(5549), 2141–2146. doi: 10.1126/science.1066556
- 1519 Smith, I. B., Hayne, P. O., Byrne, S., Becerra, P., Kahre, M., Calvin, W., . . . Siegler, M. (2020).  
 1520 The Holy Grail: A road map for unlocking the climate record stored within Mars' Polar  
 1521 Layered Deposits. *Planetary and Space Science*, 184(May 2019). doi:  
 1522 10.1016/j.pss.2020.104841
- 1523 Sori, M. M., Becerra, P., Bapst, J., Byrne, S., & McGlasson, R. A. (2022). Orbital forcing of  
 1524 Martian climate revealed in a south polar outlier ice deposit. *Geophysical Research Letters*,  
 1525 49(6), e2021GL097450. doi: 10.1029/2021GL097450
- 1526 Sori, M. M., Byrne, S., Hamilton, C. W., & Landis, M. E. (2015). Viscous flow rates of icy  
 1527 topography on the North Polar Layered Deposits of Mars. *Geophysical Research Letters*,  
 1528 43(2), 541–549. doi: 10.1002/2015GL067298
- 1529 Stark, A., Oberst, J., Preusker, F., Gwinner, K., Peale, S. J., Margot, J.-L., . . . Solomon, S. C.  
 1530 (2015). Mercury's rotational parameters from MESSENGER image and laser altimeter data:  
 1531 A feasibility study. *Planetary and Space Science*, 117, 64–72. doi: 10.1016/j.pss.2015.05.006

- 1532 Steinbrügge, G., Haynes, M. S., Schroeder, D. M., Scanlan, K. M., Stark, A., Young, D. A., ...  
 1533 Blankenship, D. D. (2021). Altimetry measurements from planetary radar sounders and  
 1534 application to SHARAD on Mars. *IEEE Transactions on Geoscience and Remote Sensing*.  
 1535 doi: 10.1109/TGRS.2021.3134638
- 1536 Su, S., Fanara, L., Xiao, H., Hauber, E., & Oberst, J. (2023). Detection of detached  
 1537 ice-fragments at Martian polar scarps using a Convolutional Neural Network. *IEEE Journal of*  
 1538 *Selected Topics in Applied Earth Observations and Remote Sensing*. doi:  
 1539 10.1109/JSTARS.2023.3238968
- 1540 Su, S., Fanara, L., Zhang, X., Hauber, E., Gwinner, K., & Oberst, J. (2023). Searching for the  
 1541 sources of ice block falls at the Martian north polar scarps. *Icarus*, 390, 115321. doi:  
 1542 10.1016/j.icarus.2022.115321
- 1543 Thomas, N., Cremonese, G., Ziethe, R., Gerber, M., Brändli, M., Bruno, G., ... Wray, J. J.  
 1544 (2017). The Colour and Stereo Surface Imaging System (CaSSIS) for the ExoMars Trace Gas  
 1545 Orbiter. *Space Science Reviews*, 212(3), 1897–1944. doi: 10.1007/s11214-017-0421-1
- 1546 Thomas, P. C., Calvin, W., Cantor, B., Haberle, R., James, P. B., & Lee, S. W. (2016). Mass  
 1547 balance of Mars' residual south polar cap from CTX images and other data. *Icarus*, 268,  
 1548 118–130. doi: 10.1016/j.icarus.2015.12.038
- 1549 Van den Acker, E., Van Hoolst, T., de Viron, O., Defraigne, P., Forget, F., Hourdin, F., &  
 1550 Dehant, V. (2002). Influence of the seasonal winds and the CO<sub>2</sub> mass exchange between  
 1551 atmosphere and polar caps on mars' rotation. *Journal of Geophysical Research: Planets*,  
 1552 107(E7), 9–1. doi: 10.1029/2000JE001539
- 1553 Wagner, N. L., James, P. B., Ermakov, A. E., & Sori, M. M. (2023). Evaluating the use of  
 1554 seasonal surface displacements and time-variable gravity to constrain the interior of Mars. In  
 1555 *Authorea*. doi: 10.22541/essoar.169230247.71360068/v1
- 1556 Wang, H., & Ingersoll, A. P. (2002). Martian clouds observed by Mars Global Surveyor Mars  
 1557 Orbiter Camera. *Journal of Geophysical Research: Planets*, 107(E10), 8–1. doi:  
 1558 10.1029/2001JE001815
- 1559 Xiao, H., Stark, A., Schmidt, F., Hao, J., Steinbrügge, G., Wagner, N. L., ... Oberst, J. (2022).  
 1560 Spatio-temporal level variations of the Martian Seasonal North Polar Cap from co-registration  
 1561 of MOLA profiles. *Journal of Geophysical Research: Planets*, 127(10), e2021JE007158. doi:  
 1562 10.1029/2021JE007158
- 1563 Xiao, H., Stark, A., Schmidt, F., Hao, J., Steinbrügge, G., Cheng, Y., & Oberst, J. (2021).  
 1564 Spatio-temporal level variations of the Martian Seasonal North Polar Cap. *Mendeley Data*.  
 1565 doi: 10.17632/x953mzxxvv.1
- 1566 Xiao, H., Stark, A., Schmidt, F., Hao, J., Su, S., Steinbrügge, G., & Oberst, J. (2022).  
 1567 Spatio-temporal level variations of the Martian Seasonal South Polar Cap from co-registration  
 1568 of MOLA profiles. *Journal of Geophysical Research: Planets*, e2022JE007196. doi:  
 1569 10.1029/2022JE007196

- 1570** Xiao, H., Stark, A., Steinbrügge, G., Hussmann, H., & Oberst, J. (2021). Processing of laser  
**1571** altimeter Time-of-Flight measurements to geodetic coordinates. *Journal of Geodesy*. doi:  
**1572** 10.1007/s00190-020-01467-4
- 1573** Xiao, H., Stark, A., Steinbrügge, G., Thor, R., Schmidt, F., & Oberst, J. (2022). Prospects for  
**1574** mapping temporal height variations of the seasonal CO<sub>2</sub> snow/ice caps at the Martian poles  
**1575** by co-registration of MOLA Profiles. *Planetary and Space Science*, *214C*. doi:  
**1576** 10.1016/j.pss.2022.105446
- 1577** Zurek, R., Campbell, B., Byrne, S., Calvin, W., Carter, L., Clancy, R., . . . Pratt, L. (2021).  
**1578** Mars Next Orbiter Science Analysis Group (NEX-SAG): White Paper Report to the  
**1579** 2023-2032 Planetary Sciences and Astrobiology Decadal Survey. *Bulletin of the American*  
**1580** *Astronomical Society*, *53*(4), 038.

Figure 1.

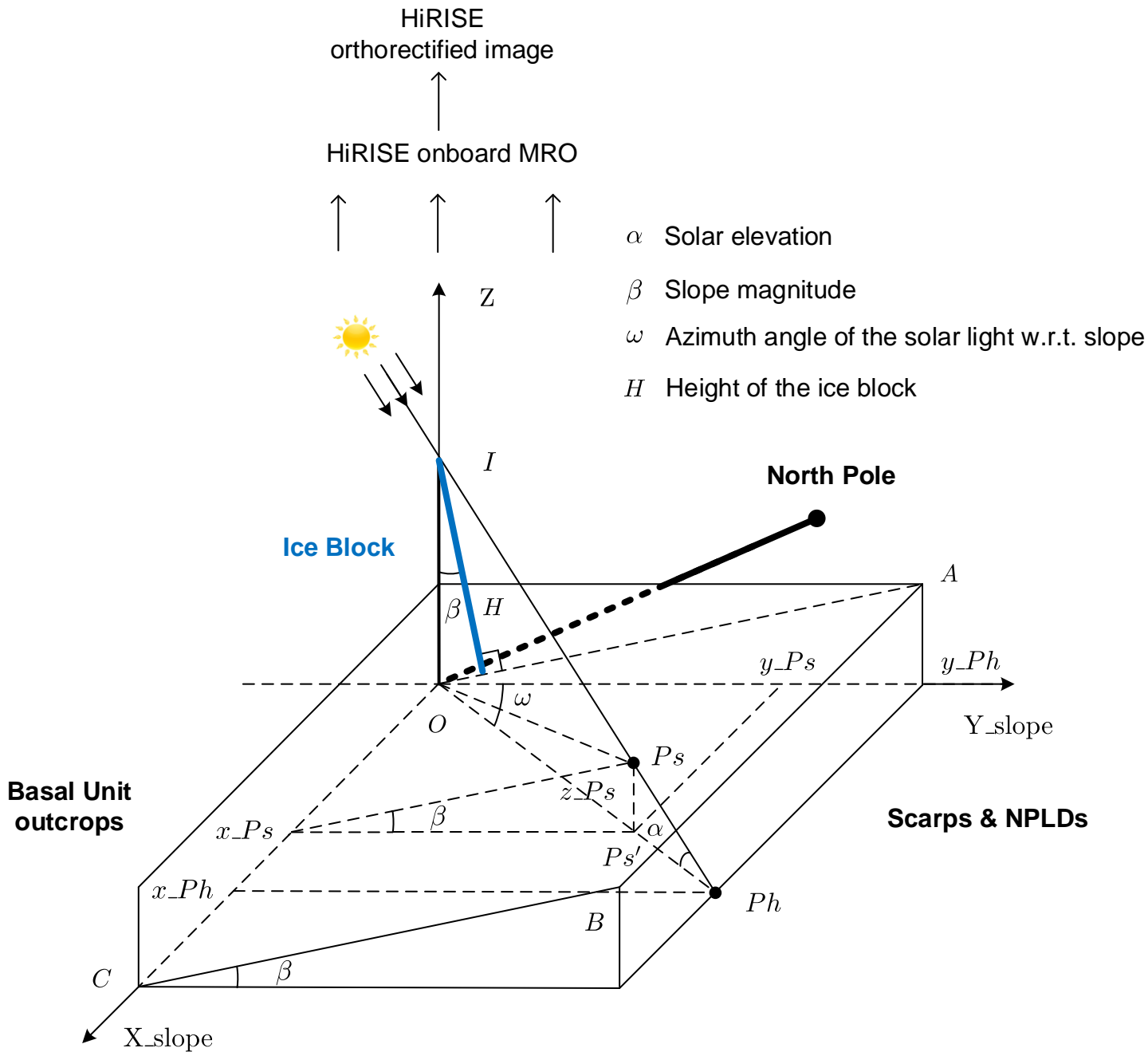


Figure 2.

-- dynamic surface @ late winter & early spring

-- dynamic surface @ mid-spring

-- dynamic surface @ late-spring

— static Basal Unit surface @ summer

IB : Ice Block

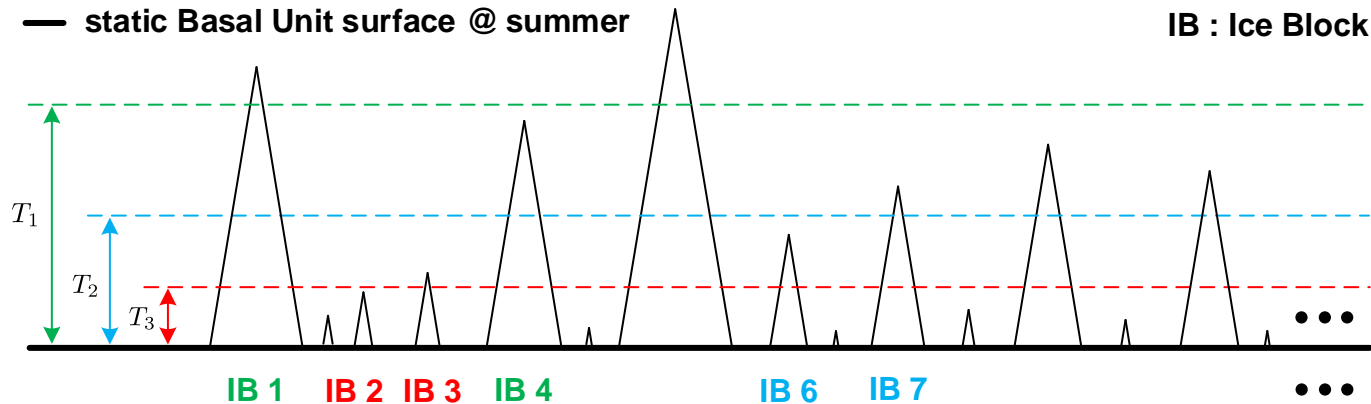


Figure 3.

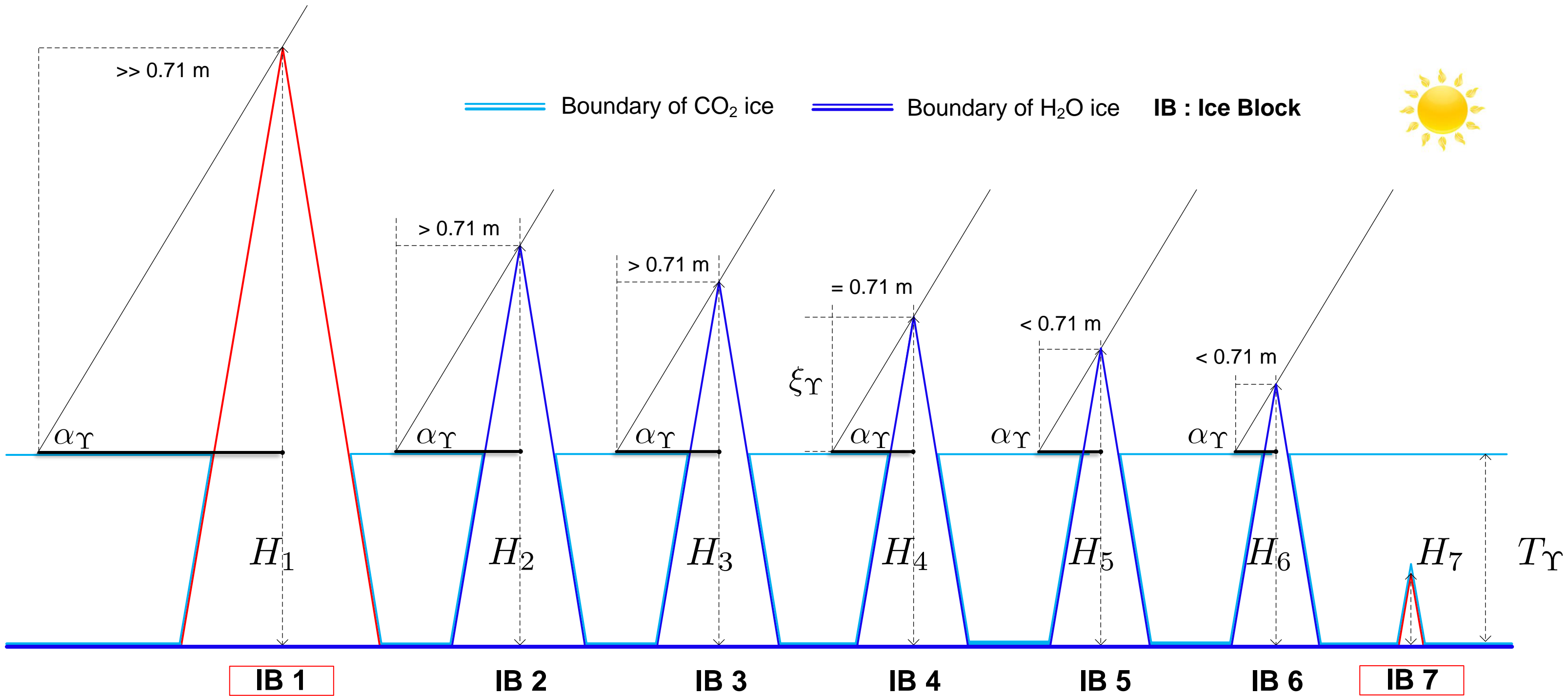


Figure 4.

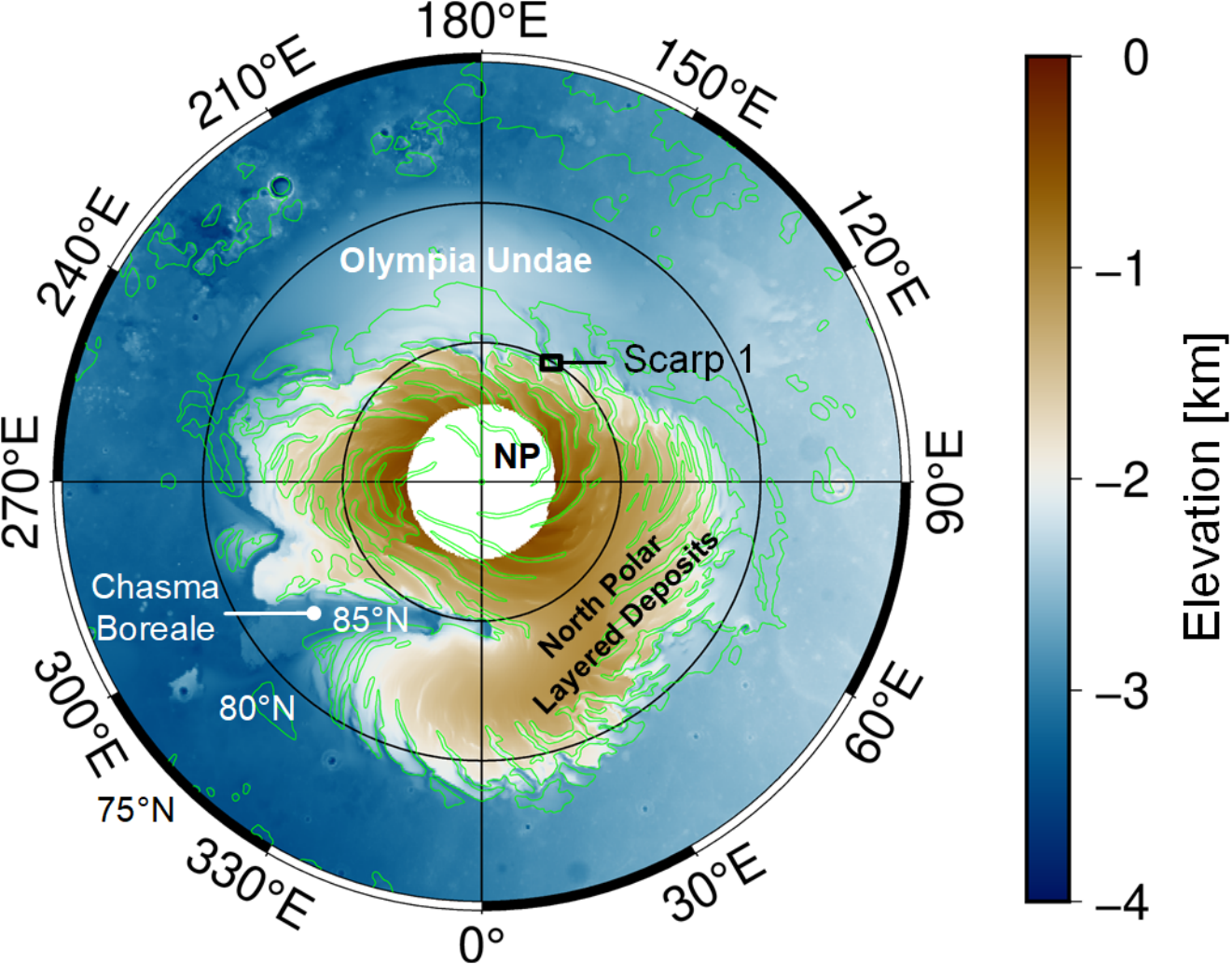
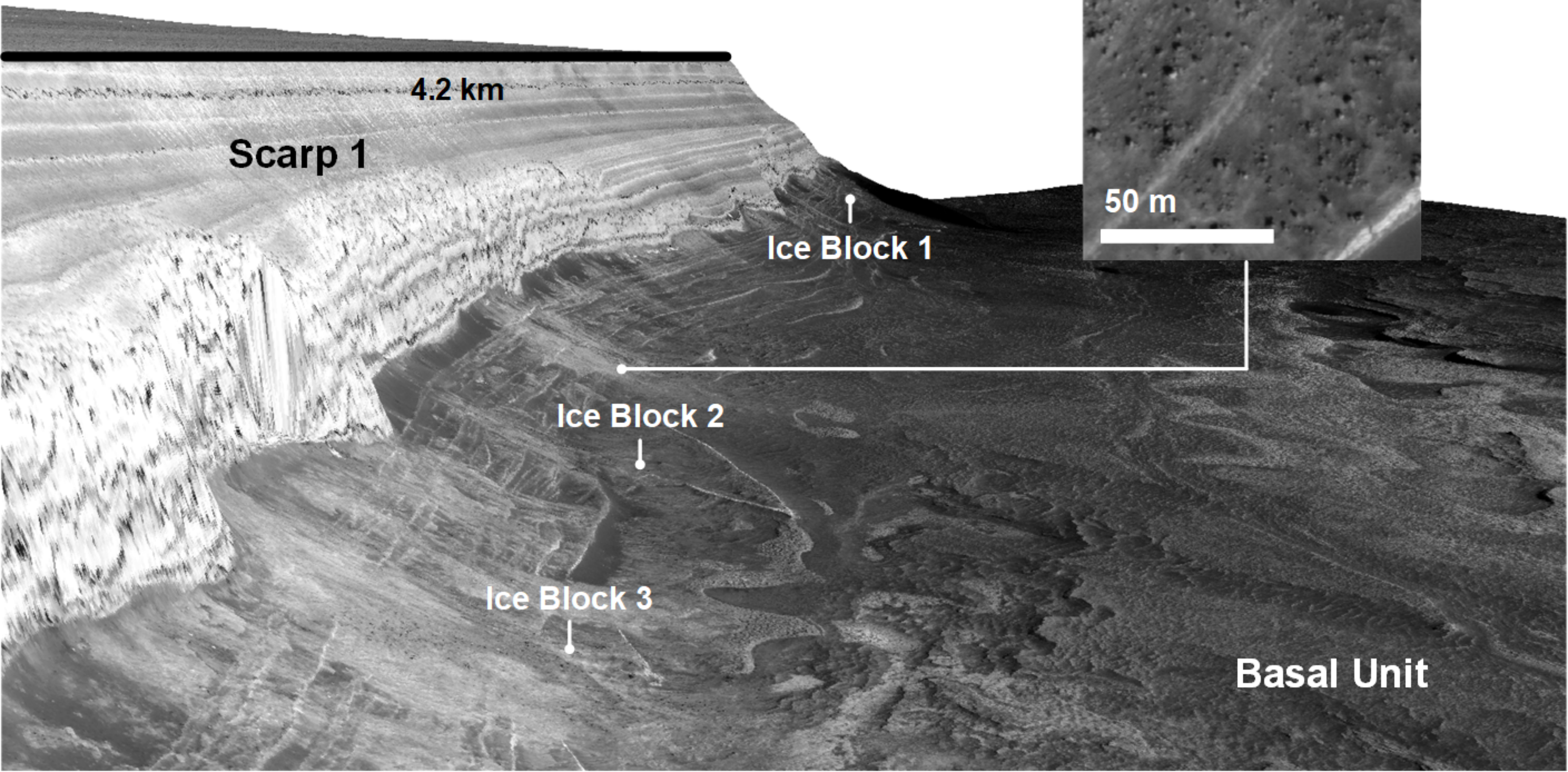


Figure 5.

**NPLDs**



4.2 km

**Scarp 1**

**Ice Block 1**

**Ice Block 2**

**Ice Block 3**

**Ice blocks**

50 m

**Basal Unit**

Figure 6.

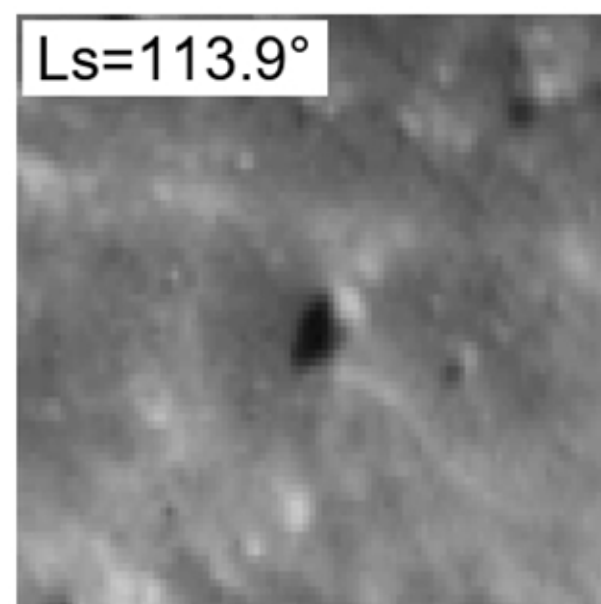
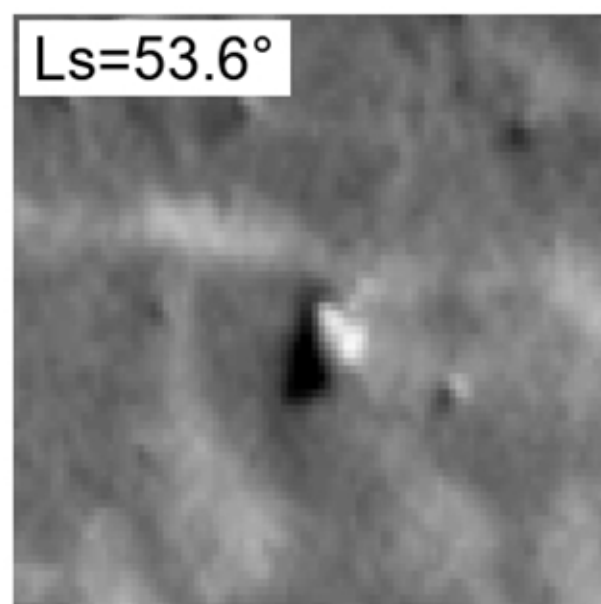
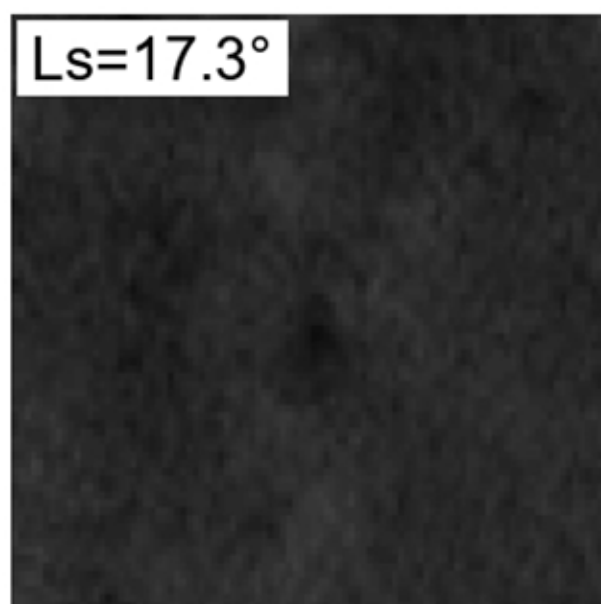
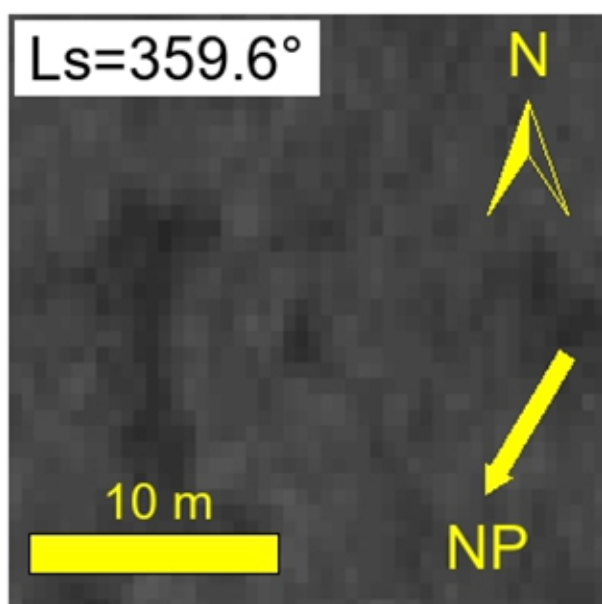
late winter

early spring

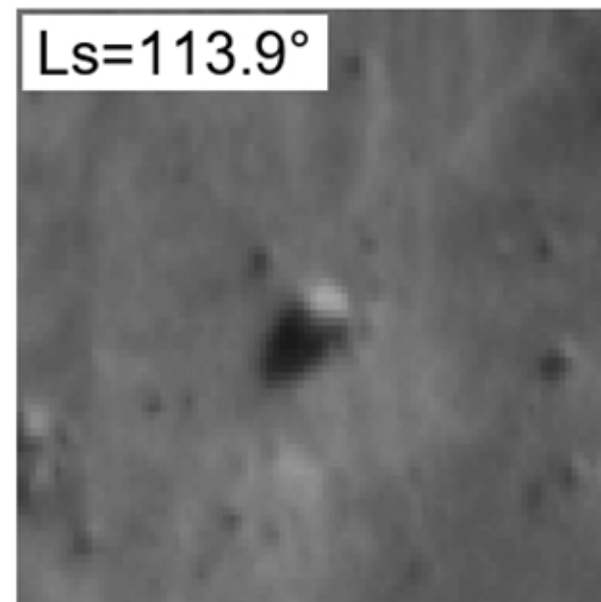
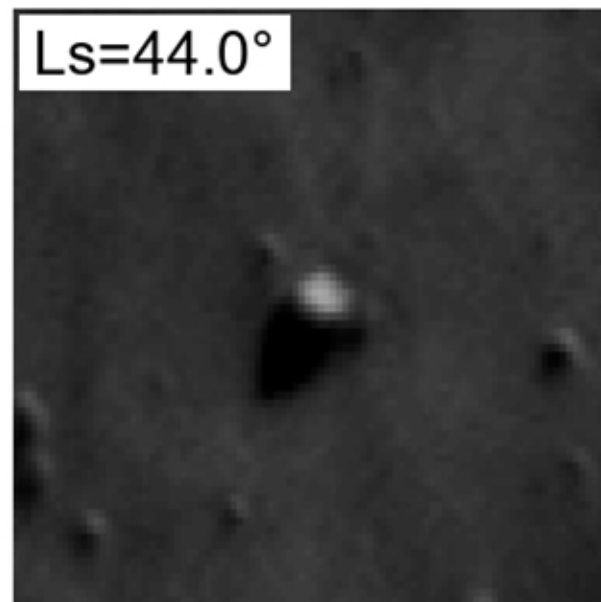
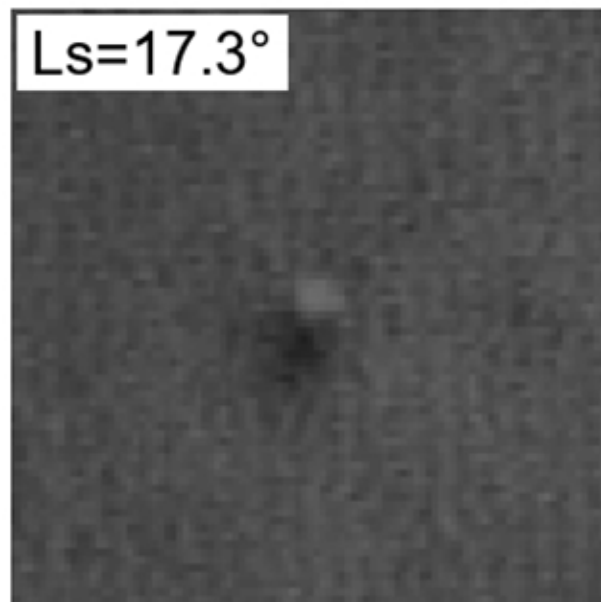
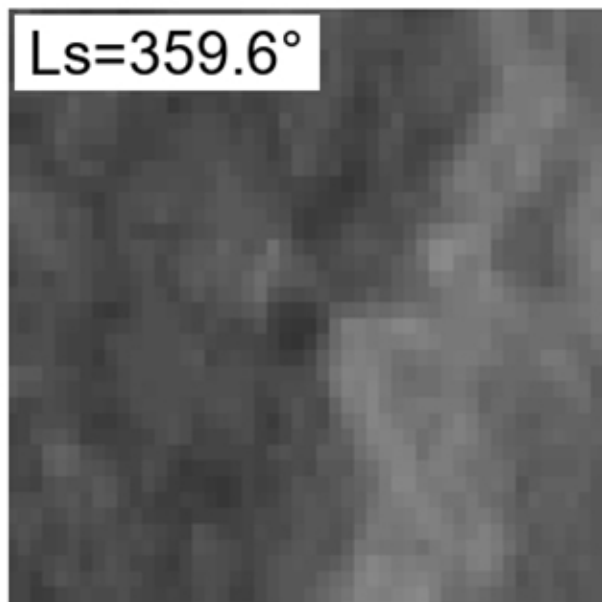
mid-to-late spring

summer

Ice Block 1



Ice Block 2



Ice Block 3

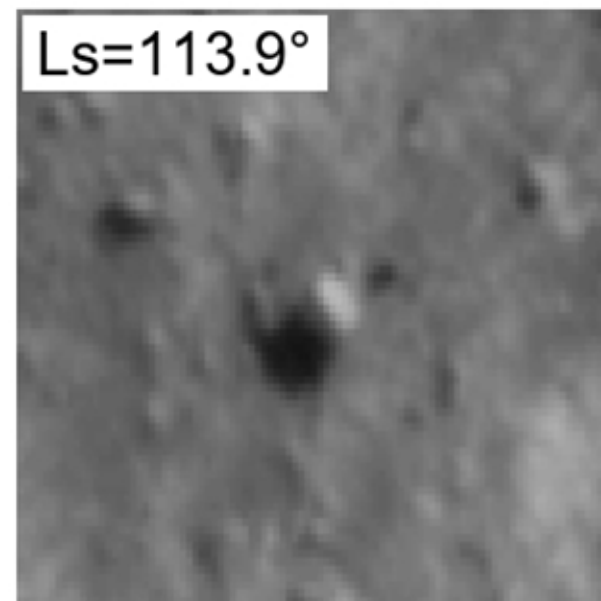
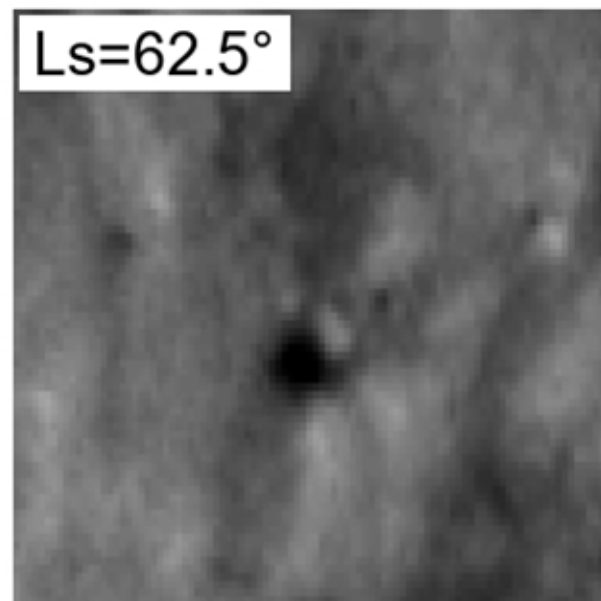
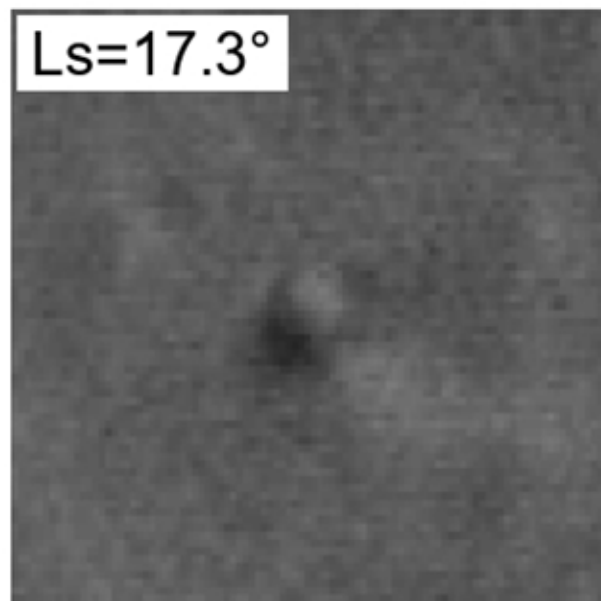
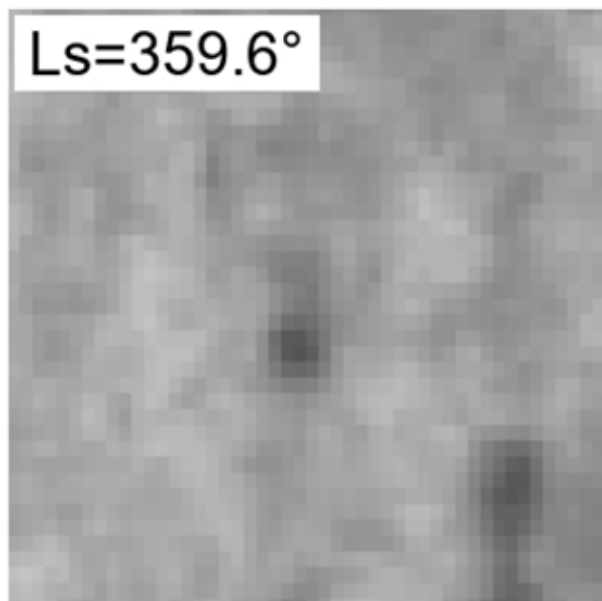
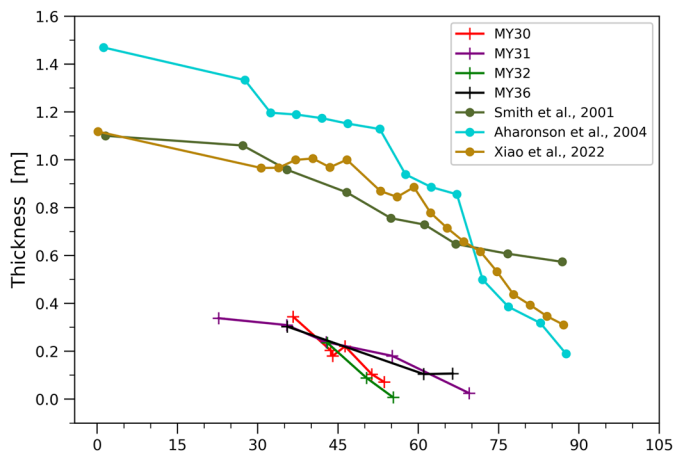


Figure 7.



**Ice Block 1**

**Ice Block 2**

**Ice Block 3**

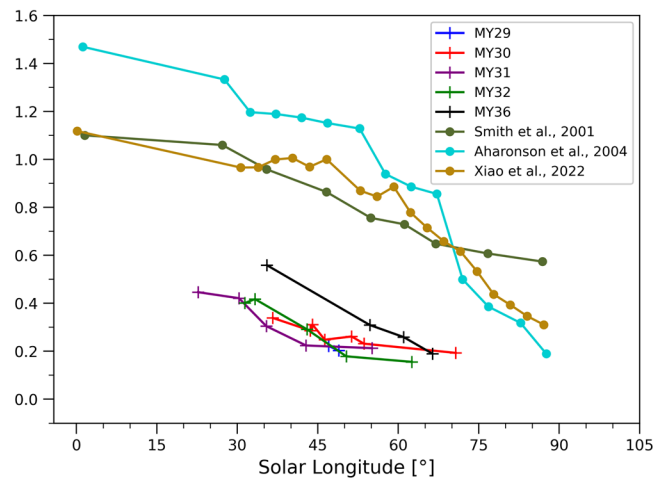
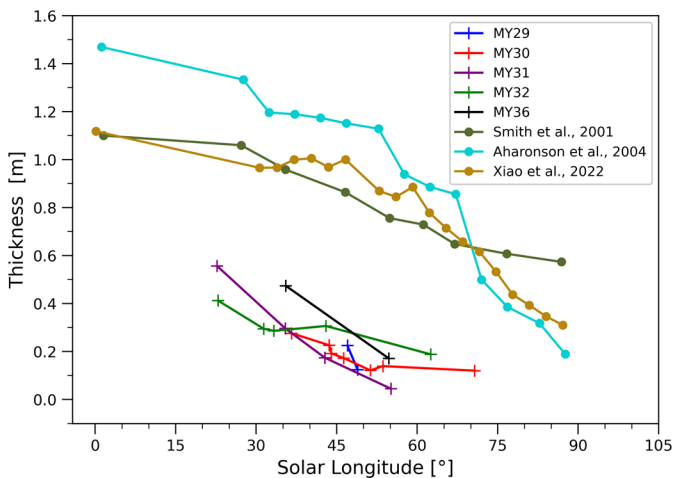


Figure 8.

# Ice blocks fully covered

# Ice blocks NOT fully covered

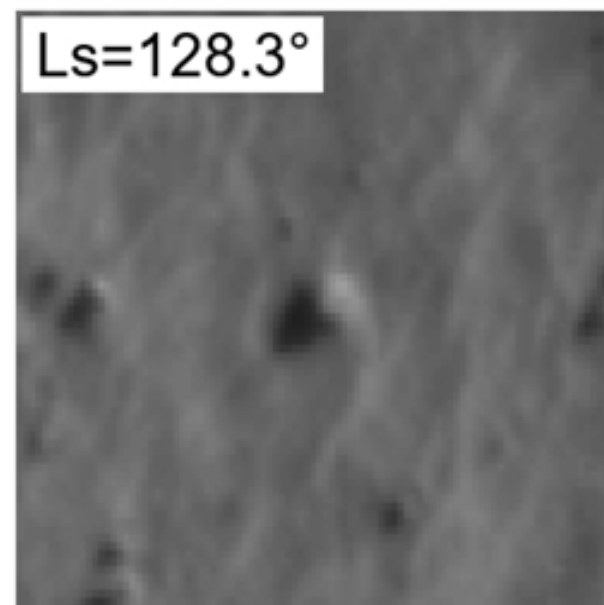
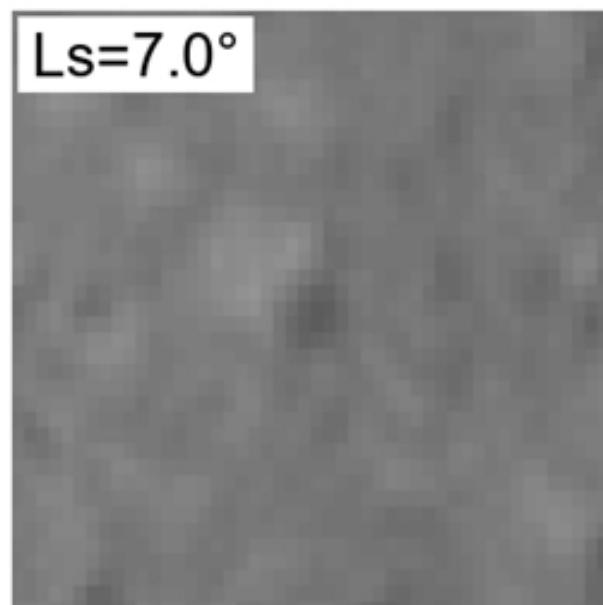
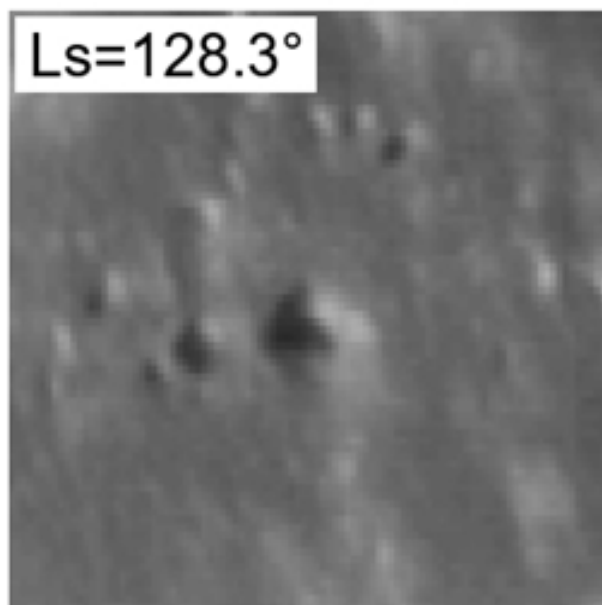
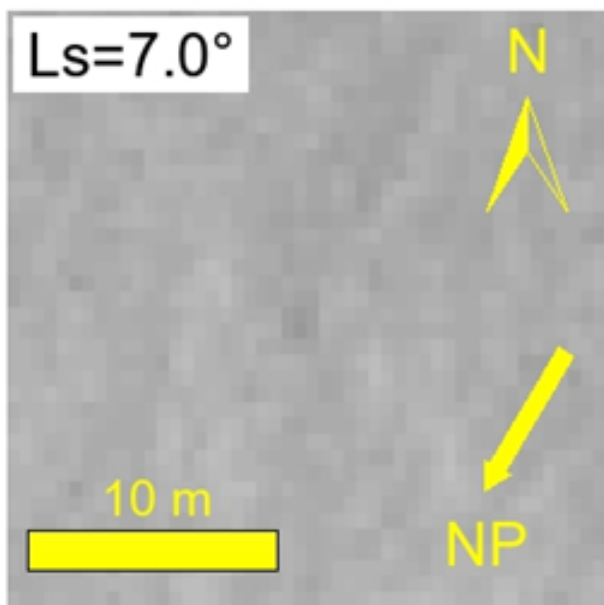
early spring

summer

early spring

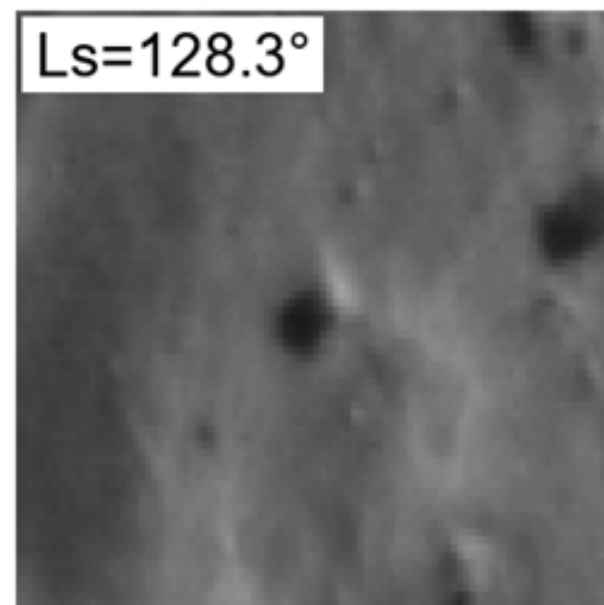
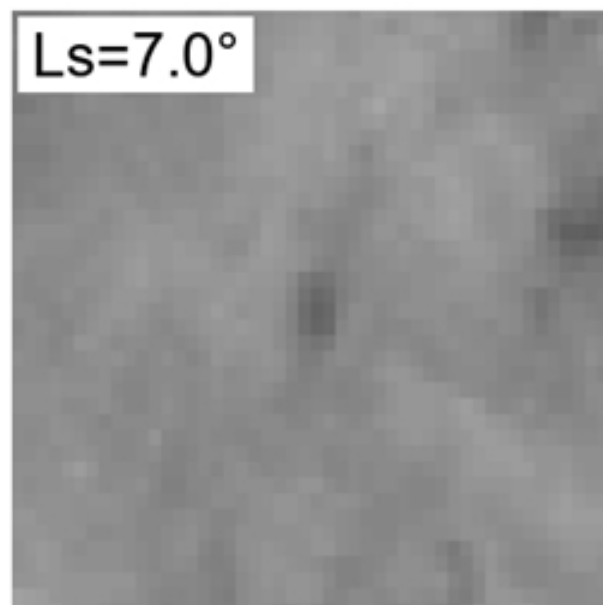
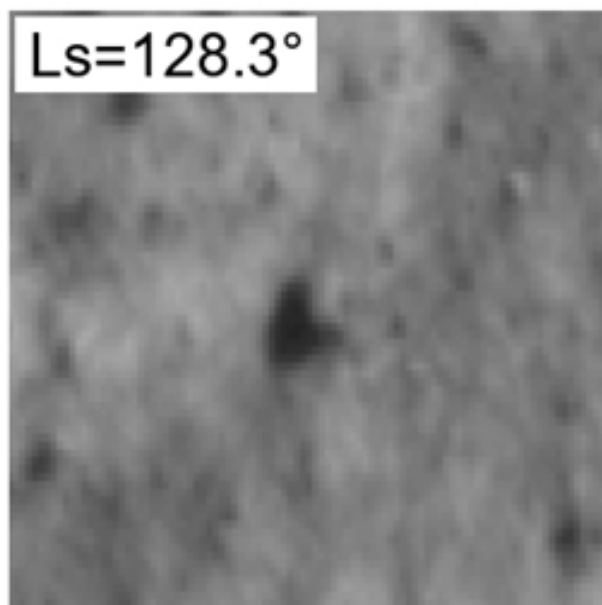
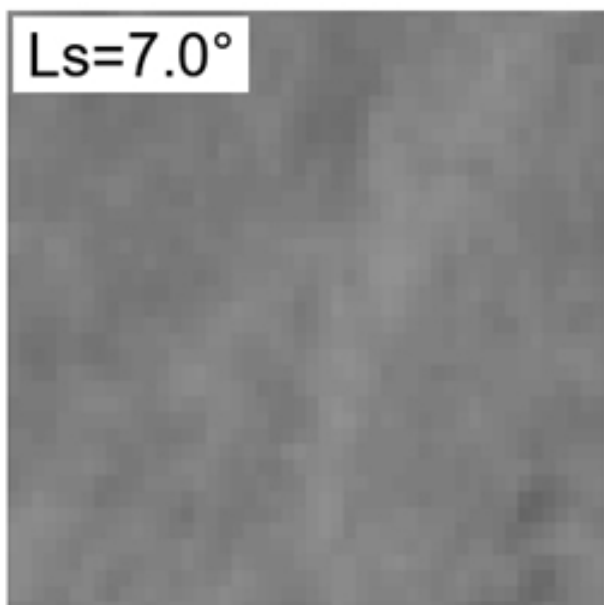
summer

Ice Block Ib1



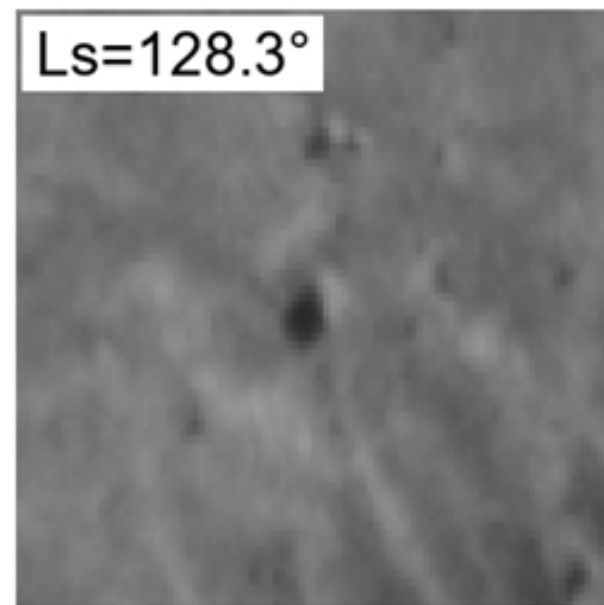
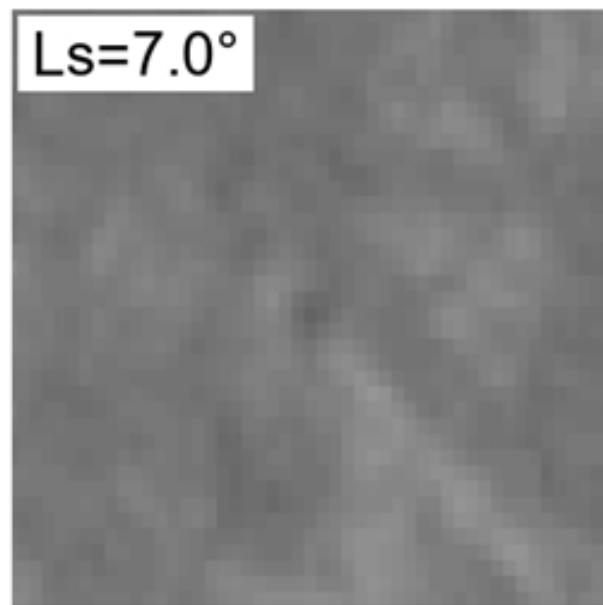
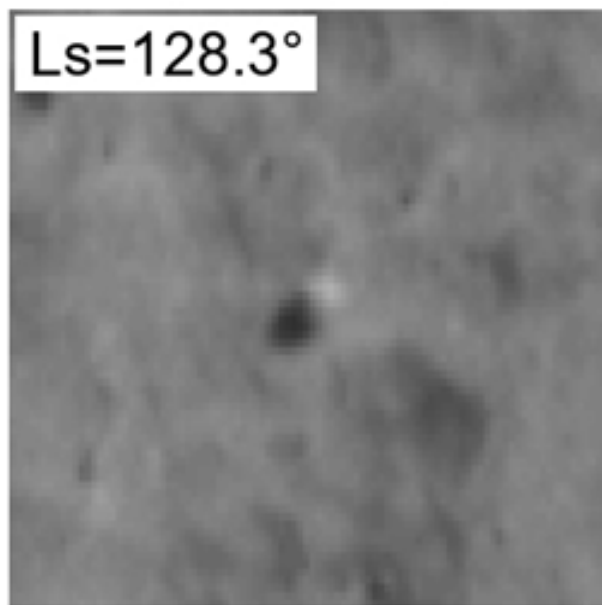
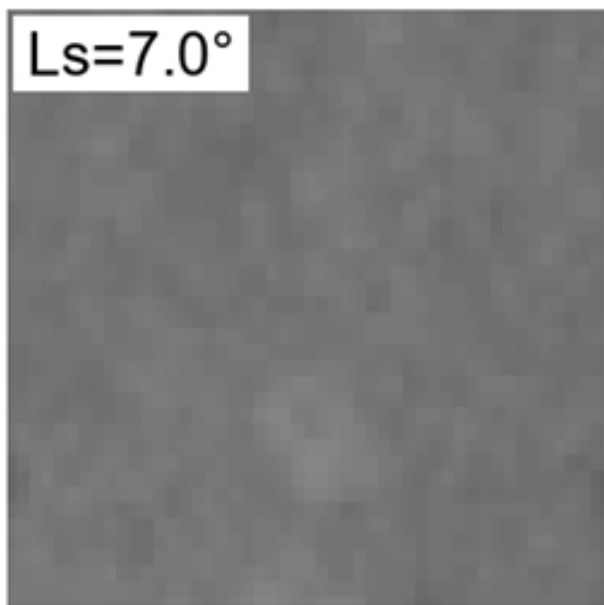
Ice Block ub1

Ice Block Ib2



Ice Block ub2

Ice Block Ib3



Ice Block ub3

Figure 9.

# Ice blocks fully covered

# Ice blocks NOT fully covered

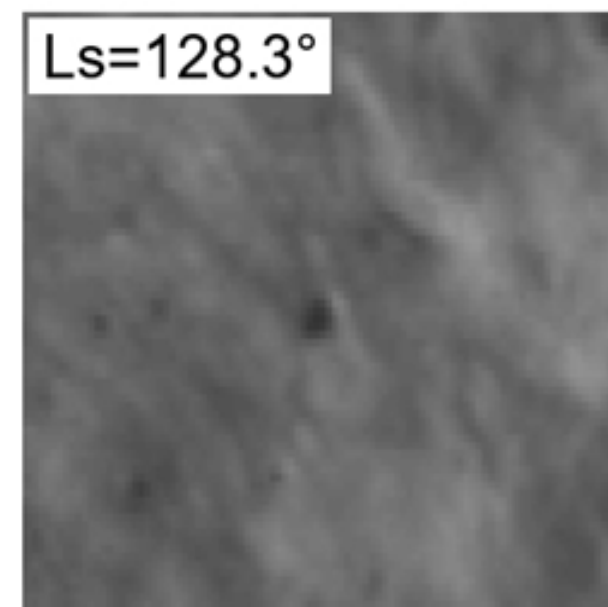
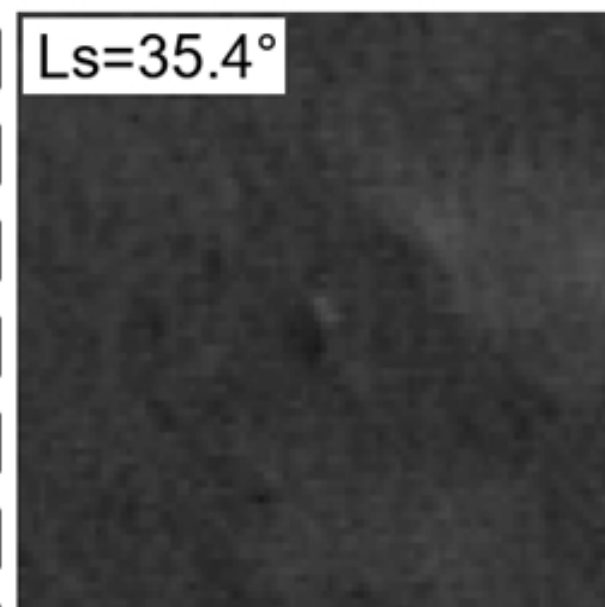
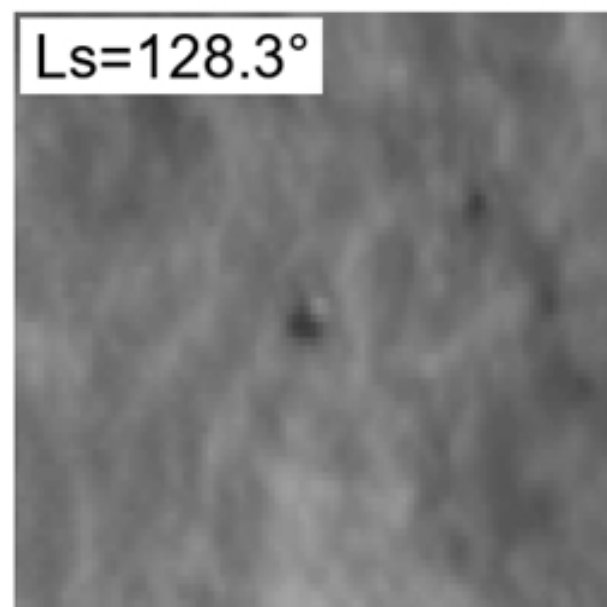
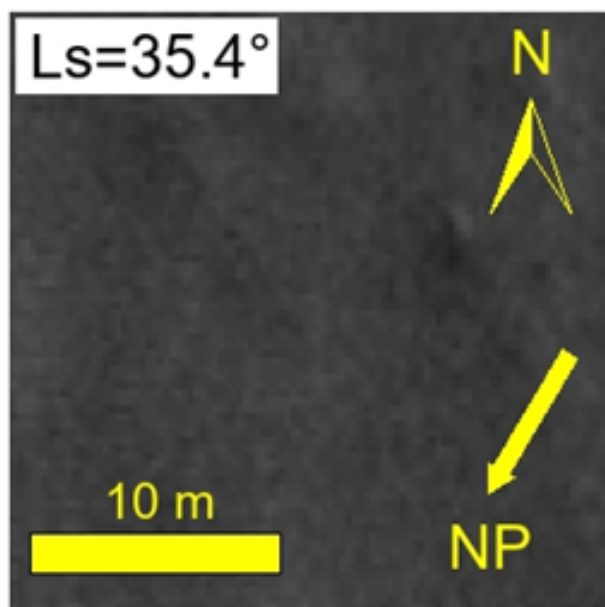
middle spring

summer

middle spring

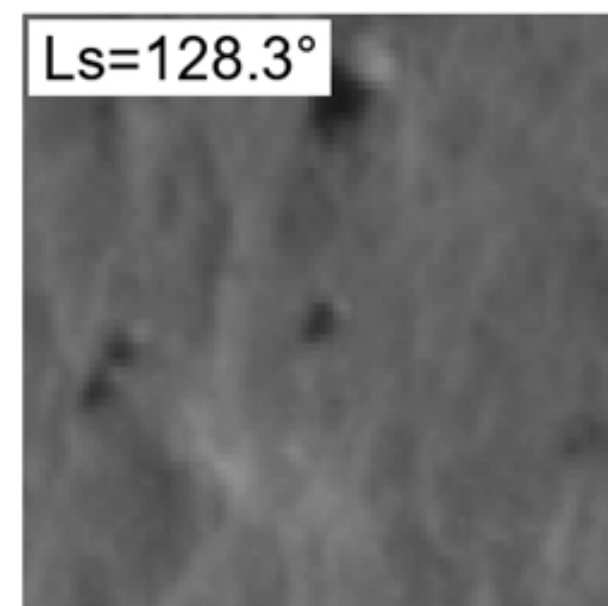
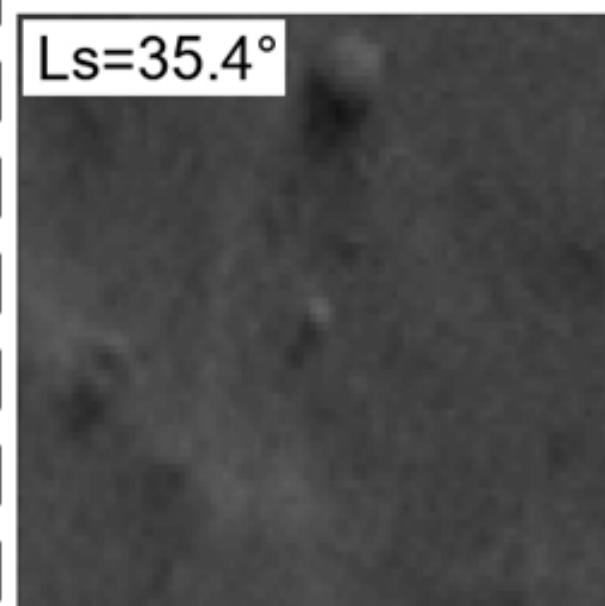
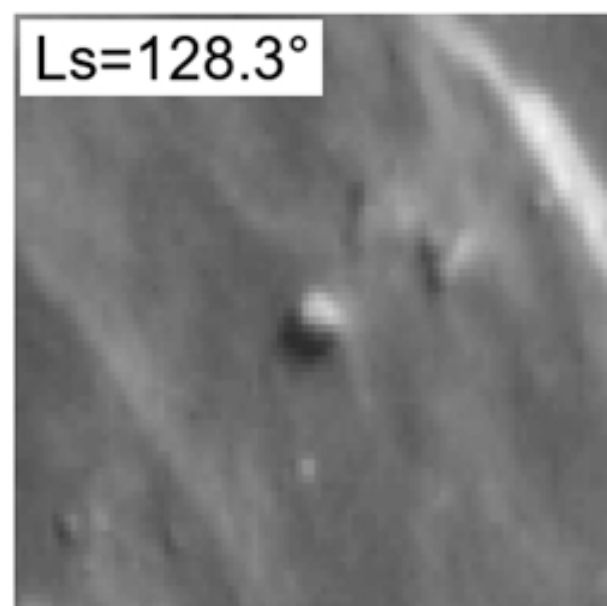
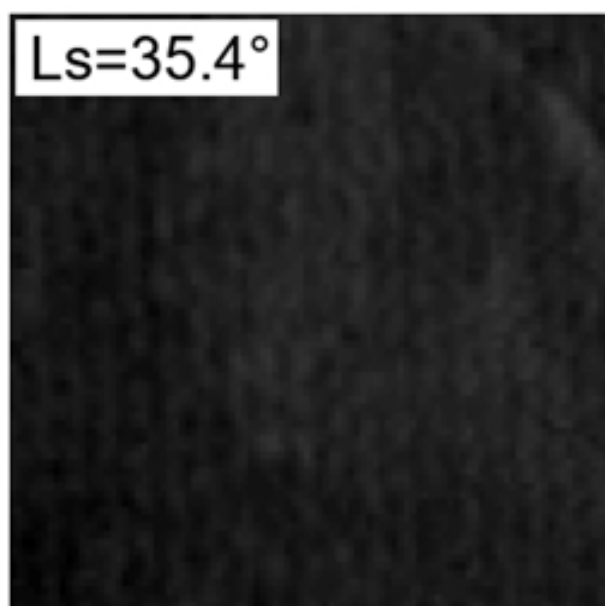
summer

Ice Block Ib4



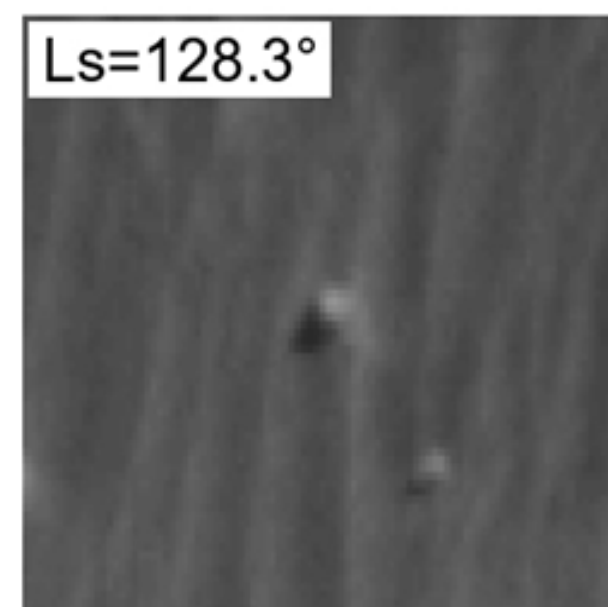
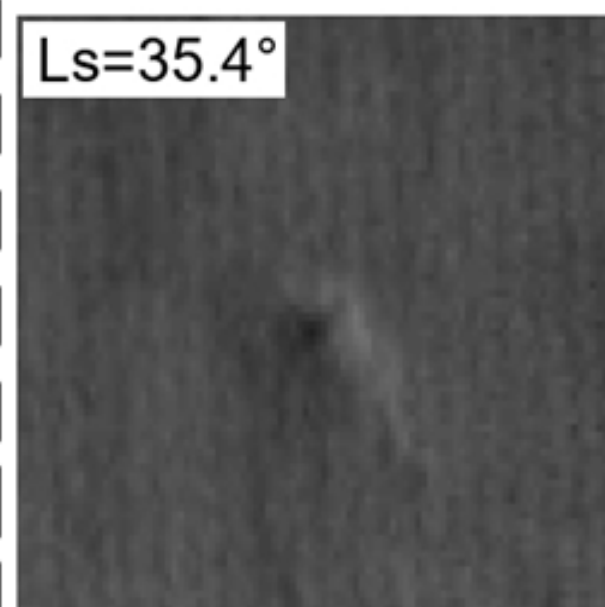
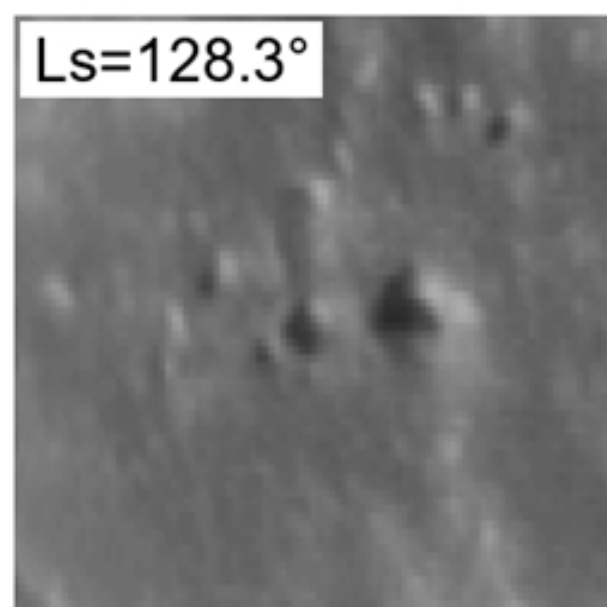
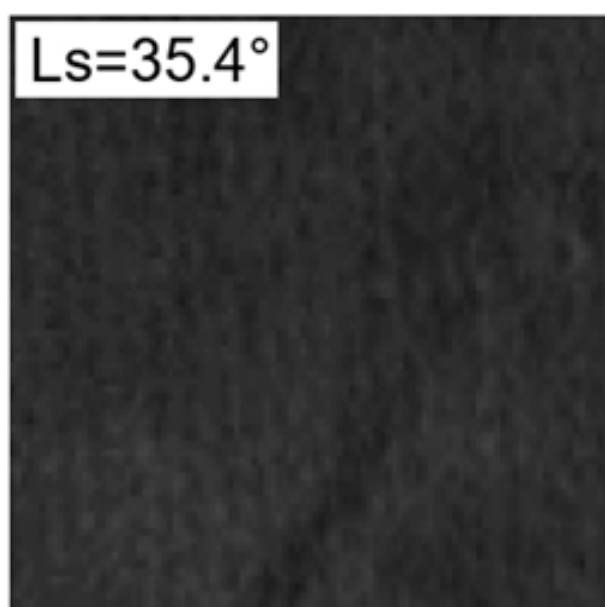
Ice Block ub4

Ice Block Ib5



Ice Block ub5

Ice Block Ib6



Ice Block ub6

Figure 10.

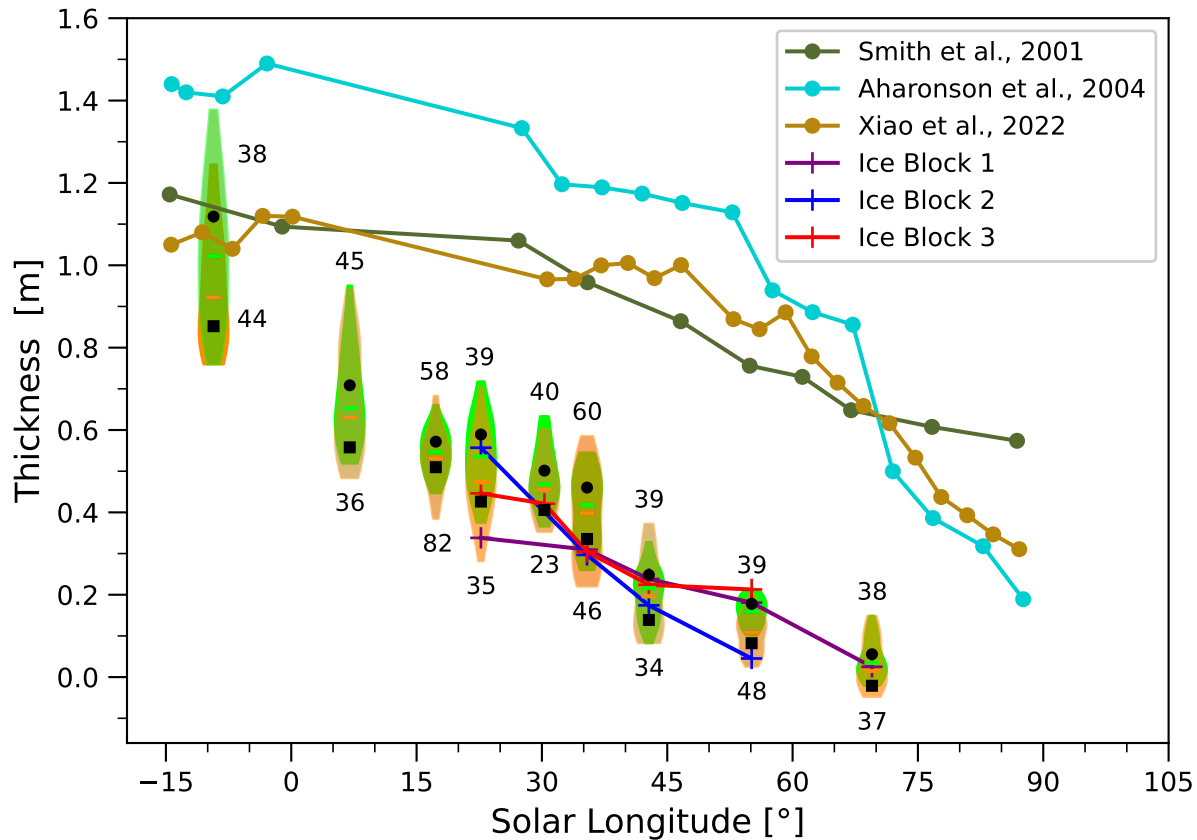


Figure 11.

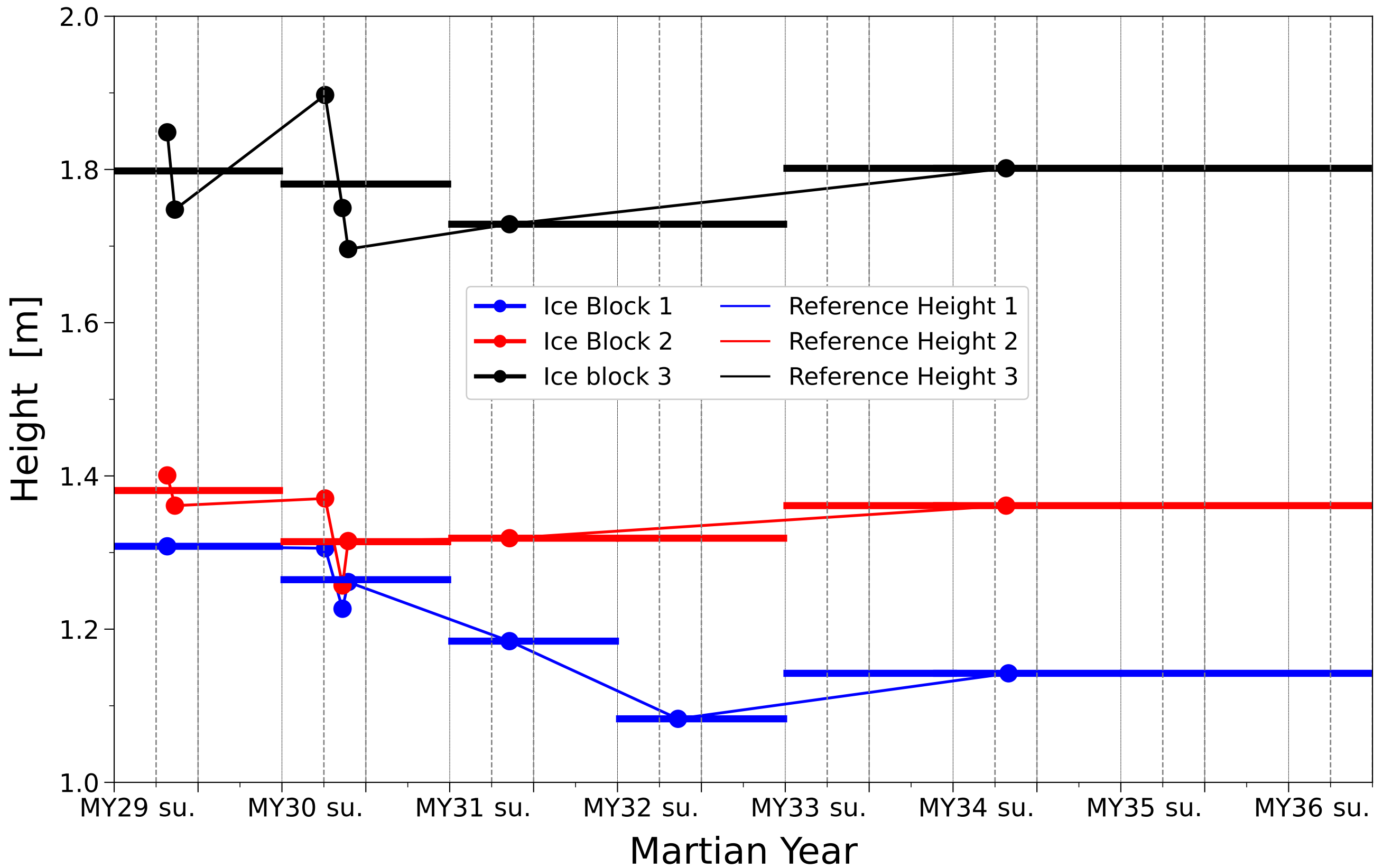


Figure 12.

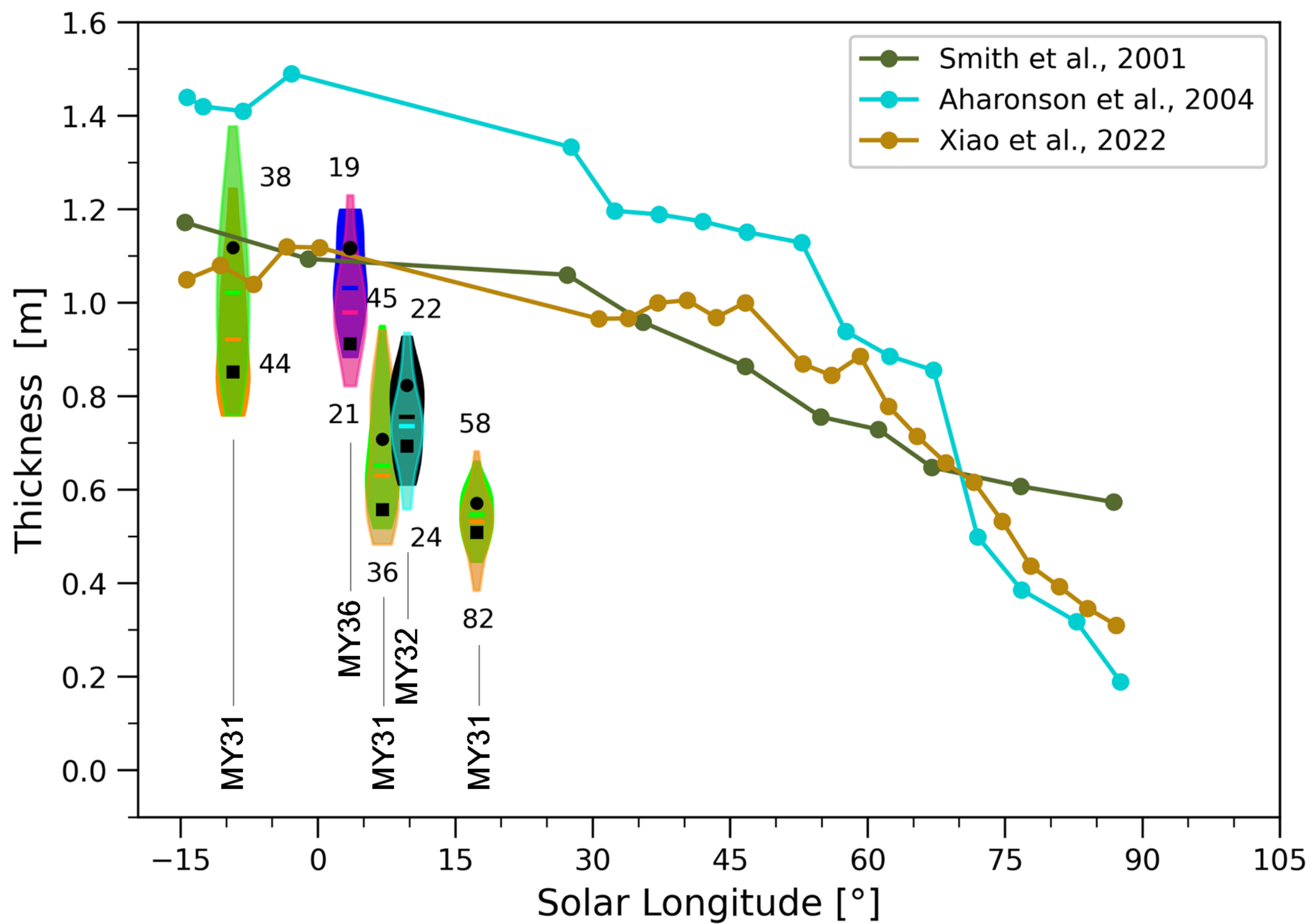


Figure 13.

# Ice block with parallel walls

middle spring

summer

# Ice block with nonparallel walls

middle spring

summer

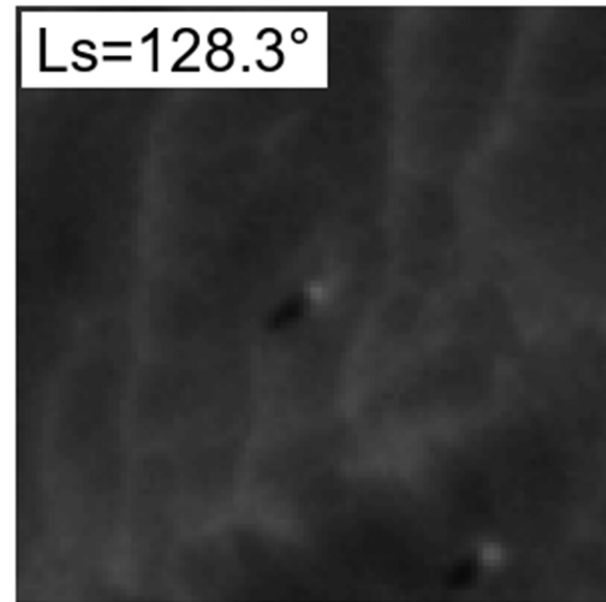
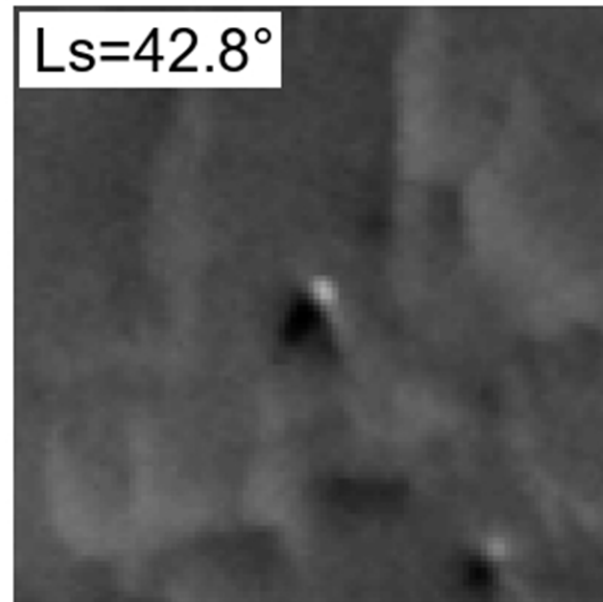
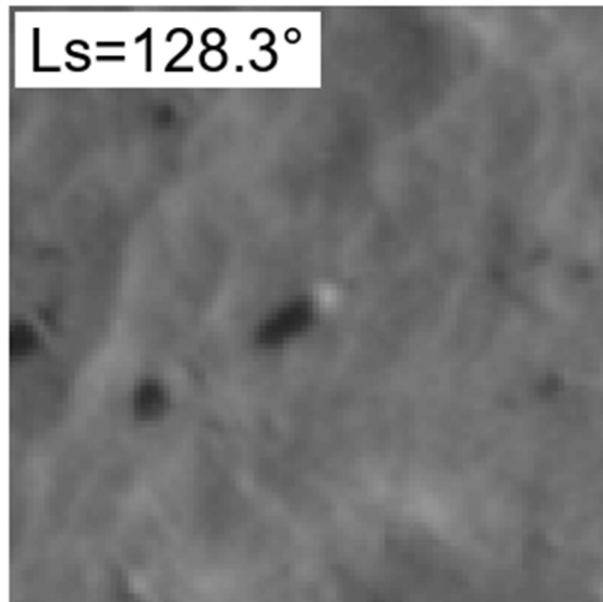
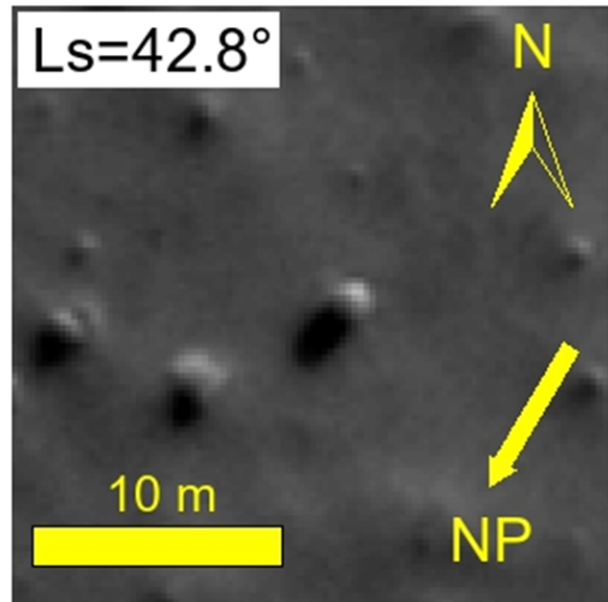


Figure 14.

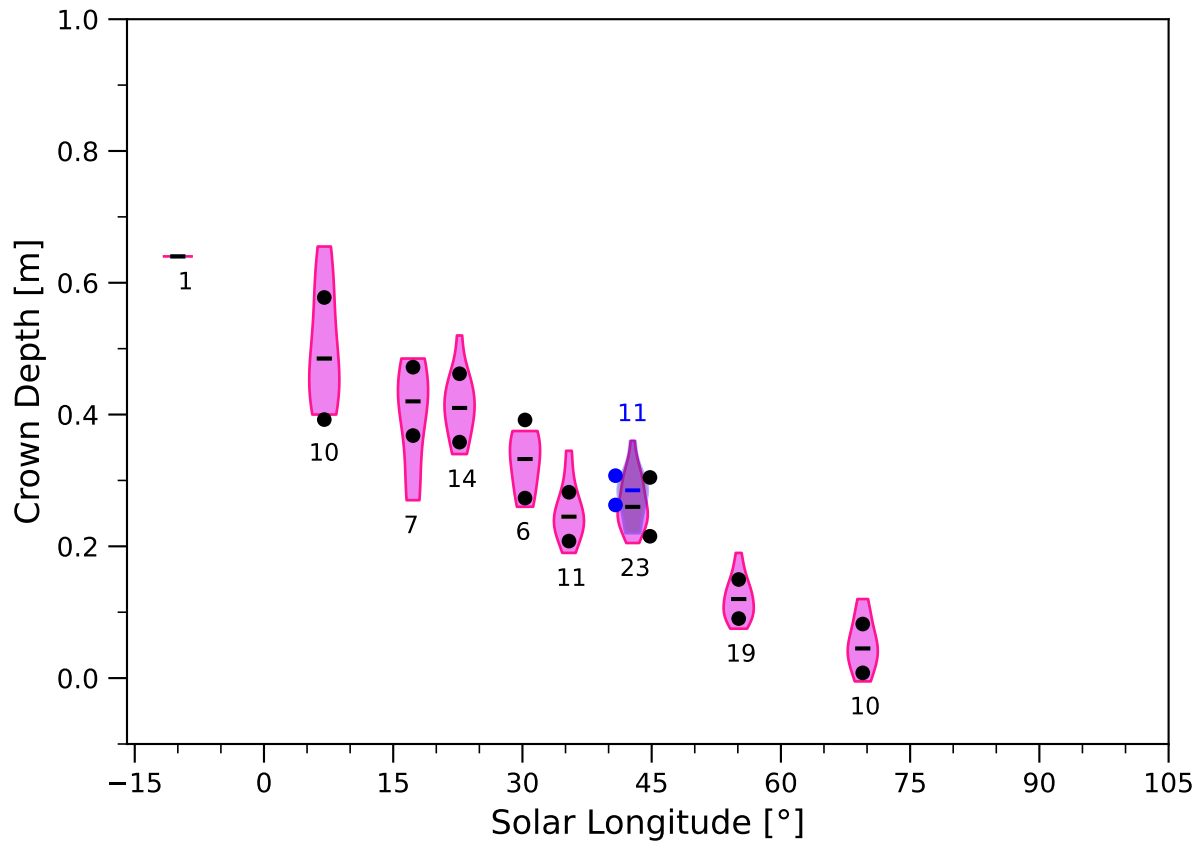
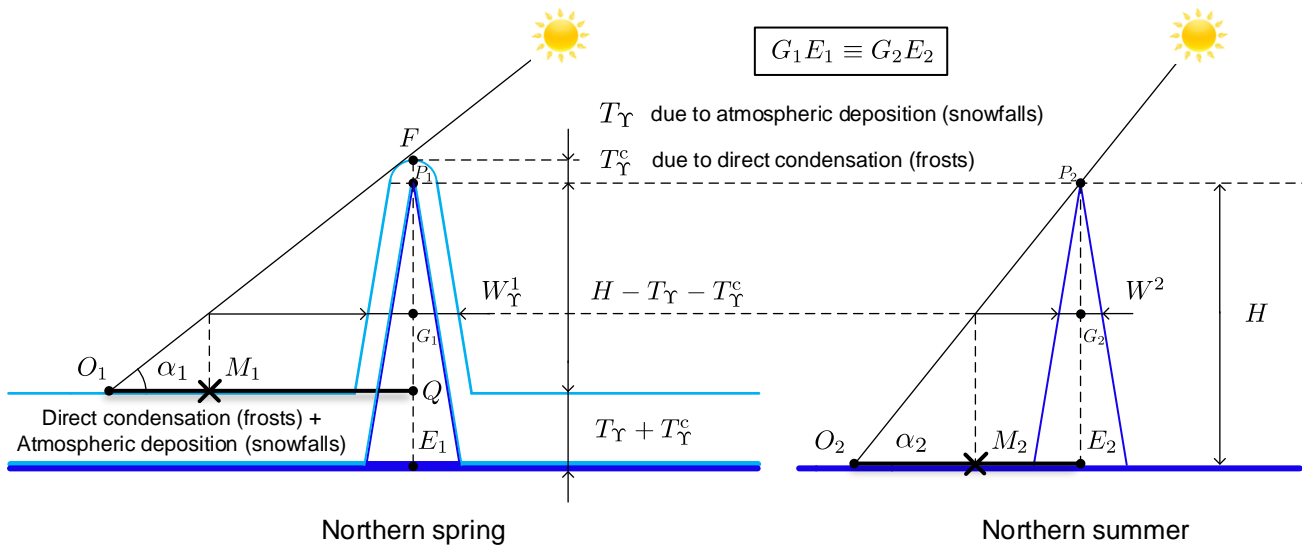


Figure 15.



▬▬ Boundary of CO<sub>2</sub> ice

▬▬ Boundary of H<sub>2</sub>O ice

✕ Shadow width measuring point

Figure 16.

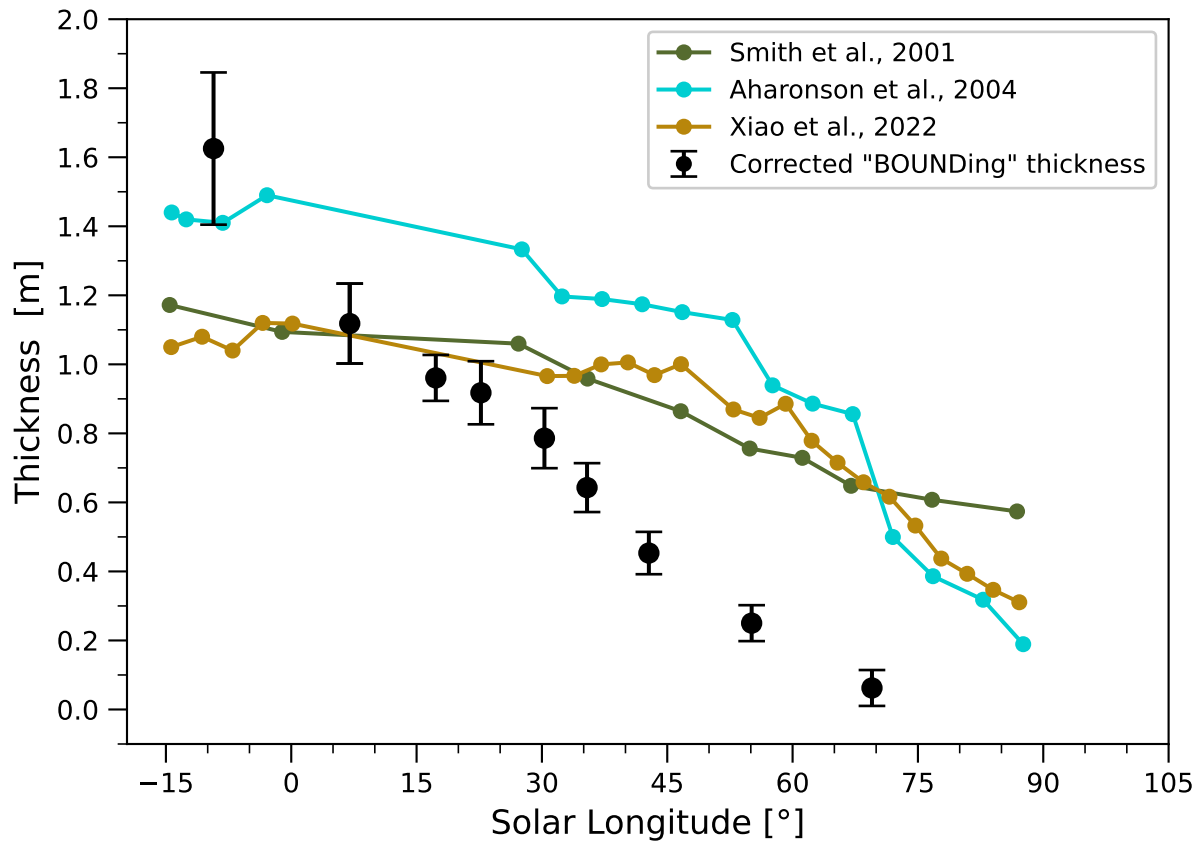
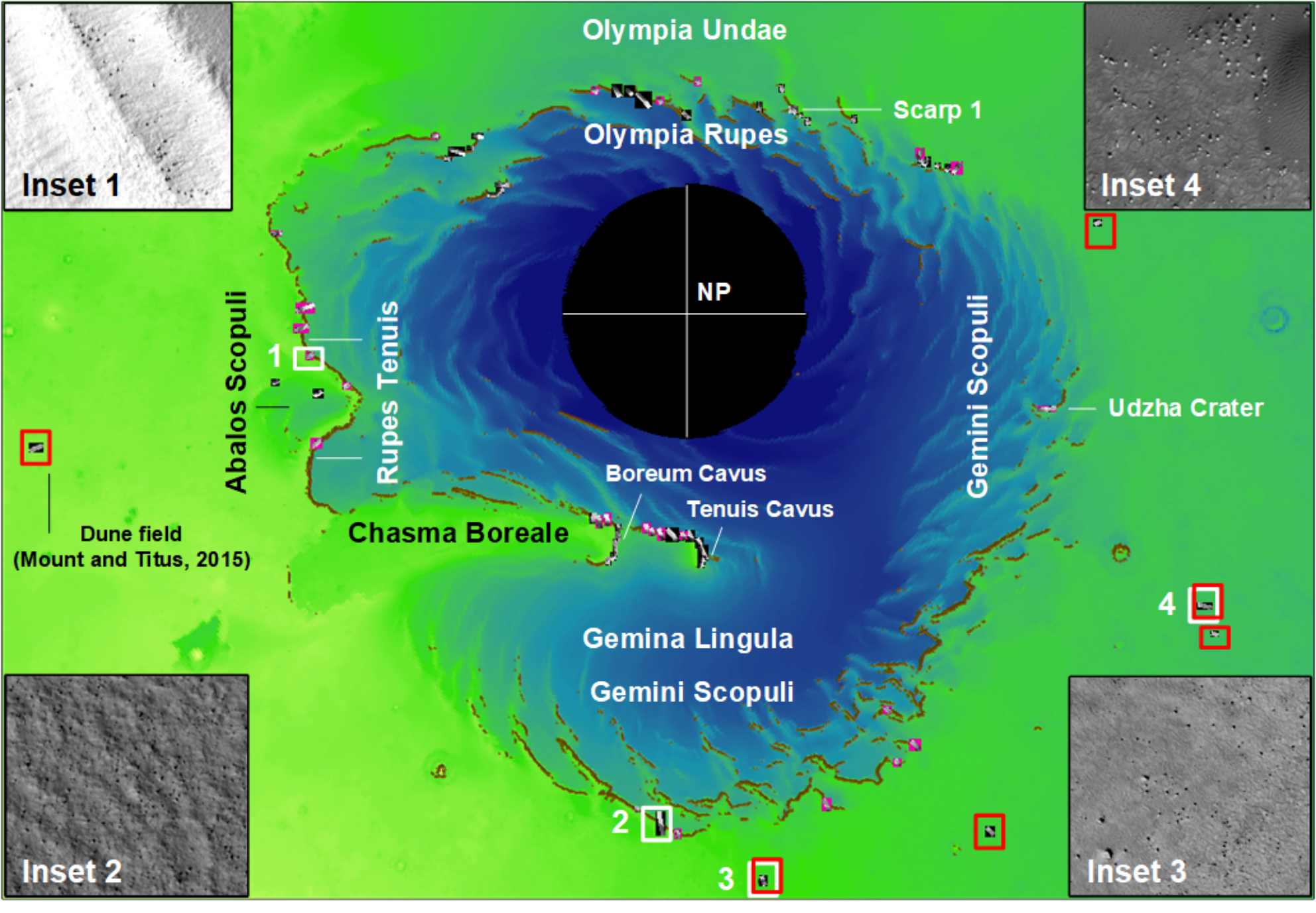


Figure 17.



**1 Supporting Information for “Are seasonal deposits in  
2 spring at the Martian North Pole much shallower than  
3 previously thought?”**

Haifeng Xiao<sup>1</sup>, Yuchi Xiao<sup>2</sup>, Shu Su<sup>1</sup>, Frédéric Schmidt<sup>3,4</sup>, Luisa M. Lara<sup>5</sup>,

Pedro J. Gutierrez<sup>5</sup>

**4** <sup>1</sup>Institute of Geodesy and Geoinformation Science, Technische Universität Berlin, Berlin, Germany

**5** <sup>2</sup>School of Mechanical Engineering and Electronic Information, China University of Geosciences, Wuhan, China

**6** <sup>3</sup>Université Paris-Saclay, CNRS, GEOPS, Orsay, France

**7** <sup>4</sup>Institut Universitaire de France (IUF), Paris, France

**8** <sup>5</sup>Instituto de Astrofísica de Andalucía (IAA-CSIC), Granada, Spain

**9 Contents of this file**

**10** 1. Tables S1, S2, S3, and S4

**11** 2. Text S1

**12** 3. Figures S1, S2, and S3

**13**

**14**

**15**

**16**

**17**

Table S1: HiRISE Images Adopted, Solar and Slope Properties, and Depth Results for Ice Block 1

18

Image ID*	Date	Solar	Mars Year	Solar Condition		Slope Condition		Ice Block	Snow
		Longitude	Season	elevation	azimuth	magnitude	aspect		
								Height [m]	Depth [m]
PSP_007710	19 Mar 2008	47.0°	MY29 sp.	23°	192.7°	4.7°	64.8°	1.19	0.12
<b>PSP_009648</b>	17 Aug 2008	113.9°	<b>MY30 su.</b>	28°	200.6°	13.0°	115.8°	1.31	NA
ESP_016228	12 Jan 2010	36.6°	MY30 sp.	20°	189.2°	10.0°	110.0°	0.92	0.34
ESP_016426	27 Jan 2010	43.6°	MY30 sp.	22°	196.2°	10.0°	110.0°	1.06	0.20
ESP_016439	28 Jan 2010	44.0°	MY30 sp.	22°	191.1°	13.0°	115.8°	1.08	0.18
ESP_016505	02 Feb 2010	46.3°	MY30 sp.	23°	193.4°	9.6°	94.1°	1.04	0.22
ESP_016650	13 Feb 2010	51.3°	MY30 sp.	24°	192.8°	10.0°	110.0°	1.16	0.10
ESP_016716	19 Feb 2010	53.6°	MY30 sp.	25°	195.0°	10.0°	110.0°	1.19	0.07
<b>ESP_017863</b>	19 May 2010	92.7°	<b>MY30 su.</b>	30°	194.8°	12.8°	103.7°	1.31	NA
<b>ESP_018905</b>	08 Aug 2010	130.0°	<b>MY30 su.</b>	23°	205.7°	6.8°	95.3°	1.23	NA
<b>ESP_019222</b>	02 Sep 2010	142.1°	<b>MY30 su.</b>	19°	221.4°	6.8°	95.3°	1.26	NA
ESP_024654 †	30 Oct 2011	22.7°	MY31 sp.	14°	186.2°	12.3°	94.9°	0.85	0.34
<b>ESP_025010</b>	27 Nov 2011	35.4°	MY31 sp.	19°	188.4°	12.3°	94.9°	0.87	0.31
ESP_025221	13 Dec 2011	42.8°	MY31 sp.	22°	190.4°	12.8°	103.7°	0.95	0.24
ESP_025577	10 Jan 2012	55.1°	MY31 sp.	25°	191.4°	13.7	108.7	1.00	0.18
<b>ESP_027674</b>	21 Jun 2012	128.3°	<b>MY31 su.</b>	24°	206.4°	10.0°	110.0°	1.18	NA
ESP_033713 †	05 Oct 2013	31.4°	MY32 sp.	18°	189.3°	13.4°	97.8°	0.95	0.14
ESP_033766	09 Oct 2013	33.3°	MY32 sp.	18°	196.8°	9.3°	77.5°	0.88	0.20
ESP_034043	31 Oct 2013	43.0°	MY32 sp.	22°	201.1°	13.4°	97.8°	0.85	0.24
ESP_034254	16 Nov 2013	50.3°	MY32 sp.	24°	202.8°	12.8°	103.7°	0.99	0.09
ESP_034399	27 Nov 2013	55.3°	MY32 sp.	25°	202.6°	11.3°	85.8°	1.07	0.01
<b>ESP_036535</b>	13 May 2014	129.9°	<b>MY32 su.</b>	24°	205.2°	11.3°	85.8°	1.08	NA
ESP_052306	23 Sep 2017	64.7°	MY34 sp.	27°	193.2°	11.3°	85.8°	1.12	0.02
<b>ESP_053875</b>	23 Jan 2018	119.1°	<b>MY34 su.</b>	27°	196.4°	12.3°	94.9°	1.14	NA
ESP_060126	25 May 2019	30.1°	MY35 sp.	17°	187.7°	12.2°	93.1°	0.68	0.46
ESP_069095	23 Apr 2021	35.5°	MY36 sp.	19°	198.0°	11.3°	85.8°	0.84	0.30
ESP_069834	19 Jun 2021	61.0°	MY36 sp.	26°	213.8°	11.3°	85.8°	1.04	0.10
ESP_069992	02 Jul 2021	66.4°	MY36 sp.	27°	208.1°	11.3°	85.8°	1.04	0.10

20

\* Image ID should be suffixed with “\_2650”. † marks the images with a grid size of 0.50 m, while the rest of them feature a better resolution of 0.25 m. Note that the solar azimuth is with respect to the North Pole while the slope aspect is defined as the angle with respect to the map north. sp. is the abbreviation for spring and su. for summer. Summer images used to derive the reference heights are marked in bold.

Table S2: HiRISE Images Adopted, Solar and Slope Properties, and Depth Results for Ice Block 2

Image ID*	Date	Solar Longitude	Mars Year Season	Solar Condition		Slope Condition		Ice Block Height [m]	Snow Depth [m]
				elevation	azimuth	magnitude	aspect		
PSP_007710	19 Mar 2008	47.0°	MY29 sp.	23°	192.7°	1.0°	295.9°	1.16	0.23
PSP_007763	23 Mar 2008	48.9.0°	MY29 sp.	23°	192.7°	2.1°	330.4°	1.26	0.12
<b>PSP_009648</b>	17 Aug 2008	113.9°	<b>MY29 su.</b>	28°	200.6°	3.0°	346.9°	1.40	NA
<b>PSP_010097</b>	21 Sep 2008	130.3°	<b>MY29 su.</b>	23°	218.6°	2.9°	324.7°	1.36	NA
ESP_016228	12 Jan 2010	36.6°	MY30 sp.	20°	189.2°	2.1°	330.4°	1.04	0.28
ESP_016426	27 Jan 2010	43.6°	MY30 sp.	22°	196.2°	3.0°	346.9°	1.09	0.23
ESP_016439	28 Jan 2010	44.0°	MY30 sp.	22°	191.1°	1.0°	295.9°	1.12	0.19
ESP_016505	02 Feb 2010	46.3°	MY30 sp.	23°	193.4°	3.0°	346.9°	1.14	0.17
ESP_016650	13 Feb 2010	51.3°	MY30 sp.	24°	192.8°	3.0°	346.9°	1.19	0.12
ESP_016716	19 Feb 2010	53.6°	MY30 sp.	25°	195.0°	3.0°	346.9°	1.17	0.14
ESP_017217	30 Mar 2010	70.7°	MY30 sp.	28°	195.0°	3.0°	346.9°	1.19	0.12
<b>ESP_017863</b>	19 May 2010	92.7°	<b>MY30 su.</b>	30°	194.8°	2.6°	296.3°	1.37	NA
<b>ESP_018905</b>	08 Aug 2010	130.0°	<b>MY30 su.</b>	23°	205.7°	3.4°	347.6°	1.26	NA
<b>ESP_019222</b>	02 Sep 2010	142.1°	<b>MY30 su.</b>	19°	221.4°	3.4°	347.6°	1.32	NA
ESP_024654 †	30 Oct 2011	22.7°	MY31 sp.	14°	186.2°	2.1°	330.4°	0.76	0.56
ESP_025010	27 Nov 2011	35.4°	MY31 sp.	19°	188.4°	3.0°	346.9°	1.02	0.30
ESP_025221	13 Dec 2011	42.8°	MY31 sp.	22°	190.4°	2.1°	330.4°	1.15	0.17
ESP_025577	10 Jan 2012	55.1°	MY31 sp.	25°	191.4°	2.9°	324.7°	1.27	0.05
<b>ESP_027674</b>	21 Jun 2012	128.3°	<b>MY31 su.</b>	24°	206.4°	3.0°	346.9°	1.32	NA
ESP_033476 †	17 Sep 2013	22.9°	MY32 sp.	14°	197.3°	3.0°	346.9°	0.91	0.41
ESP_033713 †	05 Oct 2013	31.4°	MY32 sp.	18°	189.3°	3.0°	346.9°	1.02	0.30
ESP_033766	09 Oct 2013	33.3°	MY32 sp.	18°	196.8°	2.1°	330.4°	1.03	0.29
ESP_034043	31 Oct 2013	43.0°	MY32 sp.	22°	201.1°	2.1°	330.4°	1.01	0.31

Image ID*	Date	Solar	Mars Year	Solar Condition		Slope Condition		Ice Block	Snow
		Longitude	Season	elevation	azimuth	magnitude	aspect	Height [m]	Depth [m]
<b>27</b> ESP_034610	14 Dec 2013	62.5°	MY32 sp.	27°	205.0°	2.6°	296.3°	1.13	0.19
<b>ESP_053730</b>	12 Jan 2018	113.9°	<b>MY34 su.</b>	28°	197.4°	2.1°	330.4°	1.36	NA
ESP_069095	23 Apr 2021	35.5°	MY34 sp.	19°	198.0°	3.0°	346.9°	0.89	0.47
<b>28</b> ESP_069649	5 Jun 2021	54.7°	MY34 sp.	25°	202.0°	2.1°	330.4°	1.19	0.17

\* Image ID should be suffixed with “\_2650”. † marks the images with a grid size of 0.50 m, while the rest of them feature a better resolution of 0.25 m. Note that the solar azimuth is with respect to the North Pole while the slope aspect is defined as the angle with respect to the map north. sp. is the abbreviation for spring and su. for summer. Summer images used to derive the reference heights are marked in bold.

31

32

Table S3: HiRISE Images Adopted, Solar and Slope Properties, and Depth Results for Ice Block 3

Image ID*	Date	Solar	Mars Year	Solar Condition		Slope Condition		Ice Block	Snow
		Longitude	Season	elevation	azimuth	magnitude	aspect	Height [m]	Depth [m]
PSP_007710	19 Mar 2008	47.0°	MY29 sp.	23°	192.7°	4.7°	55.2°	1.58	0.22
PSP_007763	23 Mar 2008	48.9.0°	MY29 sp.	23°	192.7°	4.7°	55.2°	1.59	0.20
<b>PSP_009648</b>	17 Aug 2008	113.9°	<b>MY29 su.</b>	28°	200.6°	5.9°	52.9°	1.85	NA
<b>PSP_010097</b>	21 Sep 2008	130.3°	<b>MY29 su.</b>	23°	218.6°	4.7°	55.2°	1.75	NA
ESP_016228	12 Jan 2010	36.6°	MY30 sp.	20°	189.2°	5.9°	52.9°	1.44	0.34
ESP_016426	27 Jan 2010	43.6°	MY30 sp.	22°	196.2°	5.9°	52.9°	1.50	0.29
<b>33</b> ESP_016439	28 Jan 2010	44.0°	MY30 sp.	22°	191.1°	5.9°	52.9°	1.47	0.31
ESP_016505	02 Feb 2010	46.3°	MY30 sp.	23°	193.4°	5.9°	52.9°	1.53	0.25
ESP_016650	13 Feb 2010	51.3°	MY30 sp.	24°	192.8°	5.9°	52.9°	1.52	0.26
ESP_016716	19 Feb 2010	53.6°	MY30 sp.	25°	195.0°	5.9°	52.9°	1.55	0.23
ESP_017217	30 Mar 2010	70.7°	MY30 sp.	28°	195.0°	4.7°	55.2°	1.59	0.19
<b>ESP_017863</b>	19 May 2010	92.7°	<b>MY30 su.</b>	30°	194.8°	4.7°	55.2°	1.90	NA
<b>ESP_018905</b>	08 Aug 2010	130.0°	<b>MY30 su.</b>	23°	205.7°	5.9°	52.9°	1.75	NA
<b>ESP_019222</b>	02 Sep 2010	142.1°	<b>MY30 su.</b>	19°	221.4°	5.9°	52.9°	1.70	NA
ESP_024654 †	30 Oct 2011	22.7°	MY31 sp.	14°	186.2°	7.5°	53.0°	1.28	0.45
ESP_024865	16 Nov 2011	30.3°	MY31 sp.	17°	188.6°	5.9°	52.9°	1.31	0.42

Image ID*	Date	Solar	Mars Year	Solar Condition		Slope Condition		Ice Block	Snow
		Longitude	Season	elevation	azimuth	magnitude	aspect	Height [m]	Depth [m]
ESP_025010	27 Nov 2011	35.4°	MY31 sp.	19°	188.4°	5.9°	52.9°	1.42	0.30
ESP_025221	13 Dec 2011	42.8°	MY31 sp.	22°	190.4°	6.4°	45.0°	1.50	0.22
ESP_025577	10 Jan 2012	55.1°	MY31 sp.	25°	191.4°	5.9°	52.9°	1.57	0.21
<b>ESP_027674</b>	21 Jun 2012	128.3°	<b>MY31 su.</b>	24°	206.4°	5.6°	54.5°	1.73	NA
ESP_033713†	05 Oct 2013	31.4°	MY32 sp.	18°	189.3°	6.4°	45.0°	1.33	0.40
34 ESP_033766	09 Oct 2013	33.3°	MY32 sp.	18°	196.8°	7.0°	44.4°	1.31	0.12
ESP_034254	16 Nov 2013	50.3°	MY32 sp.	24°	202.8°	4.7°	55.2°	1.44	0.29
ESP_034399	27 Nov 2013	55.3°	MY32 sp.	25°	202.6°	4.7°	55.2°	1.55	0.18
ESP_034610	14 Dec 2013	62.5°	MY32 sp.	27°	205.0°	4.7°	55.2°	1.57	0.16
<b>ESP_053730</b>	12 Jan 2018	113.9°	<b>MY34 su.</b>	28°	197.4°	6.4°	45°	1.80	NA
ESP_069095	23 Apr 2021	35.5°	MY36 sp.	19°	198.0°	4.7°	55.2°	1.24	0.56
ESP_069649	5 Jun 2021	54.7°	MY36 sp.	25°	202.0°	4.7°	55.2°	1.49	0.31
ESP_069834	19 Jun 2021	61.0°	MY36 sp.	25°	202.0°	4.7°	55.2°	1.54	0.26
35 ESP_069992	2 Jul 2021	66.4°	MY36 sp.	31°	202.0°	4.7°	55.2°	1.61	0.19

\* Image ID should be suffixed with “\_2650”. † marks the images with a grid size of 0.50 m, while the rest of them feature a better resolution of 0.25 m. Note that the solar azimuth is with respect to the North Pole while the slope aspect is defined as the angle with respect to the map north. sp. is the abbreviation for spring and su. for summer. Summer images used to derive the reference heights are marked in bold.

Table S4: Statistical Summary of the Thickness of the Seasonal Deposits in Late Winter and Spring of MY31

Thickness [m]	Solar Longitude								
	350.7°	7.0°	17.3°	22.7°	30.3°	35.4°	42.8°	55.1°	69.5°
40 Snowfall	0.97±0.13	0.64±0.08	0.54±0.03	0.50±0.08	0.46±0.05	0.41±0.06	0.21±0.05	0.13±0.05	0.02±0.02
Frost	0.64±0.18	0.49±0.09	0.42±0.06	0.41±0.04	0.33±0.07	0.25±0.03	0.26±0.03	0.12±0.02	0.05±0.04
41 Sum	1.63±0.22	1.12±0.12	0.96±0.07	0.92±0.09	0.79±0.09	0.64±0.07	0.45±0.06	0.25±0.05	0.06±0.05

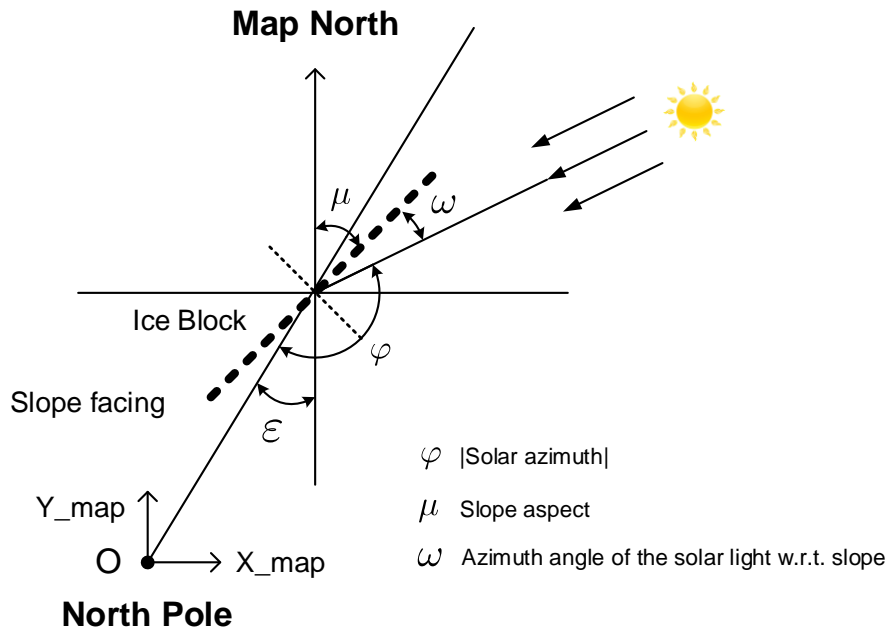


Figure S1: Schematic that illustrates the measured slope aspect and solar azimuth, and their relation to  $\omega$ , which represents the angular separation between the solar rays and the bearing of the slope. Origin of the map coordinate system, associated with a polar stereographic projection, centers at the North Pole.

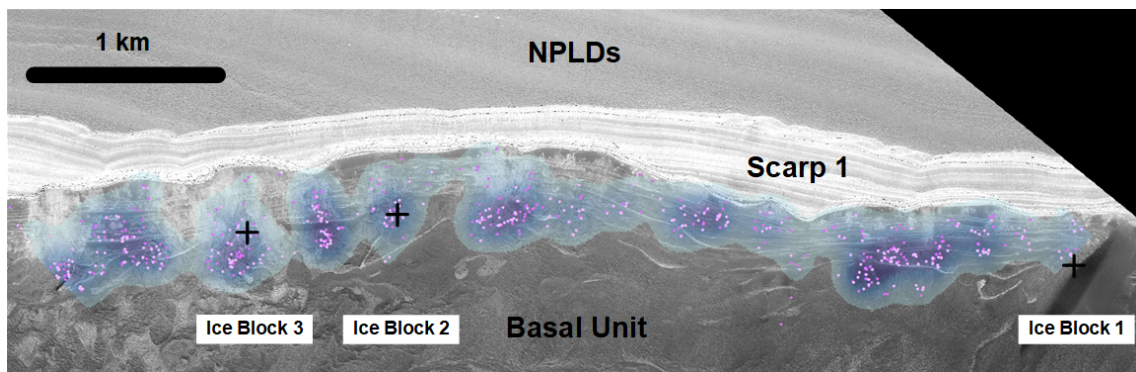


Figure S2: Distribution of the selected bounding ice blocks used to constrain the depth evolution of the seasonal deposits in MY31. Location is at Scarp 1, which is centered at (85.0°N, 151.5°E). Background image is a summer image acquired in MY29 (PSP\_009648\_2650\_RED; same as that used in Figure 3). Ice blocks that have been completely covered are marked by points in dark purple, while ice blocks that have not been submerged are marked by points in light purple. These points are draped over the density map with darker tone represents higher degree of clustering of the points. We mark the locations of Ice Blocks 1, 2, and 3 for reference.

44 **Text S1. Probabilistic analysis on the number of iterations needed in the**  
 45 **self-registration of the MOLA profiles**

46

47 Here, we discuss how many iterations are needed in the self-registration of the  
 48 MOLA profiles with the aim to generate a reference topographic model of the Mar-  
 49 tian North Pole. The probability that a specific profile, out of a full set of  $N$  profiles,  
 50 has not ever been selected and co-registered throughout all  $n$  iterations performed  
 51 is

$$52 \quad p = (1 - p_s)^n, \quad (1)$$

53 where  $p_s = 0.25$  is the fraction of the profiles randomly chosen at each iteration to  
 54 be co-registered to the rest of the profiles. The probability that a specific profile  
 55 has been selected for co-registration for at least once then stands at  $q = 1 - p$ . We  
 56 now define a discrete random variable  $X$  that describes the number of profiles that  
 57 have not ever been co-registered in the random selection process. Then,  $X$  follows  
 58 the binomial distribution,  $X \sim B(N, p)$ , which represents the number of successes  
 59 in a sequence of  $N$  independent Bernoulli trials, each with a success rate of  $p$ . The  
 60 probability mass function is as follows:

$$61 \quad \mathbb{P}(X = k) = \frac{N!}{k!(N - k)!} p^k q^{N-k} \quad (k = 0, 1, 2, \dots, N), \quad (2)$$

62 where  $!$  is the factorial function and  $k$  denotes the number of profiles that have  
 63 not been co-registered after  $n$  iterations. Given that  $N$  is sufficiently large ( $\gg 20$ )  
 64 and that  $p$  is small ( $\ll 0.05$ ),  $X$  can be approximated by a Poisson distribution  
 65  $X \sim \text{Pois}(\lambda)$ , which has a probability mass function given by

$$66 \quad \mathbb{P}(X = k) = \frac{\lambda^k e^{-\lambda}}{k!} \quad (k = 0, 1, 2, \dots, N), \quad (3)$$

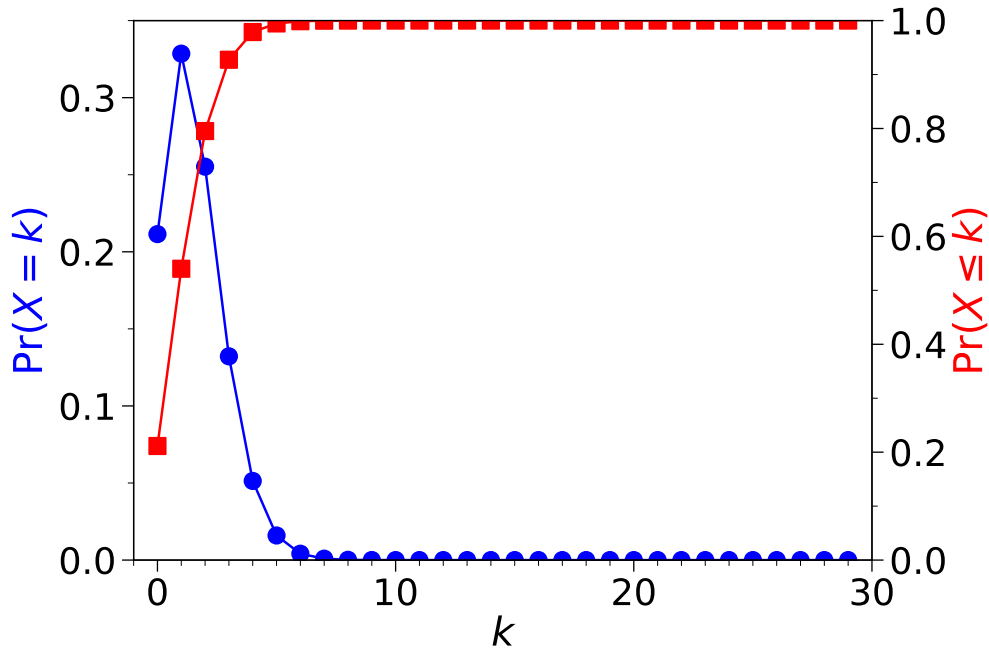


Figure S3: The probability mass function (blue dots) and cumulative distribution function (red squares) of the random variable  $X$  using  $N = 8,700$  and  $n = 30$ .

67 where  $e$  is Euler's number and the positive number  $\lambda$  equals the expected value of  $X$ ,  
 68 that is,  $\lambda = Np$ . The cumulative distribution function of the integer-valued random  
 69 variable  $X$  is

$$70 \quad \mathbb{P}(X \leq k) = e^{-\lambda} \sum_{m=0}^k \frac{\lambda^m}{m!} = \frac{\Gamma(k+1, \lambda)}{k!}, \quad (4)$$

71 where  $\Gamma(k+1, \lambda)$  is the upper incomplete gamma function. In the MOLA case  
 72 of a total number of 8,700 profiles, that is  $N = 8,700$ , and 30 iterations, that is  
 73  $n = 30$ , the most probable number of profiles that have not been co-registered even  
 74 once stand at just one, with a probability of 0.33 (Figure S3). Meanwhile, the  
 75 cumulative probability that less than 6 profiles have not been co-registered in the  
 76 self-registration iterations reaches 99.88%. These statistics justify the repeating of  
 77 the self-registration process for up to 30 times.